Effects of Gd on Microstructure and Deformation Mechanisms of Hot-Rolled Mg-Zn-Y Alloy

by

Bijoy Mallick

Student ID: 0421112016

MASTER OF SCIENCE IN MATERIALS AND METALLURGICAL ENGINEERING

Department of Materials and Metallurgical Engineering

BANGLADESH UNIVERSITY OF ENGINEERING AND TECHNOLOGY (BUET)

September 2023

The thesis titled **"Effects of Gd on Microstructure and Deformation Mechanisms of Hot-Rolled Mg-Zn-Y Alloy"** Submitted by Bijoy Mallick, Roll No. 0421112016 and Session: October 2021 has been accepted as satisfactory as a partial fulfilment of the requirement for the degree of M.Sc. Engg. in Materials and Metallurgical Engineering on 24th September, 2023.

BOARD OF EXAMINERS

1. _____ **Chairman**
Dr. Hossain Mohammad Mamun Al Rashed (Supervisor)
Associate Professor
Department of Materials and Metallurgical Engineering, BUET, Dhaka

2. _____ **Member**
Dr. A. K. M. Bazlur Rashid (Ex-officio)
Professor and Head
Department of Materials and Metallurgical Engineering, BUET, Dhaka

3. _____ **Member**
Dr. Md. Aminul Islam
Professor
Department of Materials and Metallurgical Engineering, BUET, Dhaka

4. _____ **Member**
Dr. Kazi Mohammad Shorowordi
Professor
Department of Materials and Metallurgical Engineering, BUET, Dhaka

5. _____ **Member**
Dr. Qumrul Ahsan (External)
Vice Chancellor
University of Asia Pacific, Dhaka

CANDIDATE'S DECLEARATION

It is hereby declared that no part of the work mentioned in the thesis has ever been used to support an application for a different degree or certification from this university or any other university or other learning institution.

Bijoy Mallick

ABSTRACT

The microstructural evolution under various conditions (as-cast, homogenized, and hot rolled) and the deformation mechanisms at four distinct temperatures (250°C, 300°C, 350°C, and 400°C) and two strain rates ($1x10^{-4}$ and $5x10^{-4}$ s^{-1}) of the Mg-1Zn-1.5Y alloy were investigated with the addition of Gd (1%, 2%, and 6 wt%) to the alloy system. The chemical composition was analyzed using XRF, confirming the desired alloy composition with negligible deviation. Optical microscopy was employed to observe dendritic arm presence, measure grain size, assess precipitation conditions, and identify secondary phases within the matrix. Dendritic arms were evident in the as-cast condition, with density increasing due to Gd addition. Additionally, a trend of grain size reduction was observed with Gd inclusion in all conditions. Notably, hot rolling significantly reduced grain size through dynamic recrystallization (DRX). XRD, SEM, EDS, DSC, and CALPHAD analysis were utilized to determine different phases present in the alloy matrix, phase morphology, chemical composition, phase formation temperature, and phase evolution and volume fraction with temperature for the three alloys. The 14H-LPSO phase was consistently found within the α-Mg matrix of all compositions, with volume fraction increasing as Gd content rises. However, morphological variations were identified due to compositional changes, with lamellar and blocky LPSO phases forming in alloy A (1% Gd) and B (2% Gd), and blocky LPSO in alloy-C (6% Gd). Furthermore, in CALPHAD analysis $Mg_5(Gd,Y)$ was observed in alloy-A and C, while alloy-B contained the W-phase ($Mg_3Zn_3(Y,Gd)_2$), which remained stable till the elevated temperatures around 600°C. However, above 450°C, the 14H-LPSO phase was found to start dissolving within the α-Mg matrix. Tensile testing at four different temperatures and two strain rates was conducted to assess changes in strength, ductility, and deformation mechanisms due to Gd addition. An optimal combination of strength and ductility was observed in alloy-B (2% Gd) at high temperature (400°C) and both strain rates, attributed to the presence of a bimodal 14H-LPSO phase (mix of lamellar and blocky LPSO) and the W-phase at elevated temperatures. Conversely, alloy-C demonstrated promising performance below 350°C, possibly due to the maximum volume fraction of the blocky LPSO phase. To determine the deformation mechanisms, activation energy, strain exponent (n) values, and strain rate sensitivity (m) of the alloys were calculated. Dispersed strengthening mechanism was predominant at lower temperatures (250°C and 300°C), transitioning to climb-controlled creep, glide-controlled creep, and grain-boundary sliding at higher temperatures (350°C and 400°C).

ACKNOWLEDGEMENT

I would want to begin by expressing my deepest appreciation to the Allmighty, the Generous and Merciful, for His Graciousness, Endless Kindness, and Divine Blessings.

I would like to convey my profound gratitude to Dr. H.M. Mamun Al Rashed, Associate Professor, MME, who is my thesis supervisor, for his kind guidance, vital advice, helpful recommendations, and constant support during this thesis effort. He provided me with invaluable advice and support from the start to finish of this thesis, and I owe him a huge debt of gratitude.

I would also like to acknowledge the Department of Materials & Metallurgical Engineering at BUET for granting us access to various laboratories and facilities in a timely manner. I extend my gratitude to all the lab personnel for their cooperation and assistance at different stages of our research work.

I am sincerely thankful to the entire faculty and staff members of the department for their support and encouragement. I would also like to express our appreciation to our well-wishers and friends for their inspiration and assistance throughout this journey.

Lastly, I would like to convey my deep appreciation and gratitude to our beloved parents and family members for their unwavering guidance, advice, and unwavering moral support. Their presence and encouragement have been a constant source of motivation. I offer my heartfelt thanks to all. May God bless each and every one of you.

Contents

Lists of Table

List of Figures

Chapter 1

Introduction

Nowadays, the high cost of fossil fuels, the upcoming scarcity of fuels, and the pollution of the environment have become a great concern for global leaders. As a greater percentage of total consumed fuel in the world is used in the transport industry, the reduction of fuel usage in this field can be one of the solutions for these global headaches. This can also contribute to a great extent to conserving our environment by emitting less amount of greenhouse gases. This cutting down on fuel usage can be achieved by reducing the weight of the automobile, as less power will be required to run the lightweight cars. In this critical circumstance, Magnesium(Mg) alloys can appear as a savior metal because of their great strength-to-mass ratio during various high-temperature structural applications. Being lightweight along with high strength, Mg alloys, as structural metals, already have drawn attention for their improved fuel efficiency [1]. So, for the economical, green, and sustainable development of mankind substantial research, on the most potential alloy like Mg, is not only necessary but obligatory.

Besides, being the lightest metal among all the engineering metals, over four times and 35% lighter than steel and aluminum respectively, it possesses excellent castability, good ductility, better vibration, and noise dampening property than aluminum [2] [3]. But for various ambient temperature processes, Mg alloys have shown limited formability, limited ductility, and strong plastic anisotropy, which offer barrier to use these alloys extensively in different industry. This shortcoming is a result of the availability of only a few slip systems in HCP metal, like Mg, at ambient temperature. The propensity of such magnesium alloys to generate and maintain a robust texture during deformation makes this constraint even more severe. All these limitations can be improved to a large extent by weakening the fiber texture and refining grain by adding alloying elements [4].

Although they are proven as potential alloys in the automobile, defense, and aerospace sectors, there are still a good number of fundamental questions to be answered, such as key factors that control the creep resistance and strength of Mg alloys, under various loading conditions nucleation as well as the growth of deformations, way of forming random orientation that is texture in wrought alloy for improving formability, the microstructural constituents and phase equilibria that is responsible for various properties of alloys. So,

intensive research has been going on to find answers to these questions that may unveil some new scopes of application of those alloys and improve the existing ones.

1.1 Motivation of this work

1. Finding out the lightest metal alloy that can serve as a superior alternative to Al-alloys while eliminating the limitations.
2. Exploring alloying elements for Mg-alloy systems that can overcome the limitations associated with previously used elements.
3. Optimizing the alloy composition to enhance multiple properties, thereby making it a cost-effective choice, as rare-earth elements are costly.
4. Investigating the influence of microstructure on mechanical properties and deformation mechanism at elevated temperature which will facilitate future Mg-alloy designing.

1.2 Objectives

1. To observe the effect of Gd on the microstructures of Mg-1Zn-1.5Y alloys.
2. To investigate the different phases formed in the Mg-Zn-Y alloy system for the different amounts of Gd content (1%, 2%, 6%).
3. To examine the influence of microstructure on tensile properties at four different high temperatures (250, 300, 350, and 400°C) and two distinct strain rates ($1x10^{-4}$ s^{-1} and $5x10^{-4}$ s^{-1}), while also investigating the deformation mechanisms at each test condition.

Chapter 2

Literature Review

2.1 Magnesium

Magnesium(Mg) is a light, silvery-white metal that belongs to the alkaline earth metals and belongs to the second major group of elements in the periodic table. Sir Humphry Davy made the discovery in 1808 by electrolyzing a combination of magnesia (MgO) and mercuric oxide (HgO) and named after the ancient Greek district of Magnesia in Eastern Thessaly where it was found first [5] . This substance, which makes up 2.7% of the crust's mass, is the eighth most prevalent element on Earth. Due to its strong reactivity, magnesium is only found in chemical compounds such as magnesite ($MgCO_3$) ore, dolomite ($Mg(CO_3)$-$CaCO_3$), sea water, and salt brine, and not in its pure elemental form in nature. [5]

Mg has a density of 1.74 g/cm^3, which is approximately one-fourth the density of steel and two-thirds that of aluminum [6]. The metal is lightweight and has excellent mechanical characteristics, such as high thermal stability, high strength-to-weight ratio, high electrical and thermal conductivity, high damping capacity, excellent machinability and castibility, which make it an attractive material for various applications, including transportation, aerospace, and biomedical engineering [7][8]. Nonetheless, the use of Mg has been restricted due to its low corrosion resistance and relatively weak mechanical properties, including low strength, low elastic modulus, limited ductility and toughness at room temperature, quick decline in strength at elevated temperatures, and poor resistance to creep [9] [10].

2.1.1 Mechanical Properties

The tensile strength of rolled sheets of pure Mg ranges from 149 MPa to 153 MPa. The range of elongation to failure is 2.9% to 3.1%. 2% compressive strength is between 69 MPa and 83 MPa, while 2% proof strength is between 83 MPa and 86 MPa. Bulk modulus, shear modulus, and Young’s modulus of this pure Mg sheet are 44.7 GPa, 17.3 GPa, and 44.7 GPa, respectively. Additionally, the vapour pressure is 6.53 x 109 Pa at 400 °C [11]. The low density and high specific strength of magnesium and its alloys make them excellent candidates for lightweight structural applications [12]. However, Mg's poor formability at room temperature presents a significant barrier to its use as a structural material. The

development of a robust basal texture during processing is what gives Mg its poor formability [13]. The three primary slip systems in magnesium are basal (0002) <11-20>, prismatic (1-100) <11-20>, and pyramidal (11-22) <11-23>, respectively [14][15]. At ambient temperature, basal slip systems have a significantly lower critical reserved shear stress (CRSS) than non-basal slip systems like prismatic and pyramidal slip systems. The basal slip systems are unable to completely accommodate the external elongation, despite tensile twinning's ability to allow lattice reorientation and further alter the degree of deformation at ambient temperature. As temperature rises, the CRSS value for non-basal slip systems rapidly falls, and activation of these slip systems enhances the formability of magnesium [16][17].

Mg's poor mechanical and corrosion qualities are primarily to blame for its limited usability in engineering. Although the low strength of many Mg alloys is a factor, the issue of poor corrosion resistance is likely to outweigh it, especially when the Mg includes a high number of impurities (e.g., Ni, Cu, Fe) or the electrolyte contains a harmful species like chloride. The aerospace industry is likely to reject new alloys with improved mechanical properties unless they also have superior corrosion resistance since poor corrosion resistance has such an impact on the viability of extended Mg use [18].

When compared to other structural metals, pure Mg has weak creep resistance. Magnesium creep mechanisms include basal slide, twinning, non-basal slip, GB shear, and migration. Twinning decreases when temperature increases the impact of GB shear, migration, and non-basal slide. With stress between 8.2 and 21 MPa and temperatures below 477^{o}C (n value shifts from 6.5 to 5.2, and Q is equal to 135 kJ mol), dislocation climb was identified as the creep mechanism by Vagarali et al., whereas above 477^{o}C, cross-slip was the mechanism for stress levels higher than 2.5 MPa (3.7 - 6.3 MPa), where stress exponent n was 6. Lattice self-diffusion, however, was found as the predominant process for stress levels less than 2.5 MPa (Q=139 kJ/mol, n=1) [19].

2.2 Alloying of Magnesium

Pure magnesium has several lucrative physical, chemical and mechanical properties but there are many problems regarding these properties. Magnesium is a common element on Earth, easy to machine, and can be recycled. However, the main challenge with utilizing more Mg alloys in automotive stems is their poor creep properties above 120^{o} C, leading to numerous studies on how the composition of magnesium alloys affects their creep

resistance. Diffusion-controlled dislocation climb and grain boundary sliding are two creep mechanisms seen in magnesium alloys. These mechanisms vary depending on the kind of alloy, the microstructure, the stress and temperature conditions, and other variables [20]. Due to its low cost, low density, and potent ability to strengthen magnesium, aluminum is the most popular alloying element. Rare-earth metals are now used as alloying components because they can enhance the required qualities. Additionally, alloying elements including Zn, Zr, Sn, Mn, Si, Cr, and W are employed to enhance the characteristics of pure magnesium.

Cast and wrought magnesium alloys are the two categories of Mg alloys. The most common Mg alloys on the market are those in the AZ series (Mg-Al-Zn), AM series (Mg-Al-Mn), AE series (Mg-Al-RE), EZ series (Mg- RE- Zn), ZK series (Mg-Zn-Zr), and WE series (Mg-RE-Zr). According to statistics, casting processes—particularly different die-casting techniques—are used to create more than 90% of the structural components made of Mg alloy.

2.2.1 Microstructure of Mg Alloys

The microstructure of Mg alloys is a fundamental aspect that influences their mechanical properties, corrosion resistance, and other characteristics. The microstructure refers to the internal structure of the material, which encompasses its crystal structure, grain size, texture, and the distribution of secondary phase particles or intermetallic compounds. The unique properties of Mg and the complex interactions between the primary Mg matrix and various secondary phase constituents make the microstructure particularly significant in Mg alloys [21] [22]. Therefore, for the development of new alloys with enhanced properties and for the improvement of existing alloy operations, knowing the microstructure of Mg alloys is crucial.

To develop new Mg alloys with improved properties and optimize the processing of existing ones, it is necessary to comprehend the complex interactions between the primary magnesium matrix and various secondary phase constituents, such as second phase particles, intermetallic compounds, or precipitates. The type, size, and distribution of these secondary phases have a profound impact on the mechanical properties of the alloy. Furthermore, the hexagonal close-packed (HCP) crystal structure of Mg gives rise to unique deformation mechanisms and texture development during processing and deformation, which also influence the microstructure and, subsequently, the properties of the alloy.

2.2.2 Designation of Mg Alloy

For the Mg industry, the ASTM (American Society for Testing and Materials) devised a widely used coding system. A coding system that is 'letter-letter-number-number-number' is used in this case. The two primary alloy elements are identified by the letters, which are listed in a decreasing sequence of content. They are ordered alphabetically when both alloying elements are found in the same quantity. Table 2 lists the code letters that are used to designate the alloying elements. The two numbers are adjusted to the closest whole number and are presented in the order that they are found. They represent the weight percentage of the two primary alloying elements. The fifth symbol is a letter indicating the alloy modification, and the designation of temper is included as well. The alloy code is followed by a designation of temper. The temper designation system of Mg alloys is similar to the Temper designation of aluminum alloys:

F –As fabricated;

O – Annealed;

H – Cold worked;

T4 – Solution treatment;

T5 – Artificial aging;

The temper designation for Mg alloys is similar to that of aluminum alloys. For instance, an alloy designated as ZE63A-T6 is a magnesium alloy containing approximately 6% zinc (symbol Z) and 3% rare earth elements (symbol E), with the modification of the alloy being A. The temper designation for this alloy is solution treatment followed by artificial aging (T6) [23].

Table 2.1 Symbol of Alloying Elements

A: Aluminum	B: Bismuth	C: Copper	P: Lead
E: Rare-earths	F: Iron	N: Nickel	D: Cadmium
L: Lithium	M: Manganese	H: Thorium	K: Zirconium
W: Tungsten	R: Chromium	S: Silicon	T: Tin
Q: Silver	Z: Zinc		

2.2.3 Effect of Alloying Elements in Magnesium

Pure magnesium's characteristics can be changed by adding alloying elements. Magnesium has a high chemical activity and can generate intermetallic compounds by reacting with other metallic alloying elements. Intermetallic phases can be seen in the majority of magnesium alloys. These phases help to modify the microstructure of the magnesium alloys, which in turn affects their mechanical properties. The main mechanisms to improve the mechanical performance of magnesium-based materials are solid solution hardening and/or precipitation hardening.

The next section discusses how magnesium is affected by the addition of main metallic elements.

Table 2.2 Effect of Alloying Elements on Magnesium [5]

Alloying Element	Effect on Mechanical Properties
Aluminum	Improved and Enhanced Hardness and Strength Degradation of Ductility
Calcium and Berylium	Reduction of Oxidation
Cerium	Improved Corrosion Resistance Degradation of Yield Strength
Copper	Improve in Strength Degrade in ductility
Nickel	Improve in Yield and Ultimate Strength Degradation in Corrosion Resistance and Ductility
Silicon	Enhancement of Corrosion Resistance
Zinc	Enhancement of Corrosion Resistance
Li	Enhanced ductility, formability, Stiffness and strength
Rare Earth Metals	Improvement in Strength, Corrosion Resistance and High-Temperature Creep Resistance

Among all alloying elements effect of Zinc, Gadolinium and Yttrium are elaborately discussed below:

Zinc(Zn)

Zn has a major influence on the microstructural and mechanical properties of magnesium and its alloys. The as-cast Mg-Zn alloys' grain size was greatly refined by the addition of Zn, and the volume percent intermetallic in the microstructure increased. The volume percentage and presence form of secondary phases had a significant impact on the tensile characteristics and corrosion resistance of Mg-Zn alloys. The inclusion of Zn in magnesium-rare earth (Mg-RE) alloys results in the development of phases with a distinct structure known as long-period stacking ordered (LPSO). These LPSO phases are crucial for achieving high strength in magnesium alloys while maintaining good ductility [24]. Despite the presence of the potentially harmful MgZn intermetallic, corrosion resistance increased with increasing Zn concentration in the range of 1–5 wt%, according to corrosion morphologies, immersion testing, and electrochemical studies. A network structure of MgZn intermetallic served as the cathode as a result of excessive Zn addition exceeding 7 wt%, which accelerated micro-galvanic corrosion. It was suggested that the addition of Zn content needs to be carefully controlled in order to enhance the mechanical characteristics and corrosion resistance of Mg alloys [25].

According to J. Yuan et al., the 14H-LPSO phases impede the nucleation and growth of dynamic recrystallization grains during extrusion. As a result, as the Zn content rises, the proportion of deformed grains gradually goes up while the fraction of dynamic recrystallization grains declines. The subsequent aging heat treatment of the extruded alloys shows that the addition of Zn reduces the precipitation of beta phase being consumed by the LPSO structures which results in the degradation of hardness. With increasing Zn composition, the strengths of the as-extruded alloys substantially rose and maintained high elongation. In the 0.5 wt% alloy, the texture of the (0001) basal fiber is significantly stronger. However, it has been shown that as the Zn content increased, the strength of the peak-aged alloys fell, and their elongation increased [26].

Gadolinium(Gd)

The microstructure and characteristics of pure Mg and its alloys can be improved by Gd, according to research. According to Jiang Nan et al., the microstructure of the AZ80 alloy with more than 0.6 weight percent Gd addition showed the presence of new block-shaped Al_2Gd phases. The first rod-shaped $Al_{11}RE_3$ phase may be inhibited by the presence of Gd while the block-shaped Al_2Gd phase may be precipitated. As a result, the mechanical

characteristics of the alloy have greatly improved [27]. Primary Mg_2Si in the Mg-3 wt% Si alloy can be effectively changed and refined using an appropriate amount of Gd, according to Lingying et al. The average size of the primary Mg_2Si significantly dropped and then gradually increased when Gd concentration was raised up to 1.0 weight percent. Its morphology changes throughout this time from coarse dendrite to fine polygon. The Gd content must be at least 1.0 weight percent to get the best modification effect, which is primarily due to the poisoning effect. The $GdMg_2$ phase in the main Mg_2Si obviously becomes coarser and aggregates when the Gd level increases above 2.0 weight percent [28].

Mg alloys containing Gd have excellent corrosion resistance. Alloys can therefore be applied in the biomedical field. According to Aneta et al.'s analysis, Mg-4Ca-1Zn alloys have significantly better corrosion resistance as Gd content has increased. In contrast to the E_{OCP} potential, the alloys' corrosion potential (E_{corr}) went towards positive values. The electrochemical corrosion rates and the corrosion rates seen over the course of 8 hours of immersion trials in an aggressive environment agreed. The developed H2 volume after 1 and 8 hours of immersion demonstrated the strong corrosion resistance of the alloy with 2 wt% Gd [29].

As Gd concentration rises, Mg alloys' creep resistance gets better. It is demonstrated that the primary, secondary, and tertiary creep regions are no longer visible in alloys containing high amounts of Gd, and that the tertiary creep zone in the Y9K alloy is reached very quickly after the creep test has begun [30].

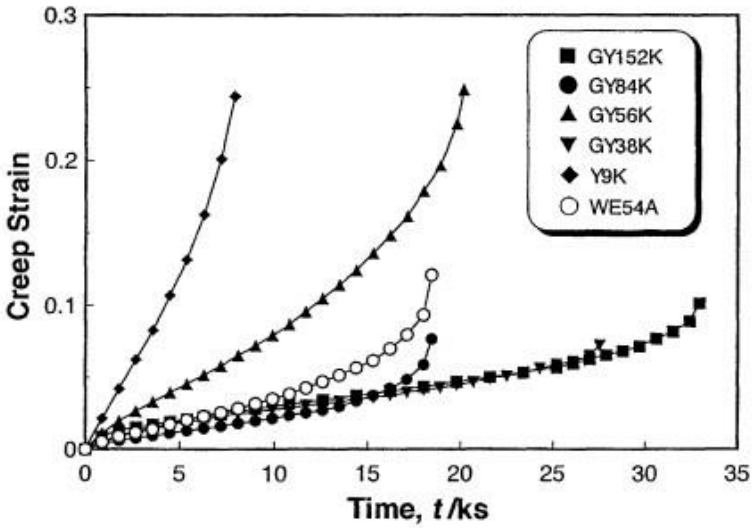

Figure 2.1: Creep curves of different alloys. Creep test was carried out at a temperature of 300oC and a stress of 100 MPa [30]

2.3 Binary Alloy System of Mg

2.3.1 Mg-Zn Binary Alloy System

The binary phase diagram for zinc and magnesium is shown in Figure 2.2. When Zn is present at a concentration of 66.7 at.%, it acts as a grain refiner, forming the stable intermetallic $MgZn_2$, which has a high melting point of 862 K. The system is characterised by two eutectic reactions, four peritectic reactions, one eutectoid reaction, and a compound that melts congruently. At 614 K and 28.9 at% Zn, the Mg-rich eutectic point is located, while 640 K and 92.9 at% Ca are the locations of the Zn-rich eutectic point [31]. Eutectics with low melting points enable liquid to develop during sintering, which may hasten the capillary action of zinc to disrupt a greater area of Mg surface layer. According to Mg solidus curve, Zn is the most soluble in Mg at 2.5 at.% Zn at 613 K and the highest solubility of Mg in Zn is very negligible that is 0.3 at.% Mg at 637 K temperature [31].

Table 2.3 Different Reactions at various composition and temperature in Mg-Zn Binary Alloy System [31]

Reaction Type	Reaction	Composition (at.%Zn)	Temperature (K)
Eutectic	$L \leftrightarrow Mg_{51}Zn_{20} + Mg_{12}Zn_{13}$	28.9	614
	$L \leftrightarrow Mg_2Zn_{11} + Zn\_Hcp$	92.9	640
Peritectic	$L + Zn\_Hcp \leftrightarrow Mg_{51}Zn_{20}$	28.9	614
	$L + Mg_2Zn_3 \leftrightarrow Mg_{12}Zn_{13}$	29.7	620
	$L + MgZn_2(Laves\_C14) \leftrightarrow Mg_2Zn_3$	37.1	689
	$L + MgZn_2 (Laves\_C14) \leftrightarrow Mg_2Zn_{11}$	90	654
Congruent	$L \leftrightarrow MgZn_2$ (Laves_C14)	66.7	862
Eutectoid	$Mg_{51}Zn_{20} \leftrightarrow Mg\_Hcp + Mg_{12}Zn_{13}$	28.1	599

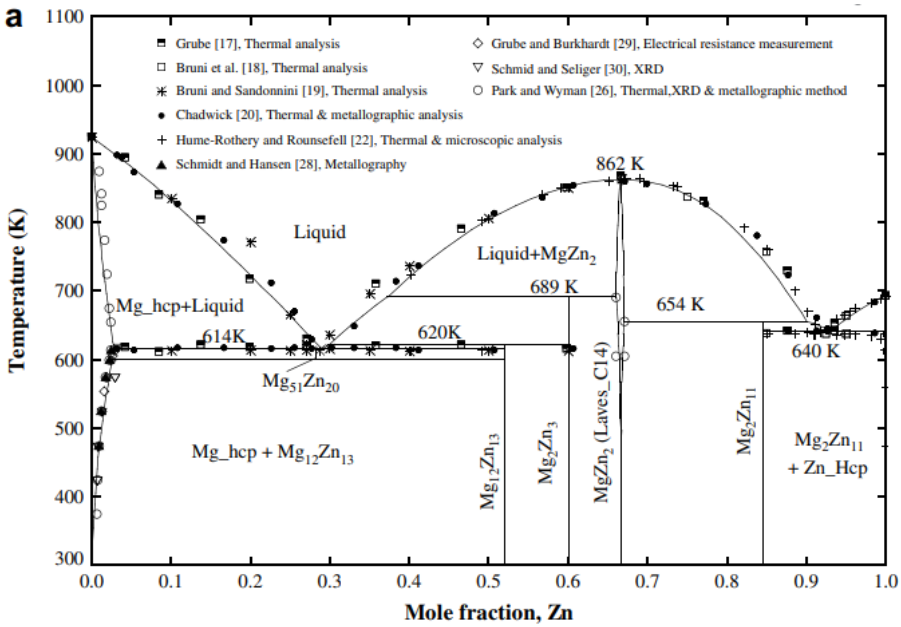

Figure 2.2: Binary Phase Diagram of Mg-Zn [31]

2.3.2 Mg-Y Binary Alloy System

The Mg-Y binary phase diagram, as depicted in Figure 2.3, provides a comprehensive understanding of the various phases that form within the system at different temperatures and compositions. This diagram reveals the presence of multiple secondary phases, each associated with specific reactions. In particular, the formation of these secondary phases is attributed to three peritectic reactions, two eutectic reactions, and one eutectoid reaction. Within the Mg-Y binary system, three distinct compounds are observed, each with its own narrow homogeneity range. These compounds include $Y_{1-x}Mg(\gamma)$, $Y_{1-x}Mg_2(\delta)$, and $Y_{5-x}Mg_{24}(\varepsilon)$. [32] The composition of these compounds varies depending on the specific temperature and composition conditions within the system. The presence of these secondary phases and the reactions involved in their formation play a crucial role in determining the overall behavior and properties of the Mg-Y alloy system. Understanding these phase transformations and their corresponding conditions is essential for designing and optimizing alloy compositions with desired properties for various engineering applications.

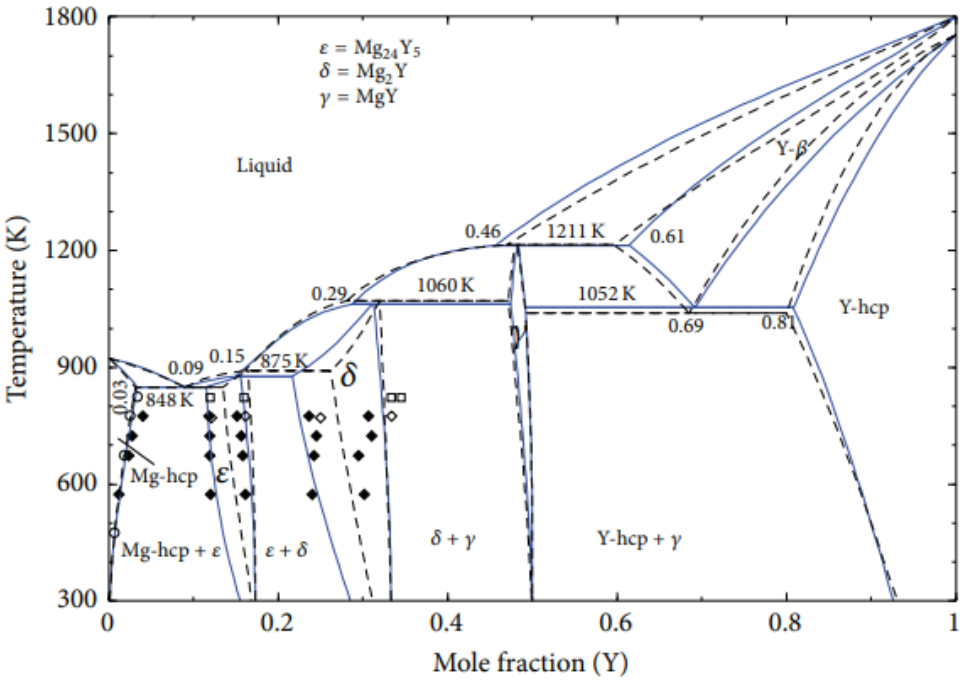

Figure 2.3 Mg-Y Binary Phase Diagram [33]

The intermetallic phases were analyzed using single crystal X-ray diffraction, allowing for the determination of their respective homogeneity ranges. It was found that $Y_{1-x}Mg$ has a homogeneity range of 50-52 at.% Mg, $Y_{1-x}Mg_2$ has a range of 65.8-66.8 at.% Mg, and $Y_{5-x}Mg_{24}$ has a range of 84-87.5 at.% Mg. Another study reported a broader homogeneity range for $Y_{1-x}Mg_2$, spanning from 66.7 to 74.0 at.% Mg [32].

Table 2.4 Different Reactions at various composition and temperature in Mg-Y Binary Alloy System [32]

Reaction Type	Reaction	Temperature (K)
Peritectic, p_1	L + Y-β(bcc) ↔ $Y_{1-x}Mg$	1213
Peritectic, p_2	L + $Y_{1-x}Mg$ ↔ $Y_{1-x}Mg_2$	1058
Peritectic, p_3	L + $Y_{1-x}Mg_2$ ↔ $Y_{5-x}Mg_{24}$	890
Eutectoid	Y-β(bcc) ↔ Y-α(hcp) + $Y_{1-x}Mg$	1048
Eutectic	L↔ $Y_{5-x}Mg_{24}$ + Mg	839

2.3.3 Mg-Gd Binary Alloy System

Manfrinetti and Gschneidner [34] conducted a comprehensive investigation of the Mg-Gd binary phase diagram across the entire composition range. Their study incorporated thermal analysis, metallographic examination, and X-ray analysis.

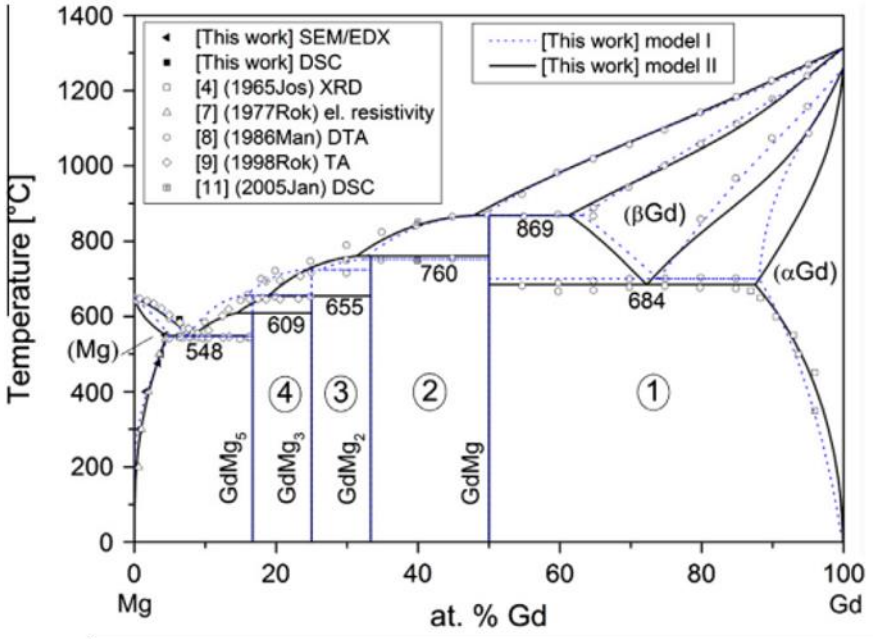

Figure 2.4 Mg-Gd Binary Phase Diagram [34]

Table 2.5 Different Reactions at various composition and temperature in Mg-Gd Binary Alloy System [34]

Reaction Type	Reaction	Temperature (^oC)	Composition of Phases at.%Gd (as Sequence in Reaction)		
Eutectic	L ↔ (Mg) + $GdMg_5$	548	8.3	4.6	16.6
Peritectic, p_1	L + $GdMg_3$ ↔ $GdMg_5$	609	14.5	25	16.6
Peritectic, p_2	L + $GdMg_2$ ↔ $GdMg_3$	655	18.9	33.3	25
Peritectic, p_3	L + GdMg ↔ $GdMg_2$	760	31.3	50	33.3
Peritectic, p_4	L + β-Gd (bcc) ↔ GdMg	869	47.9	61.3	50
Eutectoid	β-Gd (bcc) ↔ α-Gd (hcp) + GdMg	684	72.2	87.5	50

Through these techniques, they identified four intermetallic compounds, namely $GdMg_5$, $GdMg_3$, $GdMg_2$, and GdMg. These compounds were found to be formed through a series of peritectic reactions. At the eutectic temperature of 548^o C, the maximum solubility of Gd

in Mg is determined to be 4.6 atomic percent (at.%). The Mg-Gd binary phase diagram, represented in Figure 2.4 , offers a comprehensive overview of the phases that emerge within the system across various temperatures and compositions. This diagram provides valuable insights into the existence of multiple secondary phases, each of which corresponds to specific reactions. Table 2.5 presents a detailed overview of the reactions associated with different temperatures within the Mg-Y binary system. These reactions correspond to the formation of various phases.

2.4 Effect of Various Heat Treatment Process on Microstructural Evolution

Mg alloys can undergo several essential heat treatment procedures: stress relieving, homogenization, solution treatment, annealing, and age hardening. Stress relieving is implemented at temperatures above 120°C to mitigate residual stress, which has the potential to cause dimensional distortion, cracking, and stress corrosion. This procedure is particularly important for wrought alloys following various forming techniques like extrusion and rolling. It is also necessary for castings due to their interaction with the mold during solidification, as well as for welds in both cast and wrought alloys. Annealing is performed at temperatures approximately around 300°C to promote the process of recrystallization within the volume of the material. This recrystallization compromises the alloy's strength while significantly improving ductility. The primary purpose of annealing is to support specific stages of the manufacturing process.

Solution annealing, known as T4 treatment, is a heat treatment procedure employed to dissolve phases that exist in an alloy subsequent to casting or forming. This results in the formation of a supersaturated solid solution. The alloy is subjected to elevated temperatures, typically ranging from 380-530° C, for a duration of 4 to 24 hours, surpassing the solvus line. Similarly, direct artificial aging, referred to as T5 treatment, involves the generation of precipitates from elements already present in the solid solution subsequent to casting or forming. This process is commonly carried out following solution annealing. It entails heating the alloy at temperatures of 130 to 230° C for a period of 5 to 50 hours. The combination of solution annealing and subsequent aging, known as T6 temper, is a critically important thermal method utilized to enhance the mechanical properties of magnesium alloys. This two-step process involving solution annealing to dissolve phases and

subsequent aging to precipitate desired elements leads to significant improvements in the alloy's mechanical characteristics.

The heat treatment procedures for magnesium alloys are outlined in the ASTM B661-06 Standard. This standard has been established to provide guidelines for appropriate practices that ensure the attainment of desired physical and mechanical properties in magnesium alloys.

2.4.1 Age Hardening

Age hardening is a process in metallurgy that involves the hardening of a material by aging it at an elevated temperature for a specific amount of time, which results in the formation of precipitate particles that hinder the motion of dislocations within the material, thereby increasing its strength and hardness. The crucial factors of age-hardening are time and temperature. The aging temperature determines the type and size of the precipitates formed, while the aging time affects their distribution and density. It is important to carefully control these parameters to achieve the desired mechanical properties and microstructure in the alloy [35].

In a study, aging of the GW62 alloy at a 175^{o} C temperature resulted in a sequence of precipitation, with the β" phase precipitating first, followed by β' phase until peak aging, and the final transformation of β' phase into β_1 and β phases during over-aging hence the change in mechanical properties also observed [36]. In another study, Beladi and Barnett [37] examined how different pre-treatments applied to WE54 influenced its deformation that is compressive one at temperatures ranging from 25 to 450^{o} C , with a strain rate of 0.01 s^{-1}. The findings revealed that when peak aged samples were subjected to hot working, the process of dynamic recrystallization was hindered due to the effects of solute drag and/or Zener pinning.

Temperature also plays a crucial role in the aging process of alloys, as evidenced by a study which revealed that the highest hardness of GW62 alloy was achieved at 175° C aging temperature, compared to 200° C and 225° C [36].

2.4.2 Solid Solution Treatment

Solid solution treatment, also known as solutionizing, is a metallurgical process that involves heating a metal alloy to a high temperature to dissolve its various constituent elements into a single homogenous phase, creating a solid solution. This process is used to

improve the machinability, formability, and ductility of the alloy, and to facilitate subsequent heat treatment processes like age hardening.

The critical aspects of solid solution treatment include temperature and time, which determine the extent of solute diffusion and hence the resulting microstructure of the material. Higher temperatures and longer treatment times can lead to the complete dissolution of the solute and the formation of a homogenous structure [36]. However, excessively high temperatures or long treatment times may lead to grain growth, coarsening of the microstructure, and other undesirable effects. In a study [38] involving Mg-1.8Zn-0.8Y-0.8Gd and Mg-0.9Zn-0.8Y-0.8Gd (at%) alloys, it was discovered that the solution treatment significantly improved the elongation, while causing a sharp degradation in the ultimate tensile strength (UTS) of the alloys. Therefore, it is important to optimize the solid solution treatment conditions based on the specific material and desired properties.

Solid solution treatment can result in either softening or hardening, depending on several factors including the type and concentration of solute atoms, their interaction with the solvent atoms, and the misfit between the solute and solvent atoms in terms of size and modulus, as well as valency effects [39]. For instance, a study by [40] found that Mo and Re had a softening effect on ternary Nb alloys, while other studies [41] have shown that Y and Gd produce much higher solid solution strengthening in Mg alloys compared to Al and Zn.

2.4.3 Homogenization

Homogenization is a thermal treatment process that is applied to an alloy in order to obtain a uniform distribution of its constituent elements. During homogenization, for a long time, the alloy is heated to an elevated temperature, which causes the constituent elements to diffuse and redistribute themselves throughout the alloy.

The crucial factors affecting homogenization include the temperature and duration of the treatment, as well as the composition and microstructure of the alloy. An investigation on the effect of homogenization duration on the microstructure and mechanical properties of AZ91 alloy revealed that a longer duration of 100 hours resulted in a more uniform distribution of precipitation and increased dynamic recrystallization, leading to improved tensile strength and elongation compared to a shorter duration of 21 hours [42]. Therefore, the temperature and duration of the homogenization process should be carefully selected to ensure that the alloy reaches a sufficiently high temperature to allow for diffusion of the

constituent elements, while also avoiding any detrimental effects that may occur from prolonged exposure to high temperatures. The composition and microstructure of the alloy also play a role in the homogenization process, as the presence of certain alloying elements or specific microstructural features may influence the homogenization kinetics and resulting microstructure.

2.5 Deformation of Mg Single Crystal

At ambient temperature, the predominant deformation process for single-crystal Mg is basal dislocation slip. Due to constraints imposed by nearby grains, the situation varies in polycrystalline magnesium [43]. Mg has a hexagonal close-packed (HCP) crystal structure. The fundamental hexagonal unit cell has three axes (a=b≠c) and associated angles (α=β=90°, γ=120°). Two atoms are arranged in a single primitive hexagonal unit cell to produce a double lattice. Consequently, in the ideal case, ABABAB is the stacking order of the HCP structure in the c direction (atom layers of black and cyan in Figure 2.5**:** HCP structure and primitive unit cell containing 2 atoms and the Thomson-tetrahedron [44]).

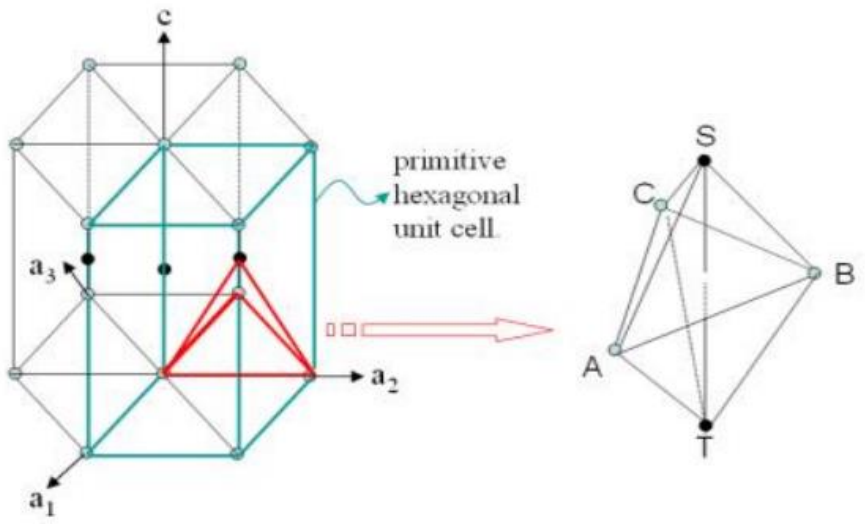

Figure 2.5: HCP structure and primitive unit cell containing 2 atoms and the Thomson-tetrahedron [44]

The asymmetry of the atom array is the primary distinction between (FCC) and HCP in terms of crystallography. In the case of FCC, the cubic system defines the unit cell, however the cubic system should not be applied to HCP. Typically, the four-axes Millier-Bravais notation has been used to denote the planes and indices of directions in HCP structures. The vectors a_1, a_2, a_3 and c constructed the four-axis system, that is shown in Figure 2.5, where a_3 is redundant because it equals $-(a_1 + a_2)$.

The deformation behavior of a material is influenced by two key material characteristics. The ratio of c/a is one of the characteristics. The a and c axes are typically shown as being the closest to the atom center, respectively. The most optimal axial ratio to use is $\sqrt{8/3}=1.633$. However, this desirable c/a ratio is not found in any pure metal. Depending on c/a ratio, certain metals, including Zr and Cd, exhibit twinning-dominant deformation when compression is applied along the c axis, while Mg and Be require tensile load to undergo twinning. The elastic modulus is another key characteristic that influence deformation behavior [44].

2.5.1 Role of Slip Plane

Slip is a term used to describe the plastic deformation of metals that normally occurs when dislocations move across the crystal lattice and cause crystal blocks to slide along defined crystallographic planes, or slip planes [44]. Only when the applied shear stress surpasses a threshold value of shear stress known as the critical resolved shear stress, or CRSS, can it frequently happen in close-packed planes and close-packed directions. Despite the fact that HCP metals are possible to have more twining and slip systems, it is discovered that Mg is largely deformed by one twinning system and four slip systems [44].

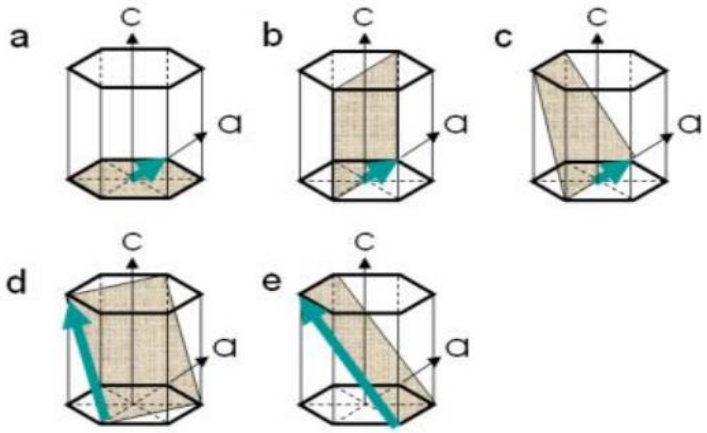

Figure 2.6: Slip Systems of Magnesium. (a) Basal, (b) Prismatic, (c) Pyramidal ‹a›, (d) Pyramidal ‹c+a› and (e) Tensile Twin Slip System. [44]

Table 2.6 Slip/Twin Plane and Direction of Twin System and 4 Slip System [44]

Type	Twin/Slip Plane	Twin/Slip Direction
Basal Slip	(0001)	$[11\bar{2}0]$
Prismatic Slip	$(00\bar{1}0)$	$[11\bar{2}0]$
Pyramidal Slip	$(10\bar{1}1)$	$[11\bar{2}0]$

Type	Twin/Slip Plane	Twin/Slip Direction
Pyramidal Slip	$(11\bar{2}2)$	$[\bar{1}\bar{1}23]$
Twinning	$(10\bar{1}2)$	$[10\bar{1}1]$

The five Mg deformation modes are depicted in Figure 2.6. The basal, prismatic, pyramidal ‹a› and pyramidal ‹c+a› slip systems are shown in Figure 2.6 (a), (b), (c), and (d), respectively, while the tensile twin system is shown in (e).

Dislocations with a particular Burgers vector move along specified slip planes to undergo slip deformation. Together, these Burgers vectors and slip planes make up a slip system, and active slip systems have a big impact on how the material deforms. The Burger Vectors, Slip Plane, and Direction are shown in Table 2.6. The basal, prismatic, and pyramidal ‹a› slip systems all have ‹a› Burger vectors, however the pyramidal ‹c+a› slip system's Burger vector is ‹c+a›. As a result, the pyramidal ‹c+a› slip system's Burger vector has a higher energy than those of the other slip systems, making it less stable energetically [44].

The easiest direction of slip occurs on the basal plane, in the close packing ‹a› direction (1 210), which is also the most typical slip system in other hcp metals. In magnesium, where atom densities are maximum, slip primarily occurs on surfaces with large spaces and on directions with the smallest lattice translation vectors. To obtain uniform, generalized ductility, a minimum of five independent slip systems must be present. There are two separate slip modes in both the basal slip system and the prismatic slip system. Another deformation mode could result from the twin's ability to accommodate strain [44].

Crystallographic slip most frequently occurs in magnesium alloys in the $[11\bar{2}0]$ direction on the (000l) basal plane, which is the closely packed plane, at room temperature (Figure 2.7).

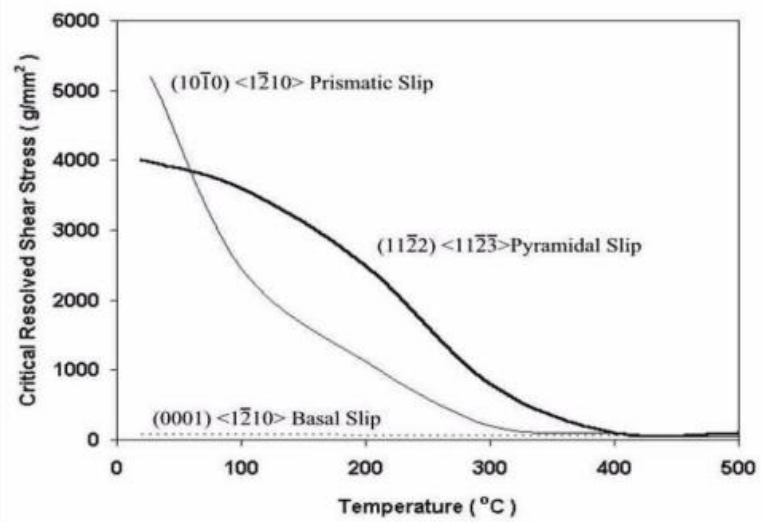

Figure 2.7: The Variation of CRSS of Mg for Pyramidal Slip, Prismatic Slip, and Basal Slip with Changing Temperature [45]

On the $(10\bar{1}0)$ vertical face planes, prismatic slip happens in the $[11\bar{2}0]$ direction, whereas on the $(10\bar{1}1)$ planes, pyramidal slip develops in the $(11\bar{2}0)$ direction. On the $(11\bar{2}2)$ planes, pyramidal slip [c+a] occurs in the $[\bar{1}\bar{1}23]$ direction [45]**.** The ductility of magnesium is improved by these additional slip systems. As a result, basic manufacturing techniques are frequently performed at high temperatures.

Magnesium has been found to exhibit $(11\bar{2}2)$ $[\bar{1}\bar{1}23]$ pyramidal slip, allowing it to slip off of the basal plane. The system was discovered to be functional from ambient temperatures to 500°C; however, due of its larger CRSS than other slip systems that are functional beyond ambient temperature, it can only be seen in deformation of single crystals, compression along c-axis, under the limited orientation [45]**.**

2.5.2 Twinning

The behaviors of both flow and fracture are significantly influenced by twinning. Stress accumulations brought on by the dislocation slip's anisotropic nature are the main source of twin induction [43]. Also, slip process can be reversed while twinning is a kind of polar mechanism that cannot be reversed. Twinning is accomplished by the atoms translating to accommodate deformation. However, understanding twinning is essential since it is an important deformation mode at room temperature with basal slip. Compared to the twin propagation stress, the stress of twin nucleation is significantly higher. As a result, twin can easily form in a zone of concentrated stress, such as at a grain boundary. The crystal is reoriented by Twin. In the instance of the tensile twin of Mg, the misorientation is roughly

87.3°. But that does not mean that the atom array undergone a substantial degree of translation. The crystallographic orientation can only be altered by a small-scale atomic translation. In reality, even if the twin's direct contribution to plastic strain in polycrystalline systems is not very significant, the twin can nevertheless have a significant impact by altering the crystal's crystallographic orientation to one that favors dislocation-slip interactions. Due to the lack of a grain boundary in mono-crystalline magnesium, once a twin occurs, practically the entire volume is twinned. As a result, in a single crystal, the twin's impact is much greater. The purity of the metal has an impact on the twinning deformation mechanism. Depending on the size of the sample, the twinning behavior can vary. Twins can form at various locations on the bulk scale, where they eventually intersect after propagating. The sample's stress field became heterogeneous as a result, which allowed for the creation of secondary twins. On the other hand, when twinning occurs at a small scale, it propagates promptly and nearly the entire sample is twinned [46].

In HCP metals, many twinning modes have been researched. In magnesium alloys, main deformation twins typically come in three different varieties. The sorts of twins and twinning planes involved in the creation of primary twins are related to the preliminary texture of the metal samples. Because magnesium has a smaller c/a ratio than is ideal, extension twins (ETs) can be produced when a compressive load is exerted perpendicular to c-axis. On the other hand, contraction twins (CTs) occur when a compressive load exerted along the c-axis [47]. A hardening effect and sigmoidal shaped compression curve were produced by the growth of ETs in an AZ31 alloy, according to Jiang et al. The CTs rotate the basal planes either 56 or 64 degrees. As a result, basal glide is facilitated and has a softening effect. ETs produce more significant textural changes when compared to glide and CTs [47].

Again, based on their shape, twins can be divided into two groups: narrow banded types and wide lenticular types. In the beginning stages of deformation, $\{10\bar{1}2\}$ twins occur known as the wide twins and small surface height evolution results from that twinning. The narrow twins, designated $\{10\bar{1}1\}$ or $\{30\bar{3}2\}$, are present during the last stages of deformation and come with a significant alteration in surface height. The development of narrow twins appears to result in shear deformation that is extremely localized within the twin, which eventually causes strain incompatibility and ultimate failure [43]. A twin's activation is influenced by the direction of the stress being applied as well as the crystal's

c-axis's expansion or contraction. Although twinning only offers a little amount of strain, it offers an additional independent method of deformation in Mg.

2.6 Deformation Mechanism of Mg Polycrystal

A common metal-forming method that results in significant texture evolution is cold rolling. As plastic deformation during cold rolling increases, it is primarily responsible for basal plane alignment along the rolling direction (RD) [48][46]. This deformation occurs during rolling and is characterized by superimposed shear and compressive forces [46]. The complexity of Mg's lattice structure is frequently described by a limited number of twin and slip systems, the selection of which may result in distinct material behavior.

In previous study, it was observed that at a temperature of 473 K, the primary mechanism of deformation involves prismatic <a> slip, contributing to the preservation of the initially robust [0110] crystallographic texture. However, as the temperature increases to 673 K, pyramidal <c + a> slip becomes activated due to thermal energy, resulting in a multi-slip phenomenon known to have a weakening effect on the material's texture [49].

2.6.1 Role of Slip Plane and Stacking Fault Energy

Slip planes denote specific crystallographic planes within a crystalline material, along which dislocations – imperfections in the atomic arrangement – move during mechanical deformation. This movement along slip planes is fundamental for enabling plastic deformation, allowing materials to yield without breaking. The choice of slip planes, along with the ease of dislocation motion on these planes, significantly impacts a material's mechanical behavior. Stacking fault energy (SFE), on the other hand, characterizes the energy associated with deviations from the perfect stacking sequence of atomic layers in a crystal lattice. It quantifies the propensity for stacking faults – irregularities in the stacking order – to form within a material. A high stacking fault energy implies that stacking faults are less favorable, resulting in a more ordered lattice. Conversely, a low stacking fault energy encourages the formation of stacking faults, leading to a more disordered structure. Slip planes and stacking fault energy (SFE) are two of the most crucial concepts that play a very important role during the plastic deformation of alloys.

From a previous study, the enhanced ductility observed in solid solution Mg–Y alloys is linked to a notable increase in the occurrences of pyramidal <c + a> dislocation slip, $\{10\bar{1}1\}$ $<10\bar{1}2>$ contraction twinning, and $\{10\bar{1}1\}$ $\{10\bar{1}2\}$ secondary twinning [48]. Some

studies ([50]) have found out that secondary twinning plays a role in crack initiation, while pyramidal dislocation slip is crucial for accommodating strain along the <c>-axis, thereby leading to more compatible deformation [51] [52]. Another research finding have shown that the increased non-basal shear activities in Mg–Y alloys coincide with a substantial reduction in I_1 stacking fault energy (SFE). It is conjectured that this adjustment in the I_1 SFE serves as the fundamental rationale behind the heightened engagement of pyramidal deformation mechanisms in Mg–Y alloys, enabling the activation of dislocation sources for <c + a> dislocations [53].

Prior investigations [54] [55], encompassing both theoretical calculations and experimental work, have consistently indicated a notably elevated stacking fault energy (SFE) in pure Mg. In experimental observations of pure Mg subjected to recrystallization and mild room-temperature deformation, the absence of I_1 and I_2 stacking faults was evident. This absence implies infrequent dislocation dissociation and the presence of narrow spacing (measuring 61 nm) between partial dislocations, collectively signifying a heightened SFE [56] [57].

Prior research [58] conducted by various authors has drawn the conclusion that the limited room-temperature ductility of magnesium arises primarily from the constraint imposed on basal dislocation slip. They have posited that enhancing the likelihood of basal dislocations transitioning to prismatic planes within magnesium could potentially ameliorate ductility. To achieve this, they proposed introducing elements that would elevate the I_2 stacking fault energy (SFE), thereby increasing the probability of cross-slip among basal dislocations [53]. In contrast, a separate study involving TEM observations of Mg-Y alloy revealed a reduced I_2 SFE, which would lead to (i) diminished chances of cross-slip for basal dislocations and (ii) a less mobile configuration for basal dislocations. Consequently, this could result in a relatively higher degree of activation for non-basal deformation and, as a consequence, an increase in strength. Furthermore, the study's theoretical and experimental investigations indicated a reduced I_1 SFE concurrent with enhanced cross-slip on pyramidal planes, leading to improved ductility [53].

A study has proposed [53] that the primary driver behind the increase in ductility within the Mg–Y system is the alteration of the I_1 stacking fault energy (SFE), and this influence manifests in the following ways: (i) The augmentation in ductility can be attributed to the heightened activity of pyramidal <c + a> dislocations since slip modes out of the basal plane constitute a principal mechanism for enhancing the ductility of Mg alloys, aligning with the von Mises criterion for compatible deformation. (ii) The initiation of <c + a>

dislocations, pivotal for generating shear outside of the basal plane, is closely linked with the presence of the I_1 stacking fault. This sessile I_1 stacking fault, whose energy decreases with Y alloying, is secured by pyramidal partial dislocations. This structural phenomenon facilitates the creation of dislocation arrangements on pyramidal planes. In accordance with Yoo et al.'s nucleation model [59] , it was proposed that the I_1 stacking fault acts as a heterogeneous nucleation source for pyramidal <c + a> dislocations. (iii) The observed (via TEM) and computed (using DFT) reduction in I_1 SFE due to the introduction of Y results in the formation of stable SFI_1 in Mg–Y alloys, which, in turn, provides sources for <c + a> dislocations [53].

2.6.2 Grain Boundary Sliding

Because there aren't enough slip systems to provide Mg alloys their full ductility, it is grain boundary sliding (GBS) which has been seen as a deformation process that enables strain in the c-axis direction. GBS can promote ductility, but only when the temperature is sufficiently high and the grain size is small. It was discovered that a similar mechanism of intense shearing in the GB region occurs at lower temperatures as well. This mechanism does not promote ductility and instead causes fracture at the grain boundary [43].

2.6.3 Formability of Mg Alloy

Due to significant mechanical anisotropy, it has been discovered that Mg alloys, in particular AZ31 and ZK60, have poor ductility and formability at room temperature. This anisotropy is attributable to the strong texture produced by thermo-mechanical processing, which led to the establishment of a preferred orientation inside the hexagonal close-packed crystal structure [60]. When it comes to sheet metal and extruded goods, the bulk of grains have their basal plane oriented along to the rolling direction and along the extrusion direction. Weakening this basal texture has been shown to significantly improve the formability of Mg alloys, enabling sustained strain hardening behavior and promoting uniform deformations before plastic instability occurs [60].

Recent studies have shown that the addition of rare earth (RE) elements, such as yttrium (Y) and neodymium (Nd), can effectively weaken the texture of Mg alloys. Techniques like multi-pass rolling or post-deformation annealing have been found to induce texture weakening in RE-containing alloys [53]. The reduction of stacking fault energy, solute drag/pinning effect, precipitate formation, and the development of local short-range

ordered clusters are some of the mechanisms proposed to explain the occurrence of texture weakening in these alloys [61][62] [60].

Apart from modifying the texture, the addition of RE elements also positively impacts the corrosion properties of magnesium alloys. The RE elements form eutectic systems with limited solubility in Mg, leading to precipitation hardening. These RE-containing precipitates are thermally stable, meeting the demands of industries like automotive and aerospace for higher strength and creep-resistant magnesium alloys. The most common RE-containing alloys in this context are WE54 and WE43, based on the Mg-Y-Nd system [63].

To optimize the practical application of Mg alloys, controlling the texture during hot working processes, such as extrusion, rolling, or forging, becomes crucial. Weakening the basal texture through the addition of RE elements has shown promising results. By understanding and studying the deformation behavior of Mg alloys at high temperatures, it is possible to design appropriate deformation schemes that take advantage of the desired properties of these alloys.

2.7 Effect of Hot Working on Microstructure of Mg Alloy

For hot working, the flow stress (σ_f) during deformation is very important since it indicates the load needed for the operation. The flow stress is influenced by a number of deformation mechanisms that frequently compete with one another during hot deformation. During high temperature deformation, a generalized stress-strain curve is shown in Figure 2.8.

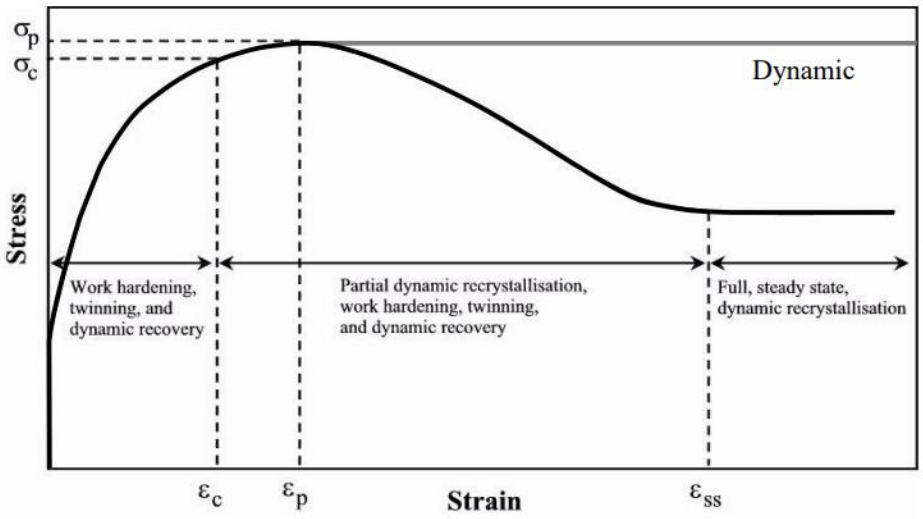

Figure 2.8: A Schematic Diagram of the Stress-Strain Curve during High Temperature Deformation [64]

Dynamic recovery, work hardening, and perhaps twinning are active during the early stages of deformation, but when the critical stress or strain is reached (ε_c or σ_c), dynamic recrystallization begins. As dislocations interact and grow in number, the flow stress rises during the early stages of deformation. But when the dislocation density rises, the driving force and thus the rate of recovery increased as well. During this time, low-angled boundaries microstructure and subgrains form. A steady-state flow stress is attained at a specific strain when the rates of recovery and work hardening establish a dynamic equilibrium that results in a constant quantity of dislocation [64].

In hot deformation, strain rate and temperature have an impact on the flow stress. The peak flow stress shifts to lower stresses and lower strains as temperature rises because of mechanisms including dynamic recrystallization and dynamic recovery that contribute more to flow softening. The reason for this is the thermal activation of softening mechanisms. With a decrease in strain rate, a similar pattern is found.

The basic processes of dynamic recovery, dynamic grain growth, work hardening, static grain growth, dynamic recrystallization, static recrystallization and static recovery are discussed here.

2.7.1 Work Hardening

Work hardening is the process through which a material becomes harder as it undergoes plastic deformation. Work hardening indicates that when the strain grows, it becomes challenging for dislocations to propagate as plastic flow is caused by a dislocation mechanism. The initial stages of deformation are characterized by the activation of dislocation sources and the movement of mobile dislocations along the planes of slip in the crystal lattice. As strain is increased, dislocations interact and multiply with one another, requiring larger stresses to drive the defects across the crystal lattice. Dislocation motion is also hindered by obstacles like grain boundaries and particles. Temperature, strain rate and stacking fault energy have significant impact on the work hardening behavior. It is found that, at ambient temperature, metals having low stacking fault energy showed three stage work hardening behavior, while metal having high stacking fault energy exhibit two stage work hardening curve at temperature higher than room temperature [65].

2.7.2 Dynamic Recovery

Dynamic recovery (DRV) is the term for the thermally driven annihilation and restructuring of dislocation defects during deformation. Similar to static recovery, dynamic recovery during high-temperature deformation causes more structured dislocation configurations inside the subgrain boundaries. DRV is a crucial mechanism in metals with large stacking-fault energies, including magnesium, aluminum, and the majority of bcc metals. In order to lower the lattice strain energy during DRV, dislocations are organized into cell wall by themselves through the formation of subgrains or small angle boundaries [64].

When the dislocation concentration and temperature are high enough, dynamic recovery occurs. Koike et al. have shown that recovery can take place when AZ31 alloys are deformed at ambient temperature, while these processes are normally seen when deformation occurs at higher temperatures [66]. The increase in dislocation density during deformation causes the accumulation of stored energy. The dislocations are organized into low-energy structures during recovery, which causes them to annihilate. Dislocations of the opposite sign annihilate one another when they come into contact, which can happen through a different types of mechanisms. The unresolved dislocations go on and seek out the lowest energy configurations, which can result in a development of sub grain boundaries and cell walls. These structures develop a microstructure that is more clearly defined and can enhance the mechanical qualities of the substance, like strength and ductility. A number of factors, including temperature, stress levels, and material qualities, influence the precise recovery mechanism that takes place [67].

2.7.3 Dynamic Recrystallization

The deformation texture and grain size of Mg alloys can be refined through the process of dynamic recrystallization (DRX). Dynamic recrystallization (DRX) can happen when recrystallization operations are rapid and recovery procedures are slow. DRX is more prominent in metals like copper and nickel that have low to medium stacking-fault energies. Primary grain size, texture, composition, temperature, strain rate and strain all affect DRX processes. Three different types of DRX are observed in Mg alloys, depending on the alloy's composition, the deformation temperature, and the strain rate. Twin dynamic recrystallization (TDRX), continuous dynamic recrystallization (CDRX), and discontinuous dynamic recrystallization (DDRX) are these. DDRX arises in metals like copper alloys that have comparatively low stacking fault energies (SFEs). High SFE

materials or extreme plastic deformation circumstances, such as equal channel angular pressing (ECAP), are conducive to CDRX.

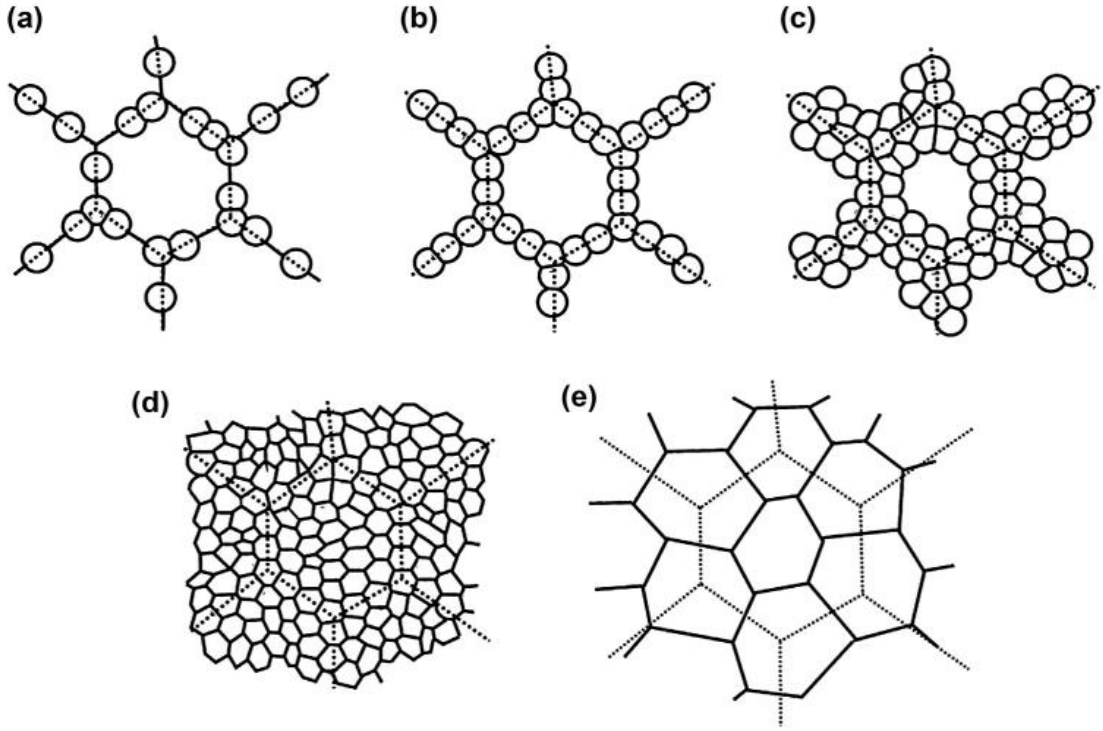

Figure 2.9: Microstructural Evolution during Dynamic Recrystallization [64]

Despite having a high SFE, magnesium is regarded as a low SFE metal because the dislocations those are on the basal planes have a low SFE. DDRX is a common phenomenon observed in Mg and its alloys when subjected to deformation at temperatures equal to or exceeding 250° C. This process involves two distinct stages: nucleation and growth. By means of the grain boundary bulging mechanism, which is schematically depicted in Figure 2.9, new grains form at the original grain boundaries. In materials with a polycrystalline structure, neighboring grains possess varying orientations, resulting in the accumulation of dislocations near the initial grain boundaries during the deformation process. Consequently, local strain gradients develop. Finally, the bulged area is divided from the parent-grain by the strain-induced sub-boundary, leading to the creation of dislocation-free grains, often referred to as "soft." When the softening effect surpasses the work hardening effect, a peak stress becomes evident in the flow curves. Figure 2.10 depicts instances of bulged grain boundaries, "necklace" microstructures, and the stress peaks associated with DDRX. It is important to note that the dimensions of the

recrystallized grains are influenced by the temperature of deformation and the rate at which

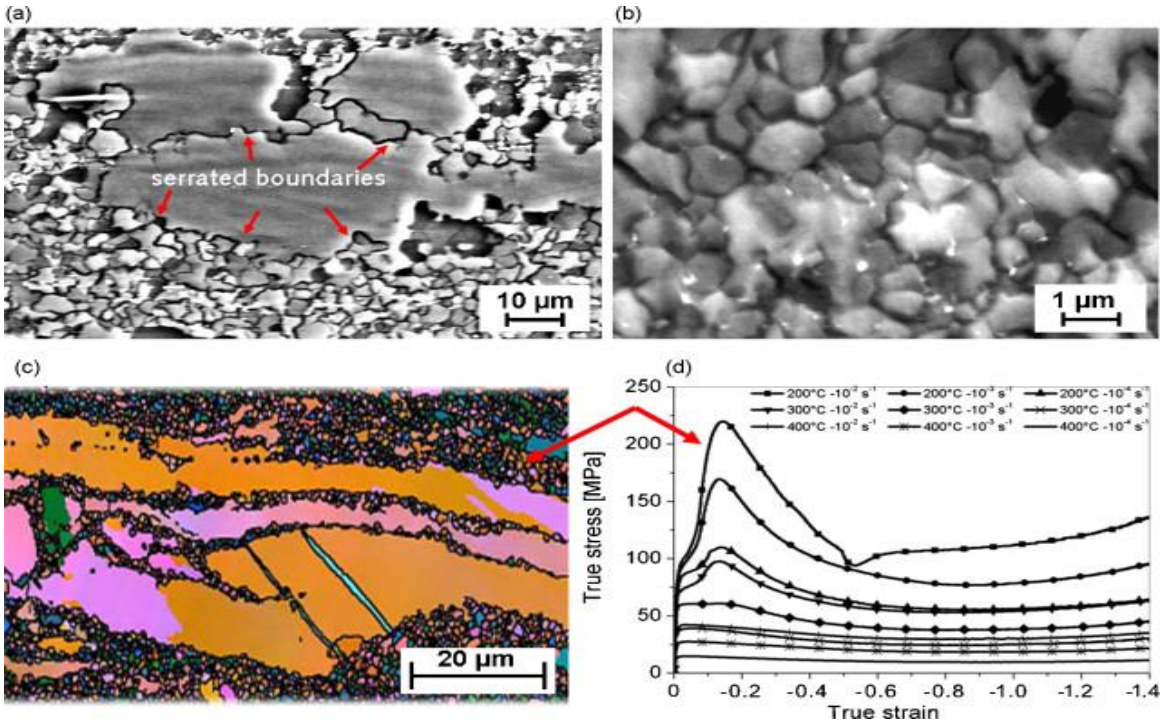

Figure 2.10: (a) – (c) Deformed microstructures of AZ31 compressed at temperature 200 °C, 10-2s-1 Strain rate: (a) Bulged primary grain boundaries; (b) Recrystallized grains; (c) "Necklace" microstructures of DDRX; (d) Stress-Strain flow curves [66]

strain is applied [66].

2.7.4 Effect of second phases on the DRX behavior of Mg alloys

Depending on the radius, spacing, and density of the second phase particles in an alloy, DRX can be promoted or suppressed. The presence of particles can promote DRX (dynamic recrystallization) by enhancing dislocation density through the mechanism of Orowan looping. However, in cases where the particles are extremely small and evenly distributed, the DRX process may be hindered due to the pinning effect, which reduces the mobility of dislocations.

Farzadfar et al. conducted a study on the dynamic recrystallization (DRX) characteristics of Mg-2.9Zn, Mg-5Zn-2Y, and Mg-6Zn-1.2Y alloys through hot compression tests. Their findings indicated that the presence of Mg_3YZn_6 and $Mg_3Y_2Zn_3$ particles significantly decreased the proportion of dynamically recrystallized grains in the two ternary alloys containing Y. Additionally, in Mg alloys, deformation zones frequently occur surrounding large particles that cannot undergo shear deformation [66].

2.7.5 Dynamic Grain Growth

Once recrystallization has concluded, strain-free grains have the potential to grow further at higher temperatures, a phenomenon known as grain growth. Temperature, specimen size, solutes, texture, particles, and time are a few of the variables that affect the rate and extent of grain growth. The shifting of grain boundaries is the primary process by which grains grow. The entire area of grain borders reduces as individual grains grow in size, which lowers the total energy. This reduction in energy serves as the driving force behind the process of grain growth. Grain growth is a phenomenon that can occur in all polycrystalline materials [68]. However, when grain growth takes place during superplastic deformation, it is specifically referred to as dynamic grain growth (DGG) [69].

2.7.6 Static Recovery

The characteristics of static recovery (SRV), which includes dislocation rearrangement, dislocation annihilation, and sub-grain development, are similar to those of dynamic recovery. SRV depends on the existence of dislocations and other defects that remain in the material after deformation since the driving force behind it is the strain energy stored inside the crystal lattice. In the context of hot-working, the extent of changes in microstructure resulting from SRV is typically minimal due to the prior occurrence of dynamic recovery. Following the deformation of austenite, it is typically observed that around 25% of the total softening can be attributed to static recovery (SRV), while the remaining portion is ascribed to static recrystallization (SRX) [70].

2.7.7 Static Recrystallization

Under appropriate conditions of thermal activation and stored energy, static recrystallization (SRX) can take place following deformation. Temperature, strain rate, degree of recovery, and degree of deformation all have an impact on the amount of stored energy. Composition, temperature, stored energy, texture, and other variables all affect how quickly crystals recrystallize. When temperatures are high, SRX happens quickly; when temperatures are low, recrystallization takes exponentially more time. It is worth noting that SRX can be suppressed by rapid cooling immediately after deformation, resulting in the retention of the deformed structure [70].

2.7.8 Static Grain Growth

Static grain growth, or SGG, is the term used to describe the process of grain growth that occurs during annealing [70]. Unlike dynamic grain growth, which occurs under the influence of both temperature and stress/load, SGG solely relies on temperature as the primary factor. Consequently, the extent of dynamic grain growth is consistently greater than that of static grain growth due to the additional contribution of stress/load.

2.7.9 Restoration

Deformation causes a material's crystal structure to develop more defects, like dislocations, which enhances the amount of stored energy in the crystal. Different restoration procedures take place to remove the defects in order to reduce this free energy. Recovery, grain growth, and recrystallization are three categories into which these mechanisms are divided. The restoration procedures significantly alter the material's deformation characteristics and lead to softening. These processes might take place statically during annealing or dynamically during deformation [67].

2.8 Techniques of Deformation Mechanism Evaluation

Any thermo-mechanical procedure may be controlled and designed much more effectively by being aware of the main deformation mechanisms that take place in the materials under consideration. To understand the deformation mechanisms, a wide range of thermo-mechanical parameters are used, including the activation energy (Q), strain rate sensitivity (m), strain exponent (n), and activation volume (V).

2.8.1 Activation Energy

Activation energy is the minimal amount of energy needed to move a grain boundary. It is a factor in figuring out how deformation occurs during grain growth. Strain rate and Temperature can affect the activation energy value. In pure Mg, the activation energies for lattice self-diffusion are 135 $kJmol^{-1}$ and 92 $kJmol^{-1}$, respectively, for grain boundary diffusion [71]. This indicates that lattice self-diffusion requires a relatively higher activation energy compared to grain boundary diffusion. However, it is important to consider that measuring activation energy to precisely determine superplastic deformation mechanisms is not considered a highly promising approach from a practical standpoint [72].

2.8.2 Strain Hardening Exponent

The strain hardening exponent (n), which depicts a material's ability to harden while deforming, describes how the metal acts during the forming process. It is determined by calculating the slope of the logarithmic true stress-strain curve. The value of n influences the dominant deformation mechanism exhibited by the material.

For n=1, the deformation mechanism is diffusional creep. When n=2, the dominant mechanism is grain boundary sliding. Glide-controlled creep occurs for n=3, while climb-controlled creep is observed for n=4-5. In cases where n>8, the deformation mechanism is associated with dispersion-strengthened alloys [72].

It is worth noting that the specific values of n and their corresponding deformation mechanisms mentioned here are general trends and can vary depending on the material and experimental conditions.

2.8.3 Static Rate Sensitivity Index

The strain rate sensitivity index (m) evaluates the degree to which the deformation behavior of a material varies as a function of the applied strain rate. In other words, it measures how much the strength and ductility of a material change when the rate of loading changes. Among the wide spectrum of thermo-mechanical properties, the ability of the strain rate sensitivity index (m) is regarded as a reliable unique constant that has already been thoroughly established to explain the dominant deformation process [73]–[75]. It has an inverse relationship with the (n) strain hardening exponent. The value of m has a strong correlation with the tensile ductility of metallic alloys. When m is small, the increasing stress at the neck will greatly speed up the increased strain rate there. As a result, the neck will develop quickly, resulting in an abrupt failure and a low elongation to failure. On the other hand, for large m, the strain rate slowly rises as a result of the elevated tension in the neck location. The progressive development of the neck as a result delays the onset of tensile failure and results in significant tensile elongations. Therefore, as the strain rate sensitivity increases, the tensile ductility enhances [76]. High m values have been found to be both a requirement and a frequent condition for metallic alloys to display superplastic behavior. The strain rate sensitivity index for superplastic materials should be larger than or equal to 0.3, and it typically falls between 0.4 and 0.8 for most superplastic materials [77]. The strain rate sensitivity, for Mg and its alloys, is mostly ascribed to their hexagonal close-packed structure [78]. For various values of m, various deformation mechanisms have

been identified, including the diffusional creep mechanism, grain boundary sliding, glide-controlled creep, climb-controlled creep, and dispersion-strengthened alloy for the value of m=1, m=0.5, m=0.33, m=0.14-0.25, and m<0.125, respectively [72].

Two common rate sensitivity parameters are determined using various techniques. They are total SRS index, m_t and instantaneous SRS index, m_i respectively. Comparing several work hardening curves produced under various but constant strain rates yields the "total" SRS index, m_t, which is associated to the course of the microstructure evolution [79]. The "instantaneous" SRS index, mi, is measured over a rapidly varying strain rate (jump test) under virtually constant strain and is considered to correspond to a constant structure. The strain rate jump test is widely acknowledged as the most accurate approach for calculating the strain rate sensitivity index. Two distinct specimens with various deformation histories are employed when the value of m is assessed using constant strain rate experiments. Therefore, it is expected that the results will differ if the deformation history is significant at the particular test temperature [77]. The strain rate sensitivity must therefore be precisely calculated in order to understand the deformation mechanism of superplastic materials. In the majority of finite element simulations and constitutive models of superplastic forming (SPF), the strain rate sensitivity index value is kept constant throughout deformation. The strain rate sensitivity, however, differs with strain, strain rate, and temperature, according to experimental research [80][77]. Therefore, using constitutive models without accounting for variations in the strain rate sensitivity index may produce inaccurate findings, particularly when substantial deformation is attained.

2.9 Applications of Mg Alloys

Mg has proven to be a promising metal for various industrial and biomedical applications due to its outstanding combination of mechanical, microstructural, and biological features [81], [82]. Mg has its limitations, however various production techniques, such alloying, casting, 3D printing, etc., can solve many of its inherent shortcomings, like its quick corrosion, which hinders the growth and expansion of Mg's industrial applications. Mg and its alloys, as engineering materials, have applications in the automotive, aerospace, electronics, sports, and biomedical industries, and it is anticipated that these sectors will grow given its amazing qualities and possibilities for recycling. Some uses of Mg alloys are presented below-

Military Application

The First and Second World Wars saw the first use of magnesium in the military when it was used to build military aircraft and their parts. Due to a number of significant environmental and financial benefits, including ductility, machinability, and castability in the manufacture of aircraft, that opened the door for magnesium to get into the civil aircraft industry. More crucial than the previously listed advantages, employing magnesium as a more lightweight metal than many other heavier alloys improve airplane fuel economy and lowers emissions. One instance of Mg being used in the aerospace sector is a typical Boeing 747 passenger model that replaced all of its Al alloys with Mg alloys. However, due to problems with durability, ignition, and flammability, Mg's potential for use is limited. Because of this, aeronautical structures still favor aluminum and its alloys over magnesium and its alloys. However, it is anticipated that with more efficient developments in applied magnesium research, which includes its manufacturing technologies and material development, it will be likely to manage such pervasive concerns with regard to the maintenance, repairs, and production of magnesium products [83].

Automotive Industries

Mg, Mg Metal Matrix Composites (MMC), and its alloys are used in the automotive and aerospace industries as addition to in the field of medical. Compared to earlier times, buyers of today base their car selection on two criteria: fuel efficiency and air pollution [84]. Alternative fuel sources, modification of aerodynamic aspect of vehicle, upgraded powertrains, and weight reduction, as suggested by Sameer and Suman, [85] can reduce fuel consumption and emissions of CO_2. Most straightforward of the aforementioned methods is said to be weight loss. The weight of a vehicle can be reduced by 20 to 70% by substituting Mg-based materials for its components.

Magnesium has a number of qualities for use in the automotive industry in addition to its low density, including great castability, strong ductility, and superior damping behavior than aluminum. The 1920s saw the introduction of Mg in a racing automobile, but it wasn't until 1970, when Volkswagen became the first company in the automotive sector to employ 20kg of Mg industrially in the body of one of its cars. Mg-based materials, such as Mg composites and alloys, are being used by more automobile firms nowadays in the interior as well as the exterior components of their products [5].

According to studies, a vehicle's weight reduction of 100 kg results in a 0.5 L reduction in fuel consumption for every 100 km traveled. This indicates that a 10% weight reduction leads to 8% reduction in fuel consumption for light trucks and an 6% reduction for passenger cars. Figure 2.11 demonstrates how an equivalent percentage increase in fuel consumption might result from a certain amount of weight reduction [86].

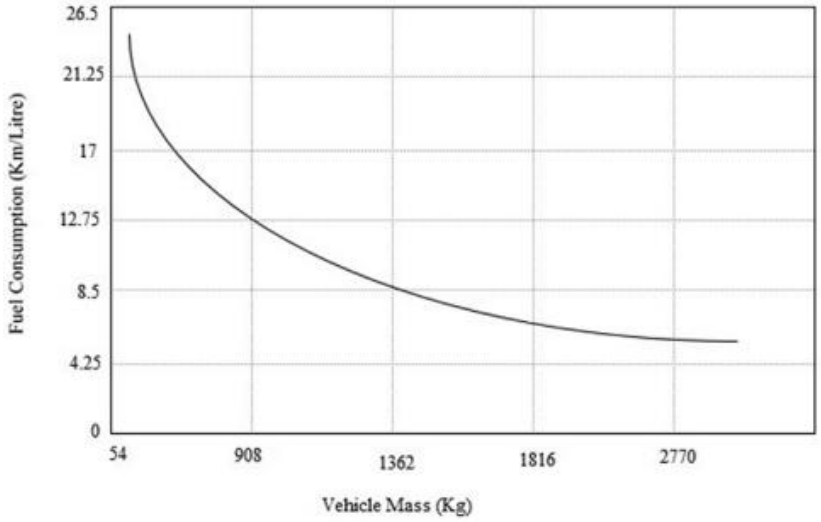

Figure 2.11: Weight of vehicle vs Fuel Consumption of the Vehicle Graph[86]

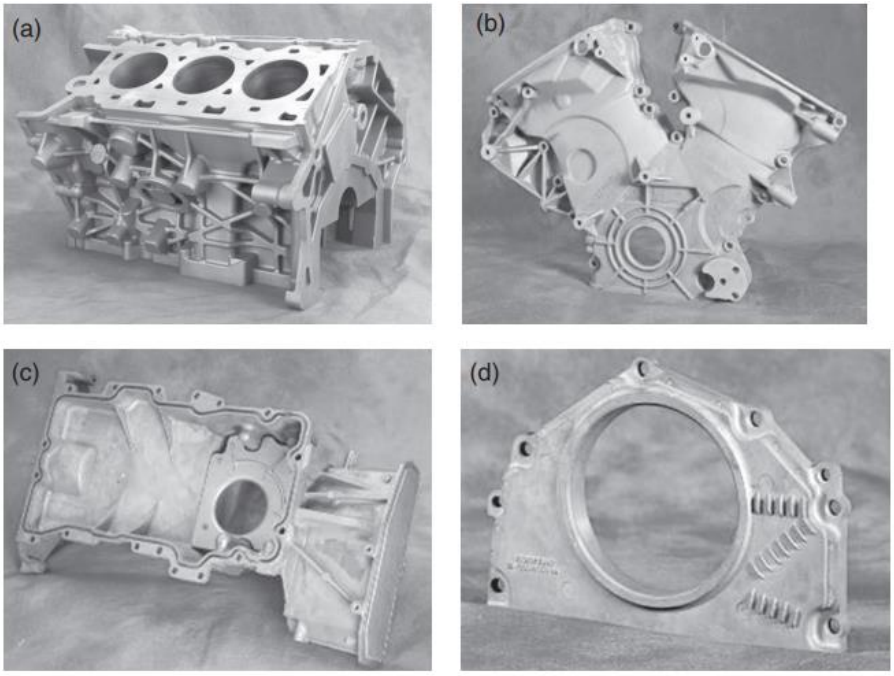

Figure 2.12: the USCAR Magnesium Powertrain Cast Components Project's magnesium powertrain components; (a) cylinder block, (b) front engine cover, (c) oil pan and (d) rear seal carrier [87]

Considering Mg's significance in energy efficiency, as well as its impact on the air pollution and environment, the use of Mg and its alloys in the automobile sector has increased generally during the past 20 years. The most efficient method of reducing air pollution is to reduce weight, which has a huge impact on transportation networks, industry, and, specifically, the CO_2 emissions released by automobiles. Although the expense of the Mg-produced parts on a vehicle is greater than the expense of the Al-made parts, this difference can be made up by Mg's contribution to lowering consumption of fuel and CO_2 emissions, which makes it worthwhile [86].

Aerospace Application

Weight reduction is one of the main goals in the aerospace sector. The aircraft's weight will be reduced overall, which will save expense on fuel. Over the years, a number of solutions for weight reduction have been developed, including less-density structural polymers, fiber metal laminates and aluminum. Low-density structural polymers do, however, have poor impact and damage tolerance characteristics. Weight reduction has also been difficult due to the slow advancement in the formation of aluminum alloys. Additionally, fiber metallic laminates are an expensive material as well. Again, at high temperature, they exhibit inferior qualities. Mg has become a desirable option due to all these restrictions. Due to the need for materials that are lightweight to lower the lift-off weight, Mg is widely used in spacecraft and missiles. It can also withstand extreme temperatures, being exposed to ozone, hitting by high-energy particles, and tiny impacts from meteorites. It also has great specific mechanical properties and is simple to construct. Various missiles utilized a significant number of Mg sheets [88].

Through the complete substitution of aluminum alloys with magnesium alloys, the aircraft has the potential to achieve a weight reduction of 60.4 tonnes, equivalent to 28% of its operational empty weight. However, the application of magnesium alloys has uncovered both inherent drawbacks and significant characteristics. These drawbacks primarily revolve around concerns related to flammability, surface toughness, and corrosion resistance. This led to restrictions being imposed by numerous organizations, and as a result, these laws significantly hampered magnesium's possibilities in modern aviation. Due to advancements in magnesium research, these persistent problems may now be handled with maintenance and repairs.

Figure 2.13 US Air Force's B-36 Long-range Bombers Assembly Line (Dark looking Mg sheet in the picture) [87]

Medical Application

Orthopedic implants must be structurally sound and biocompatible to function well and last a long time. In the biomedical and healthcare industries, metallic materials including titanium, chromium-cobalt, stainless steel, and their alloys have been widely used as biomaterials. The disadvantage of those materials, despite their higher mechanical and chemical stability, is that they don't match some of the properties like the elastic modules of genuine human bone in terms of characteristics. This causes the bone's stress shielding to weaken. Such limitation and issues are resolved by introducing Mg and related alloys as reliable biomaterials with biocompatibility [89]. The body produces a harmless oxide as a result of magnesium corrosion, which may be eliminated through urination. Additionally, as was previously mentioned, the presence of Mg in the human body's native bones promotes the formation of new bone. According to reports, the elastic modulus of human bone ranges from 3 to 20 GPa, whereas it is 41–45 GPa for magnesium, 110–117 GPa for titanium, and 189–205 GPa for steels that are corrosion-resistant. Research on the tissues of animals has shown that an implant made of Mg nourishes wounded tissue within 12 to 18 weeks and maintains its structural integrity before being replaced by natural tissue. Mg can aid in forming new bone and strengthening existing bone because of its functional activities and presence in bone tissue [90]. The first documented use of magnesium in medicine dates back to 1907, when Lambotte attempted to fix a bone fracture by combining pure magnesium with gold-plated steel nails. The idea, however, was a failure due to the magnesium corroding too quickly. Additional attempts attempted alloying magnesium with other substances, such as cadium, in a manner like the work done by Troitskii and Tsitrin

in 1944. Zna-menski created an alloy of magnesium and aluminum in 1945 and applied it to a human bone's wounds [91].

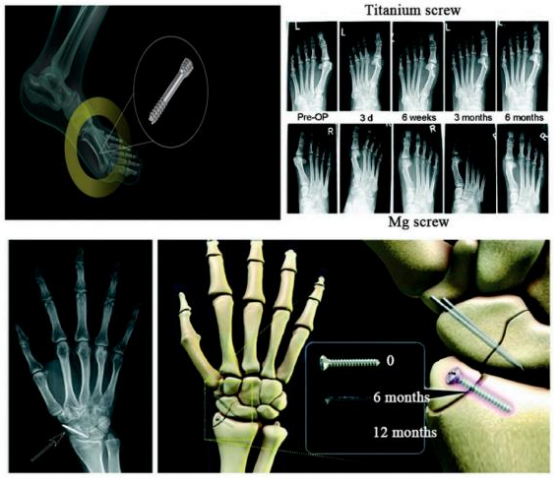

Figure 2.14 Some Examples of Application of Mg in Orthopedics [83]

Many researchers have concentrated on employing Mg in medical applications, such as biodegradable implants, through a variety of fabrication techniques. Research on processing Mg for biomedical uses has persisted. Diverse studies have attempted to propose or change processing techniques to reduce the rate of resorption of magnesium and its alloys and improve their properties, either for biomedical or industrial usage, where corrosion of magnesium is not desired [5].

Sports Application

Mg's impact resilience and light weight make it a popular material for sporting goods. Mg can also be molded into complex shapes, making it perfect for usage in tennis rackets, golf clubs, and archery bows handles. Additionally, because Mg can absorb shock and vibration, the alloys' dampening properties make it an ideal choice for the in-line skates chassis and bicycle frames. This absorption enables cyclists to ride more smoothly and comfortably while expending less energy. Mg vaulting poles are now also being produced because of their low tendency to twist and great resilience to torsional strain [88].

Electronic Application

The sector for electronic equipment is moving toward creating more portable and individual items. Consequently, it is crucial that the equipment's parts are both lightweight and strong. Mg-based materials satisfy the criteria since they are as light as plastic but far superior to it in terms of strength, heat transport, and the capacity to block interference of radio

frequency and electromagnetic when compared to their plastic counterparts. Mg alloys are used in hard-drive readers arm and heat sinks because they can be shaped into intricate designs and because they have strong heat dissipation and heat transfer properties [92].

2.10 Scope of the Work

The primary objective of this study is to gain a comprehensive understanding of the effects of gadolinium (Gd) addition in the ternary magnesium-zinc-yttrium (Mg-Zn-Y) alloy system. Specifically, our focus is on investigating how the inclusion of Gd impacts the microstructure of both cast and rolled alloys. In addition, it is intended to examine how different Gd addition percentages affect the tensile strength and elongation to failure at various strain rates and temperatures.

Additionally, this research will delve into studying the deformation mechanism under different temperature and strain rate conditions. This investigation aims to uncover the relationship between temperature and the changing trend of deformation mechanisms in the presence of Gd. By examining these aspects, we seek to enhance our understanding of the behavior of Mg-Zn-Y alloys when Gd is incorporated.

Chapter 3

Experimental Procedure

To accomplish the whole work, following experimental procedures were ensued:

a. Three Mg-1Zn-1.5Y-xGd alloy samples were cast into a 20 mm plate shape mold, where amount of Gd was varied by 1, 2 and 6 wt%. Subsequently, these plates were machined to a thickness of 18 mm to ensure a smooth and defect-free surface.
b. The chemical composition of these cast alloys was examined using X-ray fluorescence (XRF) to make sure the desired composition had been achieved.
c. These alloys were homogenized at 400° C for 21 hours, eliminating the chemical segregation that typically results from uneven cooling during casting.
d. To achieve a recrystallized microstructure, hot rolling was performed at a temperature of 420°C, resulting in an 83.33% reduction in thickness. After 30 passes, the 18 mm thick plates were reduced to a thickness of 3 mm.
e. To analyze the microstructural evolution of as-cast samples due to homogenization and hot rolling, optical-microscopy of all these treated alloys was carried out.
f. Scanning Electron Micrograph(SEM) and Energy Dispersive Spectroscopy(EDS) of hot rolled samples were carried out to find out the type and volume fraction of particle.
g. For further validation, X-ray Diffraction(XRD) analysis was also used.
h. Again, phase fractions and the quantity of precipitates were calculated thermodynamically using kinetic models. To validate the projected models CALPHAD analysis were employed.
i. On rolled sheet, high temperature tensile tests were performed at different temperature (250, 300, 350 and 400^{o} C) at different strain rate ($1x10^{-4}$ s^{-1} and $5x10^{-4}$ s^{-1}) to calculate the activation energy, the strain rate sensitivity and the strain hardening exponent value. Temperatures exceeding 400°C were avoided for Mg-alloys due to their increased susceptibility to oxidation during the tensile test, as any kind of inert gas was not used in the furnace, so maximum test temperature was selected 400^{o} C.
j. The activation energy, the strain rate sensitivity(m) and the strain hardening exponent(n) values were used to understand the deformation mechanisms at four test temperatures and two strain rates.

3.1 Raw Materials

Here, Gd was employed as an alloying element while the Mg-Zn-Y alloy served as the basis alloy. For this, magnesium and zinc were obtained from commercially available magnesium (99% Mg) and zinc (99.99% Zn) ingots, respectively. As a source for Y and Gd, 30% Gd Master alloy and 30% Y Master alloy were used.

3.2 Casting

An induction furnace was used for casting, and a ceramic crucible was used. Three alloys were cast varying Gd contents of 1, 2, and 6 weight percent, respectively. About 1.2 kg of raw materials were used for each casting. Before casting, the raw ingredients were carefully measured and gathered from their sources. Adjustments were made to the amounts of zinc, gadolinium, and yttrium so that the desired composition could be reached after casting.

For each casting, the weight % of the various metals is listed below in Table 3.1.

Table 3.1: Raw materials List for casting

Alloy	Zn	Y	Gd	Mg
Mg-1Zn-1.5Y-1Gd	1%	1.5%	1%	Balance
Mg-1Zn-1.5Y-2Gd	1%	1.5%	2%	Balance
Mg-1Zn-1.5Y-6Gd	1%	1.5%	6%	Balance

Following the correct amount of material being taken, it was heated at 150–200° C for one to two hours before being melted in the furnace. The melt was continuously covered with argon gas while it was in the furnace until it was put into the die, and it was agitated continuously to achieve a homogeneous mixture. Each casting was made using a metal die. The die's measurements were 270 mm by 120 mm by 18 mm. Before pouring the liquid metal into the die it was preheated to avoid uneven cooling of the liquid metal after casting.

3.3 X-Ray Flueoresence (XRF)

A non-destructive analytical method known as XRF (X-ray Fluorescence) determines the fundamental constituent of alloys and other materials. In XRF, high energy X-rays are directed at a sample, causing the atoms in the sample to emit secondary X-rays with a unique energy signature that can be measured and used to identify the elements present in the sample. The technique is widely used in a variety of industries, including the metals and alloys industries, to determine the elemental composition of alloys and ensure their

quality and consistency. XRF is also used in archaeological and geological studies, as well as in environmental and health and safety applications, among others.

Here, 10 mm x 10 mm samples were prepared and tested using a sequential X-ray fluorescence spectrometer (Lab Centre XRF-1800 model number). To determine compositions for all the alloys, XRF was employed.

3.4 Homogenization

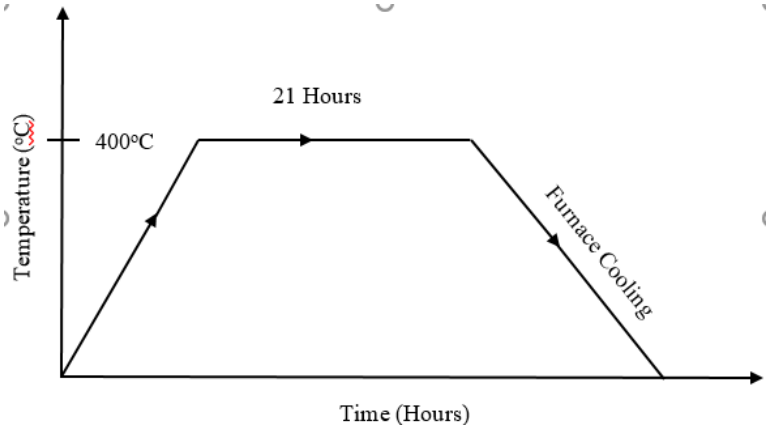

Figure 3.1 Temperature vs. Time Graph of Homogenization Process

All of the three casted alloy were homogenized for 21 hours keeping at 400^{o} C which was followed by furnace cooling that is shown in Figure 3.1. In this case, a furnace with a temperature controller, PROTHERM, model number PC442T, was employed. The purpose of this homogenization is to equalize the distribution of elements within the cast alloy, reducing segregation and creating a more uniform microstructure. Also it was assumed that the porosity and flaws inside would be minimized due to high temperature diffusion during the homogenization at this temperature.

3.5 Hot Rolling

Hot rolling is a metal working process in which metal is heated above its recrystallization temperature and then rolled by passing through roller machine to minimize the thickness or shaped into desired form. This process is done to achieve the desired microstructure, grain size, mechanical property and surface finish of the alloy and these are the function of rolling temperature and reduction percentage.

The rolling temperature for this experiment was 420° C, and a roller machine with a motor (Model No. 225M-6) was utilized. PROTHERM furnace was used for this heating purpose. Before each pass through the rollers, the sample was soaked at this temperature for 10

minutes. Subsequently, the heated sample was fed through the space between two rolling rollers. The thickness of the rolled sample was measured using digital slide calipers after each pass. The sample was then returned to the furnace for another 10-minute heating cycle before being taken out for further rolling. This procedure was repeated until the sample reached a thickness of 3 mm, which required 30 passes for each plate, with each pass 0.5 mm thickness was reduced. Through this process, the initial 18 mm thick sample was reduced to 3 mm, resulting in an 83.33% reduction in thickness.

3.6 Microstructural Observation

Light optical microscopes are used to observe microstructures. The purpose of this is to observe and analyze the microstructure of the alloy. Optical microscopy provides information about the size, shape, and distribution of the micro-constituents in the alloy such as grain size, grain boundaries, precipitates, inclusions, etc. This information helps to understand the properties of the alloy, predict its behavior in service conditions, and identify any defects that may impact its performance.

In order to observe the microstructure of as cast, homogenized, hot rolled for each sample, grinding and polishing was completed on each sample. This removes any oxides or foreign material from the surface of the sample and gives a clean surface for microstructure inspection. Samples were grinded using emery papers of 5 graded: 60, 220, 320, 500, 800, 1200 & 1500 CW respectively. After each grinding cycle was completed, samples were removed from the machine and washed in water. Then, wet polishing of these polished samples was conducted on velvet cloth by using paste of very fine alumina powder (0.01 μm). After etching the polished sample microstructures were observed under optical microscopy. For as-cast and homogenized samples, acetic glycol was used as etching agent while solution of 4 ml nitric acid with 96 ml ethanol was used for hot rolled sample. Etching time was varied by sample to sample. After successful etching samples were observed under optical microscope with magnification of 50x, 100x, 200x, 500x. Photographs were taken in each magnification for all alloys. Line intersection method was used to determine the grain size from the image and 40 grains were taken into consideration for the measurement.

3.7 SEM and EDX Analysis

SEM test was carried out only for rolled sample. 10 mm x 10 mm samples were prepared by polishing them properly and examined in their un-etched condition. This test was

conducted using a JEOL JSM-7600F field emission SEM machine. Both the secondary mode and the backscattering mode observations of microstructures were made. Here, to analyze distinct phases inside the matrix, scanning electron microscopy (SEM) was employed. Here are the steps followed to carry out SEM analysis of Mg alloys:

• **Sample Preparation**: 3 samples of dimensions (10mm x 10mm x 5mm) were cut from cast samples. Same steps for microstructure observation under optical microscopy were followed except the etching. Samples were dried keeping in oven at 60^{o} C for 15 minutes before conducting SEM test.

• **Sample Mounting**: The prepared sample was mounted onto a sample stub or holder using a conductive adhesive or carbon tape and ensured that the sample was securely attached to the stub to prevent movement during analysis.

• **Vacuum Chamber Preparation:** The sample stub was placed with the mounted sample into the SEM vacuum chamber. It was checked to ensure that the chamber was properly sealed and evacuated to achieve the desired vacuum conditions.

• **Instrument Setup:** According to the manufacturer's instructions, SEM instrument was calibrated and set up. the This involved adjusting parameters such as electron beam acceleration voltage, beam current, and working distance based on the sample characteristics and analysis requirements.

• **Sample Alignment:** The position and tilt of the sample stub was adjusted to ensure that the area of interest was properly aligned with the electron beam for imaging. The SEM's stage controls and visual feedback was employed to optimize the sample position.

• **Electron Beam Parameters:** Select the appropriate electron beam parameters for the analysis. These parameters include accelerating voltage, beam current, and spot size. Higher accelerating voltages provide better surface penetration, while lower voltages offer higher resolution for surface imaging.

• **Imaging Modes:** The desired imaging mode should be chosen based on the analysis objectives. Here, common modes include secondary electron imaging (SEI) for surface morphology, backscattered electron imaging (BEI) for compositional contrast, and energy-dispersive X-ray spectroscopy (EDS) for elemental analysis were employed.

• **Image Acquisition:** The SEM controls were used to acquire images of the Mg alloy sample. By adjusting imaging parameters, such as brightness, contrast, and magnification,

the image quality and detail was optimized. Multiple images were taken at different locations or magnifications as needed.

• **EDX:** For EDX, designated software for EDX was opened. The main difference is that an EDX detector was used, and the voltage should be between 15-20KV. The CCD camera was paused and needed to set the input CPS to 2K. Now it is ready to examine EDX. The sample must be refocused and chosen different points to analyze After saving the data the detector was shut downed and the EDX software.

• **Analysis and Interpretation:** To characterize the microstructure, grain morphology, phase distribution, and any surface features of the Mg alloys were analyzed from the acquired SEM images.

• **Reporting:** The SEM analysis results and observations were documented including relevant SEM images and EDS reports of the microstructures of all Mg alloys.

3.8 CALPHAD Analysis

The application of CALPHAD (Calculation of Phase Diagrams) modeling is extensively utilized in the investigation of magnesium (Mg) alloys, aiming to anticipate and construct equilibrium phase diagrams. These diagrams furnish crucial insights into stable phases, their compositions, and interrelationships across various temperature and composition conditions.

In the realm of Mg alloys, CALPHAD modeling integrates thermodynamic data, encompassing Gibbs energy functions and activity models, in conjunction with experimental data to precisely delineate phase equilibria. This data is amassed through diverse methodologies, encompassing calorimetry, thermodynamic measurements, and phase identification trials.

By employing optimization algorithms and minimizing the system's Gibbs free energy, CALPHAD modeling computes stable phases and their compositions within Mg alloys. This approach duly considers interactions between Mg and other alloying constituents, addressing aspects like solid solubility, phase transitions, and intermetallic compound formation.

The resultant equilibrium phase diagrams, as generated by CALPHAD modeling, empower researchers and engineers to explore phase stability within Mg alloys across distinct temperature and composition ranges. This insight proves invaluable for alloy design,

process enhancement, and the anticipation of microstructural changes during solidification, heat treatment, and various manufacturing procedures. Through CALPHAD modeling, our comprehension of Mg alloy systems is enriched, rendering significant insights into alloy behavior and facilitating the advancement of advanced Mg-based materials for diverse applications.

3.9 Tensile Test

Three hot-rolled alloys (Mg-1Zn-1.5Y-1Gd, Mg-1Zn-1.5Y-2Gd, and Mg-1Zn-1.5Y-6Gd alloy) were tested at two strain rates and four different temperatures. As a result, 24 samples of three different alloys needed to be tested in total. 250, 300, 350, and 400˚ C were the four distinct tensile test temperature. The two strain rate used were: $5x10^{-4}$ and $1x10^{-4}$ s^{-1}. A testometric materials testing machine with a maximum load capacity of 50 kN (Model No. M500-50CT) was used to conduct the tensile test.

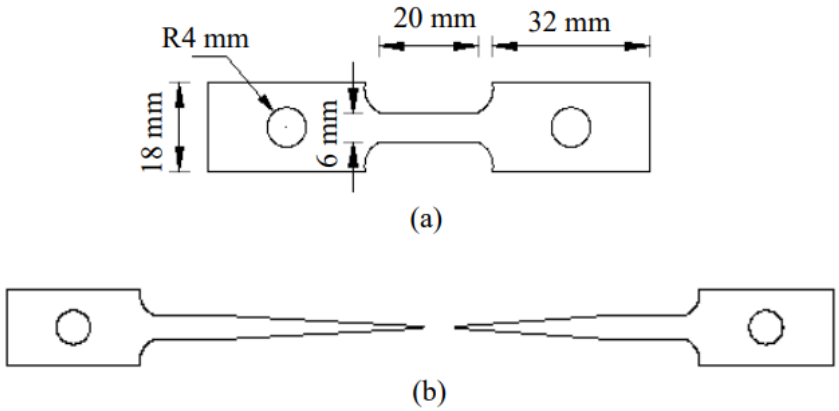

Figure 3.2 Schematic Tensile Test Sample- (a) before Tensile Test, (b) after Tensile Test

The tensile test samples were held between the holders at ambient temperature. Furnace was turned on after setting the specimen properly. Then sufficient time was given to it to reach experiment temperature and 20 minutes waited prior to start the test for even heating of the whole specimen. Samples were allowed to naturally cool after the test was finished, and raw data was gathered for later analysis and the formation of a stress-strain curve. The sample before the tensile test is displayed in Figure 3.2(a), and the sample after the tensile test is shown in Figure 3.2(b).

Chapter 4

Result and Discussion

4.1 Composition of the Alloys

In this whole experiment, intended composition of these alloys is Mg-1Zn-1.5Y-xGd (x = 1, 2, 6 wt%). After casting those three samples, to evaluate the composition if it had matched with the desired one, XRF was conducted. Results match closely as shown in Table 4.1.

Table 4.1: Compositions of Cast Alloys

Alloys	Alloy-A		Alloy-B		Alloy-C	
Elements	Given%	XRF test%	Given%	XRF test%	Given%	XRF test%
Mg	Balance	Balance	Balance	Balance	Balance	Balance
Zn	1	1.16	1	1.08	1	1.07
Y	1.5	1.34	1.5	1.36	1.5	1.56
Gd	1	1.18	2	2.12	6	6.21
Ca	0	0.08	0	0.05	0	0.05

Impurities might exist there since commercially pure Mg, Zn, Y, and Gd were used. As reported in Table 4.1, unanticipated element like Ca was found in these cast alloys, But very low in amount about less than 0.1%. Elements with a weight percentage of less than 0.1% are considered trace elements. The elements present in alloy having percentage less than 0.1% known as trace element. So these unexpected elements can be considered as trace element as well.

4.2 Optical Microstructure Observation

In this study, the microstructures of the three alloys were analyzed in three different conditions: as-cast, homogenized, and after rolling at 410^{o}C. The resulting optical micrographs, presented in Figure 4.1, Figure 4.2, and Figure 4.3, reveal distinct differences in the microstructural features of each alloy condition. These findings provide valuable insight into the effect of processing methods on the microstructure of metallic alloys.

4.2.1 Microstructure of As-Cast Samples

The optical micrographs presented in Figure 4.1 (a-c) depict the microstructural features of the three alloys in their as-cast condition. As shown in Figure 4.1, the microstructures of the as-cast samples are shown. For alloy-A no dendritic arm was visible, while dendritic structure composed of a dendritic α-Mg matrix and secondary phase crystals that form at the grain boundaries were found in alloy B and C. Notably, the increasing concentration of Gd in the Mg-1Zn-1.5Y alloy is observed to have a significant effect on the microstructure. Specifically, the dendritic arm becomes increasingly visible and finer as the concentration of Gd increases, resulting in a larger density of dendritic arms when the maximum concentration of 6 wt% is reached.

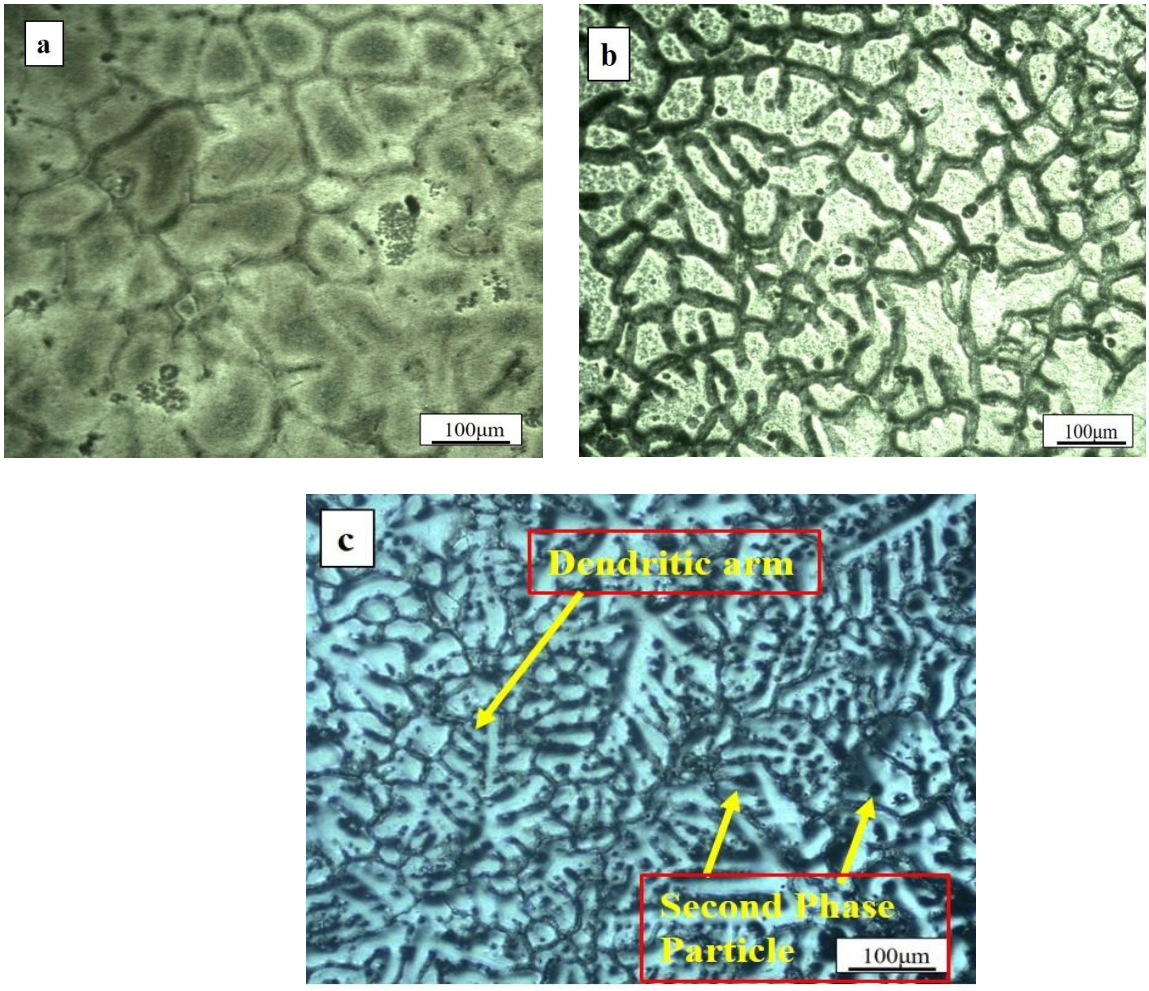

Figure 4.1 Optical microstructures of as-cast (a) Mg-1Zn-1.5Y-1Gd (b) Mg-1Zn-1.5Y-2Gd (c) Mg-1Zn-1.5Y-6Gd alloy

In a research study [93], it was discovered that secondary dendrite arm spacing (SDAS) present in the as-cast state significantly impacted the microstructural evolution during hot

extrusion and, consequently, influenced the mechanical properties of the extruded Mg-Zn-Y alloy. A correlation was found between a decrease in SDAS and the occurrence of dynamic recrystallization in the α-Mg phase region, as well as a higher dispersion of the fiber-shaped LPSO phase during the extrusion process. Increases in DRXed α-Mg grains having highly weak textures enhance ductility, while the fiber-shaped LPSO phase grains and effective dispersion of the hot-worked α-Mg grains with a robust basal texture combine to reinforce the alloy [93].

A significant change in grain size was also observed in the Mg alloy as the concentration of Gd gradually increased. The grain size measurements of the alloy with 1%, 2%, and 6% Gd were 135 ± 1.8 μm, 93.419 ± 1.2 μm, and 72.69 ± 0.9 μm, respectively. Line intercept method was used to measure the grain size by taking 40 grains for each alloy. This indicates that Gd possesses a notable grain refining ability in Mg alloys.

This observation is consistent with Fei Shi's previous study [94], which suggested that the addition of Gd enhances nucleation sites and thus contributes to the observed microstructural changes. Specifically, the increasing amount of dendritic arms and reduction of the grain size with higher concentrations of Gd in the Mg-1Zn-1.5Y alloy, as depicted in Figure 4.1 (a-c), provide obvious evidence for the critical role played by Gd in controlling the microstructure of metallic alloys.

4.2.2 Microstructure of Homogenized Samples

Figure 4.2 (a-c) depicts the optical images of the alloys, which underwent homogenization at 400^{o} C for 21 hours. The images reveal the disappearance of the dendritic arm and segregated solute in the matrix, which were apparent in the as-cast condition, and a significant increase in grain size. The dissolution or transition of secondary phases is the possible reason for this new segregation free uniform grain and that can be attributed to the enhancement of the solid solubility of Gd, Zn, and Y in the matrix during homogenization [95]. The homogenization process also facilitated the formation of new, finer precipitates, and the dissolution of non-uniformly distributed coarse precipitates by increasing the solid solubility of Gd, Zn, Y in the matrix during homogenization [95].

In a previous study [95], the evolution of phases present in the as-cast alloy was also observed during the homogenization process. Two phase transition were found, "Mg_5(Gd,Y,Zn) phase to 14H LPSO phase" and "18R LPSO phase to 14H LPSO phase," in case of Mg-1.2Zn-3.4Y-4.7Gd-0.5Zr alloy during homogenization.

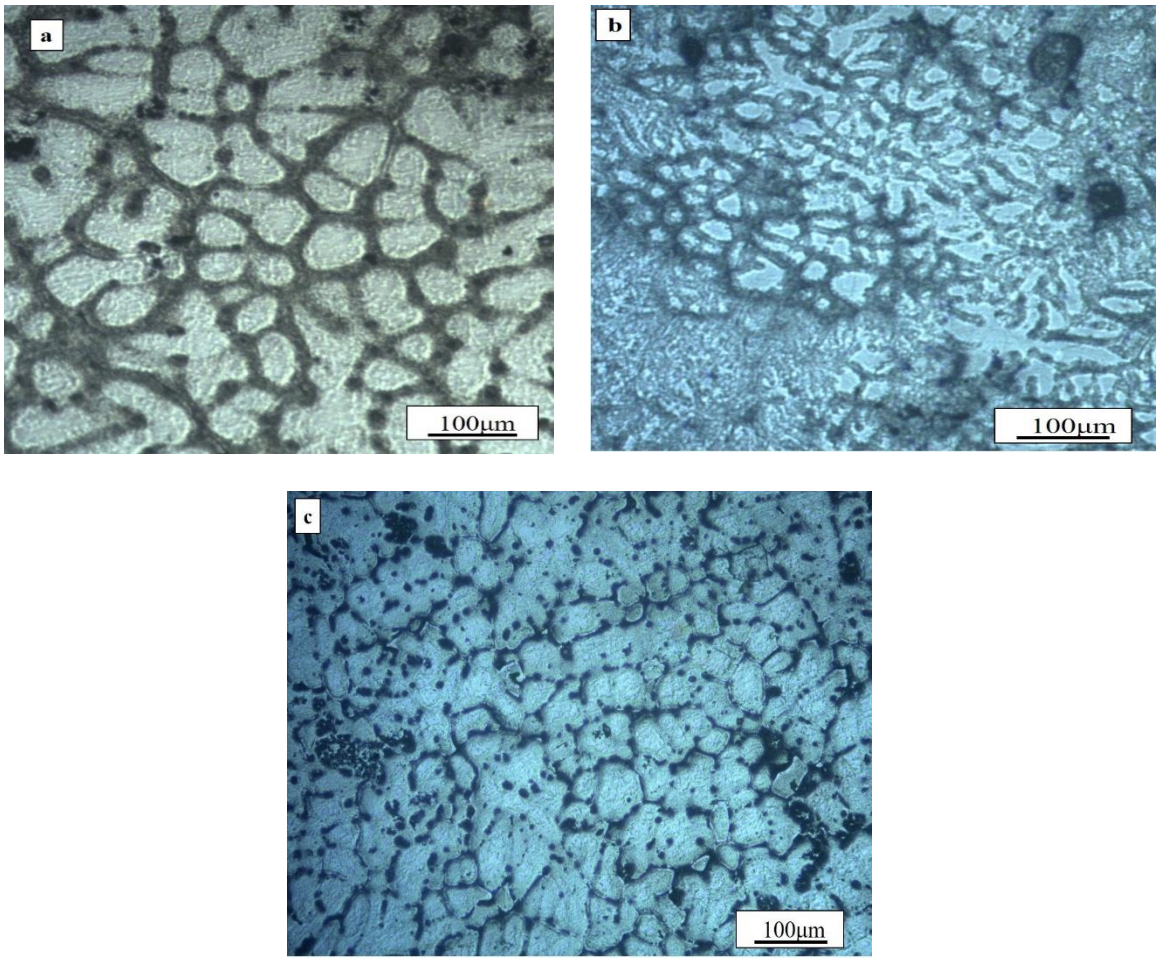

Figure 4.2: Optical microstructures of Homogenized (a) Mg-1Zn-1.5Y-1Gd (b) Mg-1Zn-1.5Y-2Gd (c) Mg-1Zn-1.5Y-6Gd alloy

4.2.3 Microstructure of Hot-rolled Samples

The microstructure of the three Mg-1Zn-1.5Y-xGd alloys (where x = 1, 2, and 6 wt%) in the hot-rolled condition was investigated using optical microscopy. As shown in Figure 4.3 (a-c), the measured grain size of the alloys decreased with increasing Gd concentration, with values of 21.39 µm, 15.47 µm, and 12.09 µm, respectively. This decreasing trend suggests that the addition of Gd promotes grain refinement in the alloys during hot rolling.

Furthermore, when compared to the as-cast condition, the hot-rolled condition resulted in a significant reduction in grain size. This suggests that the hot rolling process has a significant impact on the microstructure of the alloys, resulting in a finer grain size that may lead to improved mechanical properties, attributed to dynamic recrystallization(DRX). Previous investigations [96] have shown that dynamic recrystallization during hot rolling

is responsible for this grain refinement. This process involves the creation of new grains from the deformation of existing grains, resulting in a more uniform and refined microstructure.

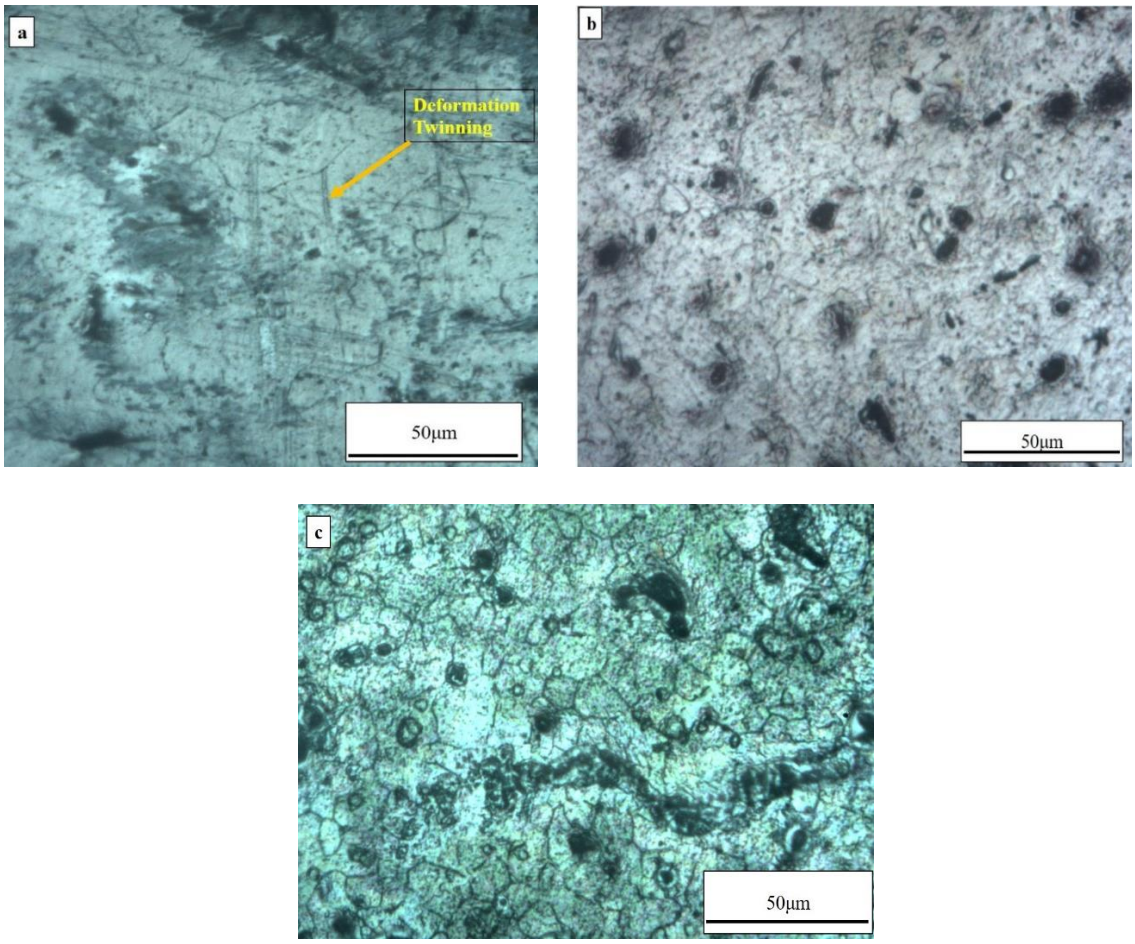

Figure 4.3: Optical microstructures of Hot Rolled at 420º C (a) Mg-1Zn-1.5Y-1Gd (b) Mg-1Zn-1.5Y-2Gd (c) Mg-1Zn-1.5Y-6Gd alloy

Again, numerous studies have reported the morphological evolution of phases due to hot working, which significantly influences the mechanical properties of the corresponding alloy. A study [95] with Mg-1.2Zn-3.4Y-4.7Gd-0.5Zr alloy found that the hot extrusion process induces the evolution of the 14H-LPSO phase, resulting in diverse morphologies due to severe deformation and dynamic recrystallization. This process leads to the fragmentation of homogenized alloy's 14H-LPSO phases, forming "sandwich-like" and "irregular-shaped" phases, while decreased solubility causes Zn, Y, and Gd to precipitate as "needle-like" LPSO phases.

4.2.4 Effect of Gd on Grain Size

Figure 4.4 compares the grain size of three Mg-1Zn-1.5Y-xGd alloys (with 1%, 2%, and 6% Gd) in three different conditions: as-cast, homogenized, and hot-rolled.

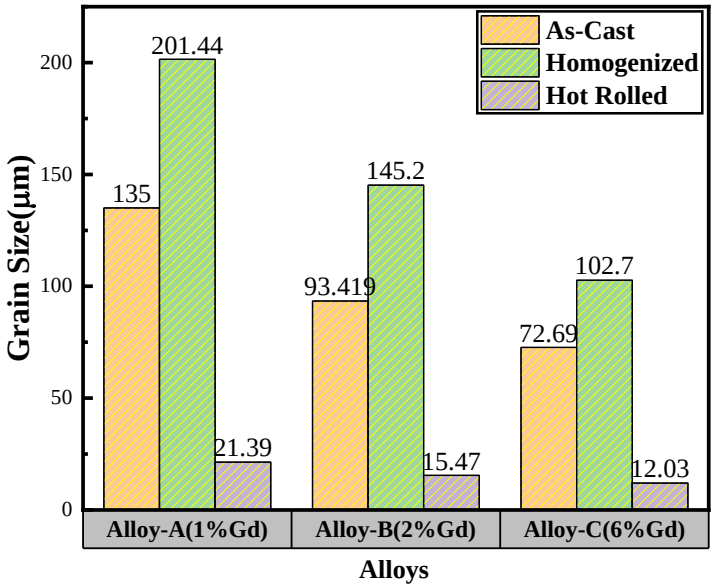

Figure 4.4: Grain Size Variation with Gd Content and in Different Conditions

The results show that the grain size decreases with increasing Gd concentration in all three conditions. In the as-cast condition, the grain size was 135 μm, 93.419 μm, and 72.69 μm for 1%, 2%, and 6% Gd, respectively. After homogenization at 400° C for 21 hours, the grain sizes increased to 201.44 ± 3.25 μm, 145.2 ± 2.78 μm, and 102.7 ± 2.34 μm, indicating an increase of 49.1%, 39.77%, and 24.86%, respectively, indicating that the homogenization process facilitated grain growth. The rapid solidification process during casting often results in coarse and non-uniform grains, leading to negative impacts on the alloy's mechanical properties and processing. The homogenization process involves heating the alloy to high temperatures, leading to the diffusion of atoms and the formation of new and more uniform grains with distinctive grain boundary, thus grain size increases. The process also breaks up dendritic structures, contributing to formation of large and uniform sized grain and a more uniform distribution of alloying elements which is also supported by a finding of a previous investigations [97][98].

Moreover, the most significant reduction in grain size occurred after hot-rolling, with values of 21.39 ± 1.33 μm, 15.47 ± 1.27 μm, and 12.03 ± 1.54 μm for 1, 2, and 6 wt% Gd, respectively that can be attributed to dynamic recrystallization (DRX) during hot rolling. This corresponds to a percentage grain size reduction of approximately 89.38%, 89.35%,

and 88.29%, respectively, compared to the homogenized condition. These findings suggest that the addition of Gd promotes grain refinement and that hot-rolling is an effective means of achieving further grain size reduction.

4.2.5 Size Distribution and Volume Fraction of Secondary Phase Particle

Particle size distribution was measured by using J Image software and analyzed for the alloys in Figure 4.5, Figure 4.6 and Figure 4.7, respectively. In each plot, particle size distribution was obtained by plotting the count versus the particle size. From these plots, the mean particle size and standard deviation were calculated for each alloy. The particle size of Mg-1Zn-1.5Y-1Gd alloy was found to be approximately 1.42 µm (with a standard deviation of 1.02), while for Mg-1Zn-1.5Y-2Gd and Mg-1Zn-1.5Y-6Gd alloys, it was found to be approximately 1.74 µm (with a standard deviation of 0.59) and 2.44 µm (with a standard deviation of 0.76), respectively.

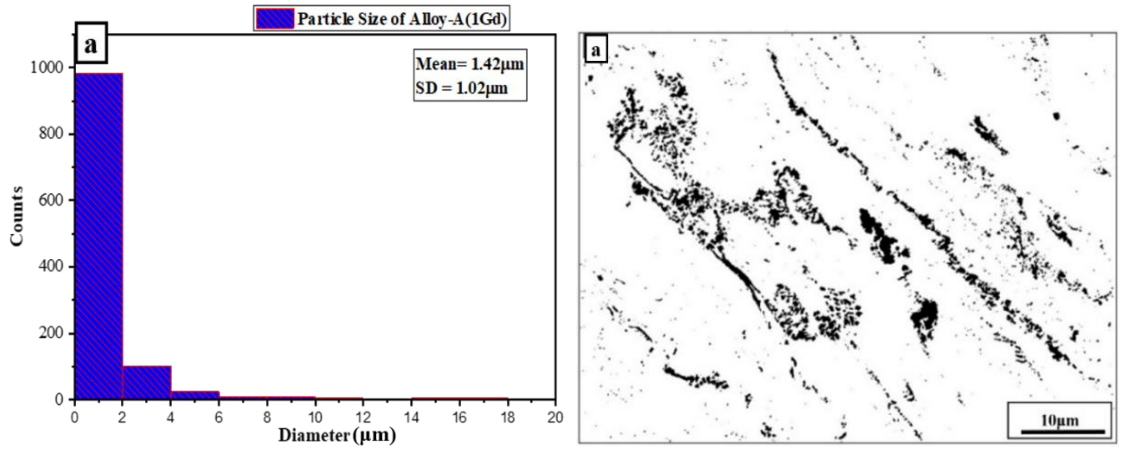

Figure 4.5: Mg-1Zn-1.5Y-1Gd Rolled Alloy (a) Particle Size Distribution, (b)SEM Image of only Particle

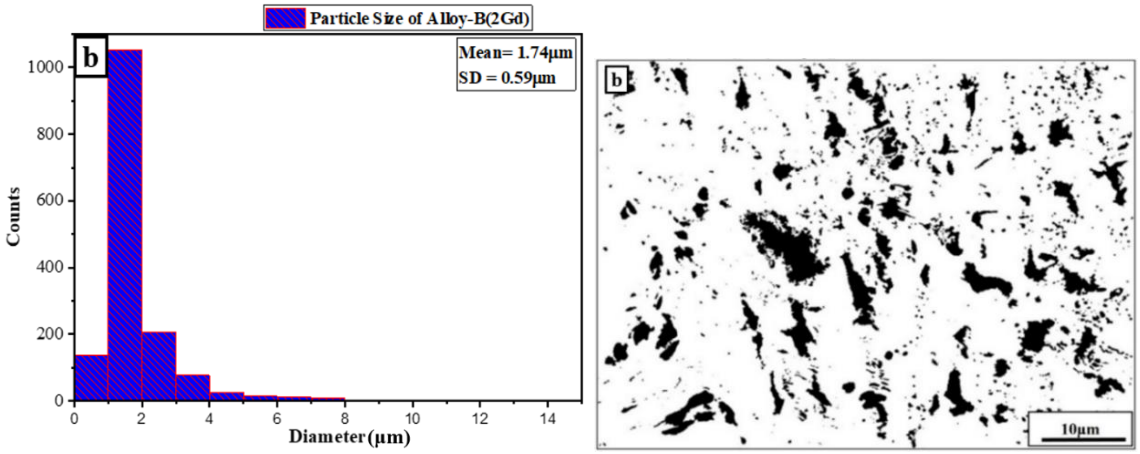

Figure 4.6: Mg-1Zn-1.5Y-2Gd Rolled Alloy (a) Particle Size Distribution, (b)SEM Image of only Particle

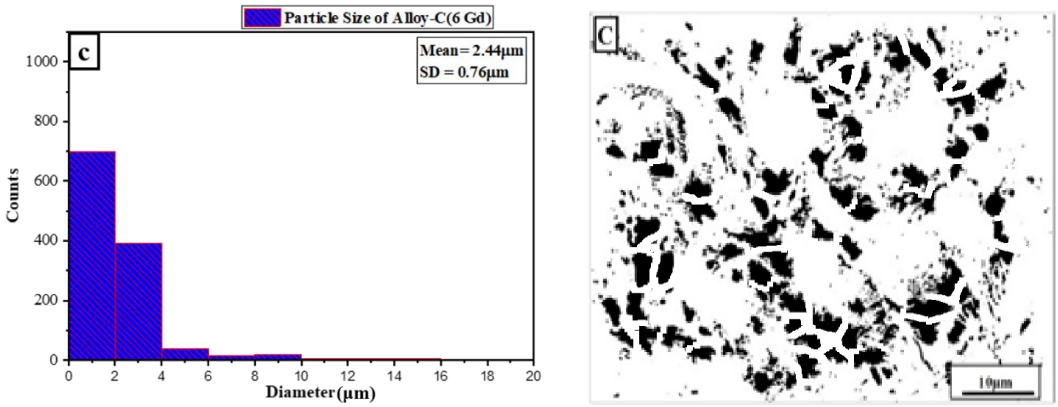

Figure 4.7: Mg-1Zn-1.5Y-6Gd Rolled Alloy (a) Particle Size Distribution, (b)SEM Image of only Particle

In Figure 4.8, the effect of Gd content on the particle size distribution is compared. The plot shows that as the percentage of Gd content in the alloy increased, the particle size also increased that can be attributed to the more formation of second phase particle. Therefore, the Mg-1Zn-1.5Y-1Gd alloy had the smallest particle size (with a standard deviation of 1.02) compared to the other two alloys.

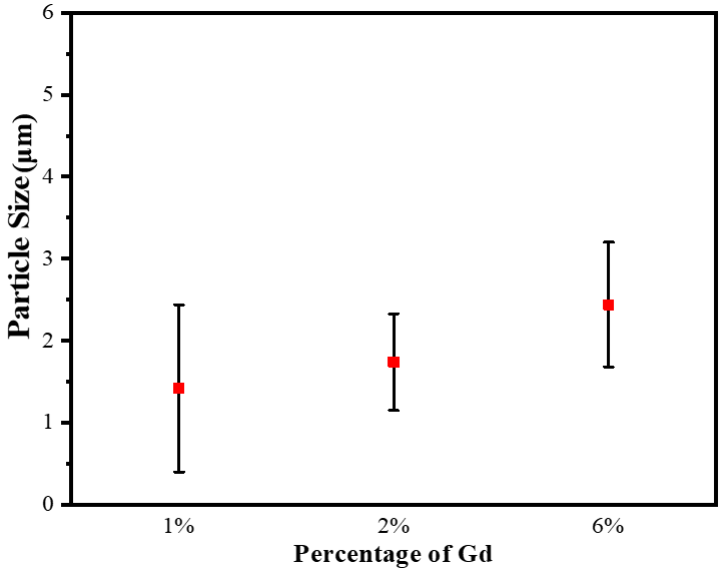

Figure 4.8: Particle Size Variation with Percentage of Gd Content

Table 4.2 Volume Fraction of Secondary Phases(%) in Alloy-A, B, and C

Alloy Composition	Volume Fraction of Secondary Phase (%)
Mg-1Zn-1.5Y-1Gd	3.25%
Mg-1Zn-1.5Y-2Gd	4.76%
Mg-1Zn-1.5Y-6Gd	7.54%

Again, volume fraction of secondary phase particle is determined by analyzing SEM image in imageJ software for alloy-A, B and C and found 3.25, 4.76, and 7.54%, respectively. So, it is a clear indication that increasing amount of Gd percentage results in more formation of secondary phase particle.

4.3 XRD Analysis

Figure 4.9(a)-(c) present the X-ray diffraction patterns of three alloys. The results reveal that the microstructures of the Mg-1Zn-1.5Y-xGd alloys, with x=1, 2, and 6 wt%, comprised of namely α-Mg, $Mg_{12}Zn(Gd,Y)$ (Z-phase/14H-LPSO), $Mg_3Zn_3(Gd,Y)_2$ (W-phase), and $Mg_5(Gd,Y)$, each exhibiting distinct diffraction peaks.

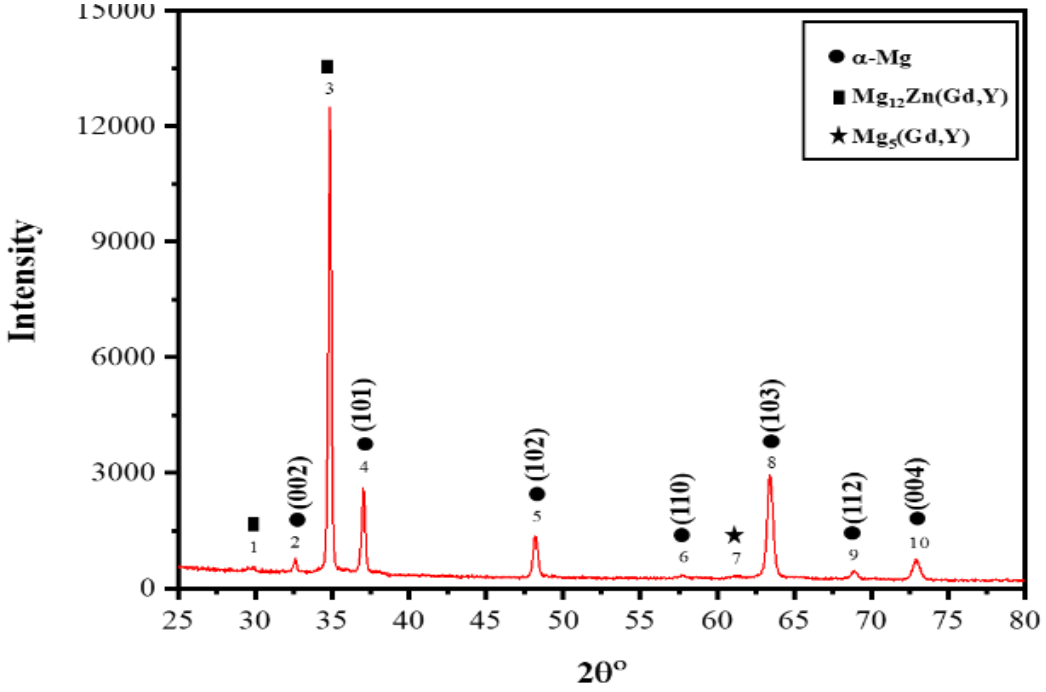
α-Mg
Mg12Zn(Gd,Y)
Mg5(Gd,Y)
Intensity
2θº
(002)
(101)
(102)
(110)
(103)
(112)
(004)

(a)

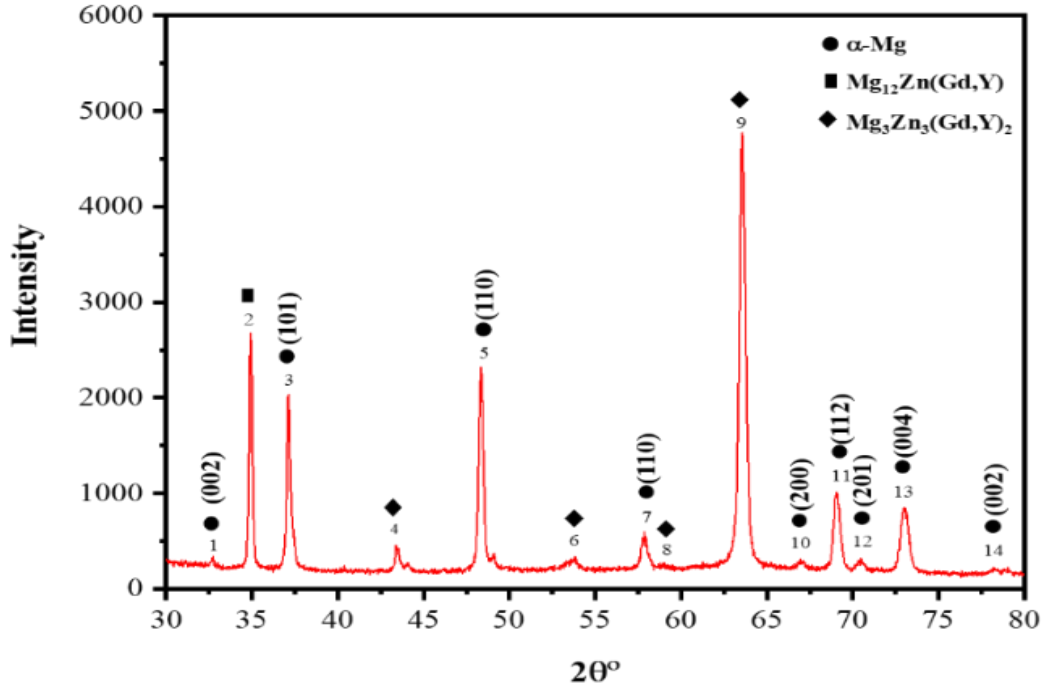
α-Mg
Mg12Zn(Gd,Y)
Mg3Zn3(Gd,Y)2
Intensity
2θº
(002)
(101)
(110)
(200)
(112)
(201)
(004)

(b)

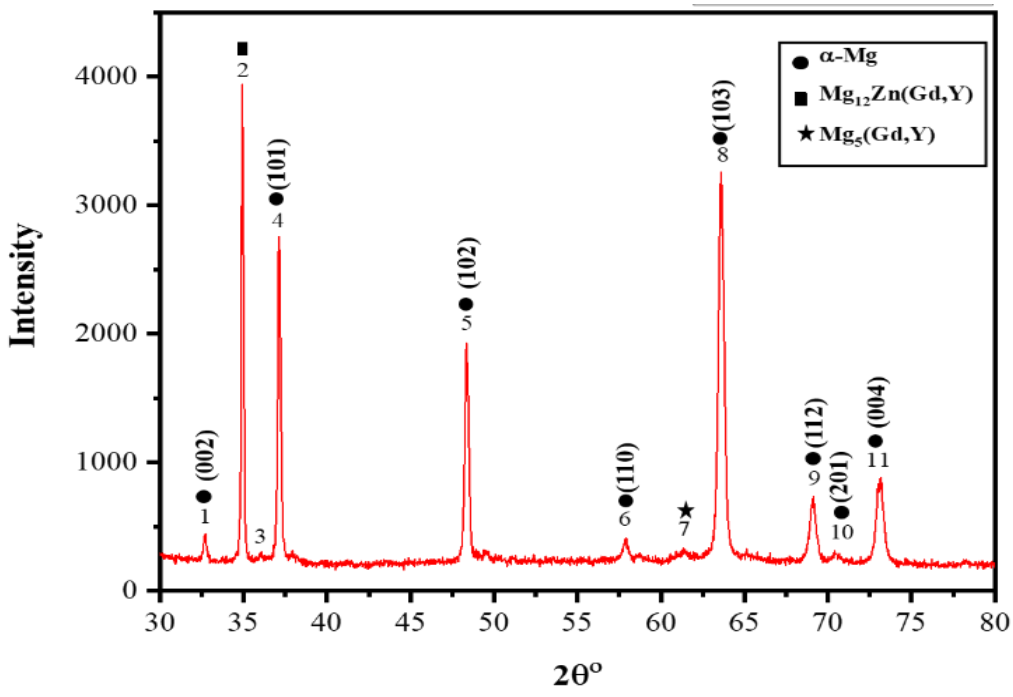

(c)

Figure 4.9: XRD Results of (a) Mg-1Zn-1.5Y-1Gd Alloy, (b) Mg-1Zn-1.5Y-2Gd Alloy, (c) Mg-1Zn-1.5Y-6Gd Alloy

According to previous studies [99], it is found that during solidification the precipitation of the secondary phase in the Mg-Zn-RE system alloys is largely controlled by the Zn to RE atomic ratio, which is clearly evident in case of this analysis. Among all identified phases α-Mg is found common in each alloy while the type of secondary precipitate phases varied with the change of Gd content, as with Gd the Zn-RE ratio changes.

From the Figure 4.9(b), it can be seen that as the amount of Gd was increased up to 2 wt% in the alloy-B (2% Gd), new phase $Mg_3Zn_3(Gd,Y)_2$ (W-phase) has appeared in expense of $Mg_5(Gd,Y)$ in the microstructure of the alloy. It is found in a study [94] that the newly emerged W-phase exhibits a pinning effect, which improves the mechanical properties of the Mg-alloy during the deformation processes. Further addition of Gd (up to 6 wt%) in the case of alloy-C causes the disappearance of the W-phase, leaving α-Mg, $Mg_{12}Zn(Gd,Y)$, and $Mg_5(Gd,Y)$ phases in the microstructure of the alloy that found in Figure 4.9(c). A previous study [100] with Mg-xZn-7Gd-5Y-0.5Zr (x=0, 3, 7, 13) composition is consistent with the findings of this XRD results.

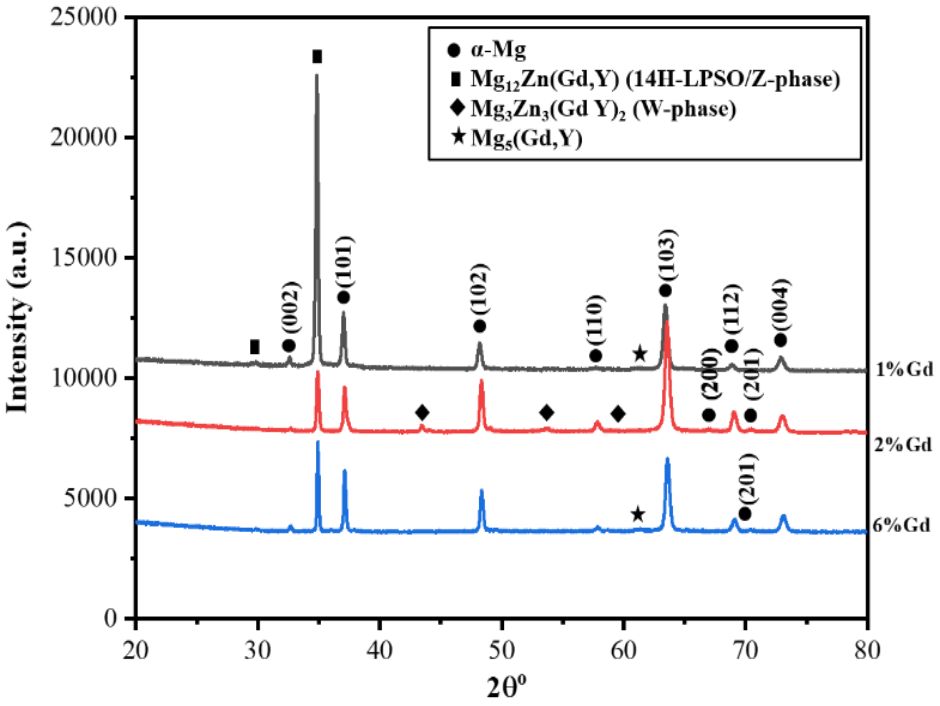

Figure 4.10: Comparative XRD Results of Mg-1Zn-1.5Y-xGd (x=1, 2, 6 wt%) Alloys

Figure 4.10 provides a comparative analysis of the XRD results for three alloys. The plot illustrates that the peak for the 14H-LPSO phase/Z-phase weakens with the addition of Gd, indicating a decrease of volume fraction in that phase with Gd addition.

Yamasaki et al. [93] found that the LPSO phase that is present in a Mg-Zn-Y alloy can refine the Mg grains via dynamic recrystallization, which results from strain-induced thermo-mechanical treatment and consequent deformation of the LPSO phase. The α-Mg grains that is recrystallized, exhibiting a weak texture, enhance the ductility and dispersion of the fiber-shaped LPSO phase, thereby strengthening the thermo-mechanically treated Mg-Zn-Y alloy.

4.4 CALPHAD Modelling with Temperature

The relationships between phase fraction and temperature for the three alloys in equilibrium are shown in the figures below. In the context of alloy-A, Figure 4-14 illustrates the presence of Mg_5(Gd,Y) and 14H-LPSO structures at room temperature, with dissolution occurring at approximately 200°C and 450°C, respectively. At elevated temperatures, the emergence of the W-phase, Mg_3(Gd,Y), is observed. The determined solidus temperature is 600°C, accompanied by a liquidus temperature of approximately 660°C.

In the case of alloy-B, Figure 4-15 depicts the coexistence of $Mg_3(Gd,Y)$ (W-phase) and 14H-LPSO structures at room temperature, undergoing dissolution at approximately 600°C and 400°C, respectively. The solidus temperature is determined to be 600°C, while the liquidus temperature is around 660°C.

Illustrated in Figure 4-16 for alloy-C, the absence of $Mg_5(Gd,Y)$ is noted at room temperature, while 14H-LPSO structures are present and dissolve at approximately 450°C. At elevated temperatures, the emergence of $Mg_3(Gd,Y)$ (W-phase) is observed. The solidus temperature for this alloy is determined to be 600°C, and the liquidus temperature is approximately 670°C.

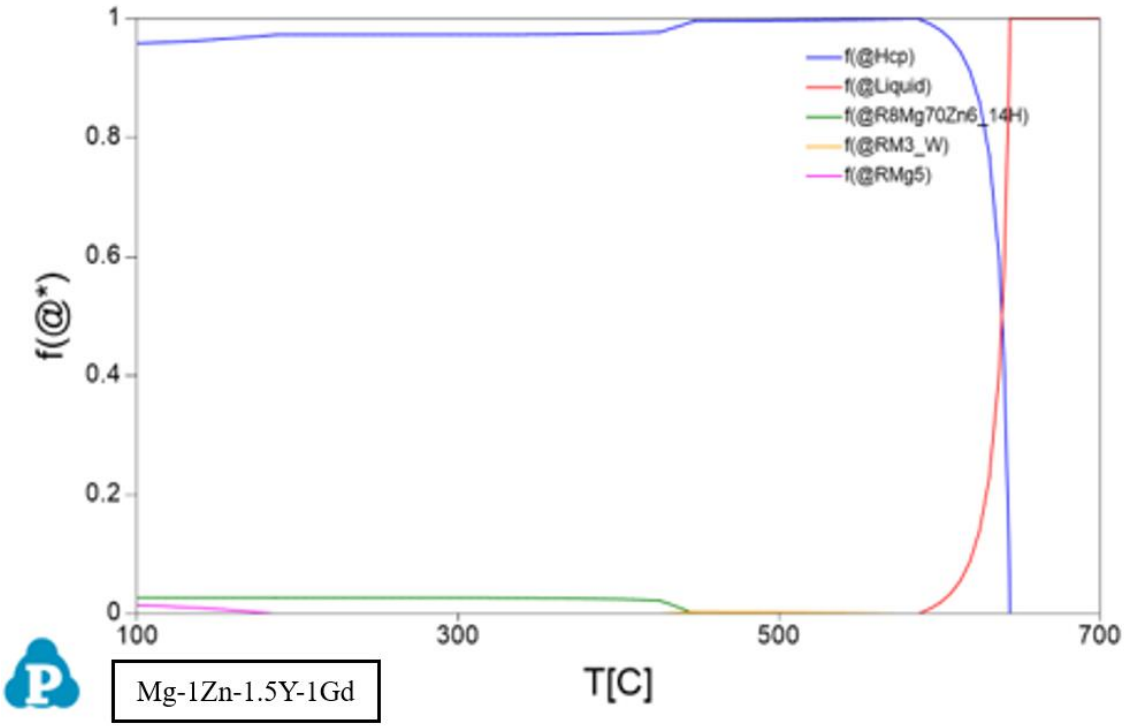

Figure 4.11 Equilibrium Phase Fraction vs Temperature in Alloy-A

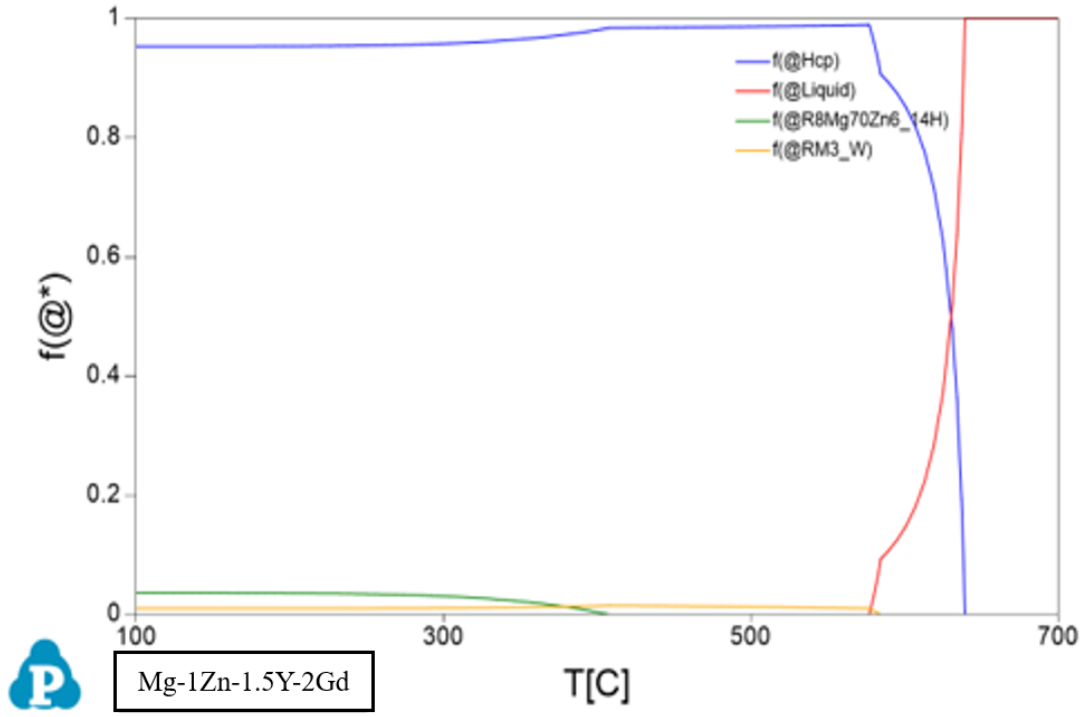

Figure 4.12 Equilibrium Phase Fraction vs Temperature in Alloy-B

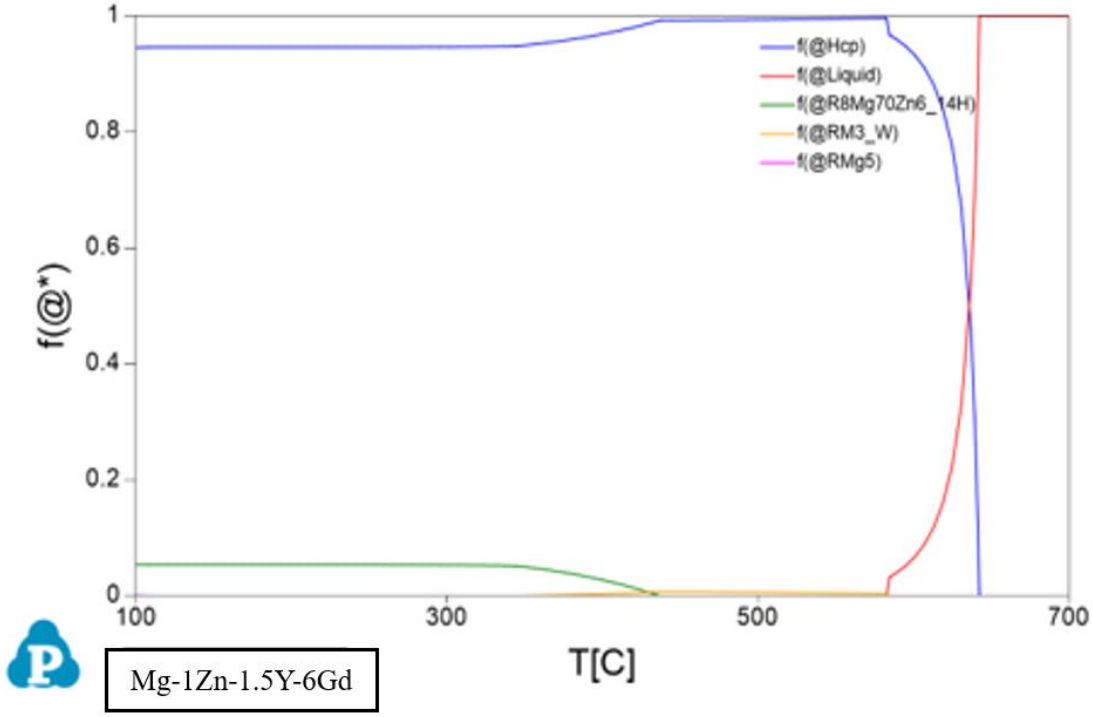

Figure 4.13 Equilibrium Phase Fraction vs Temperature in Alloy-C

Table 4.3 Variation of Volume Fraction and Secondary Phase Behavior with CALPHAD Analysis Temperature of Alloy-A

Secondary Phases in Alloy	Volume Fraction(%)					
	100-200^{o} C	200-300^{o} C	300-400^{o} C	400-500^{o} C	500-600^{o} C	600-700^{o} C
14H-LPSO	2.69%	2.69%	2.69%	_	_	_
$Mg_5(Gd,Y)$	1.35%	_	_	_	_	_
$Mg_3Zn_3(Gd,Y)_2$ (W-phase)	_	_	_	0.67%	0.67%	_

Table 4.4 Variation of Volume Fraction and Secondary Phase Behavior with CALPHAD Analysis Temperature of Alloy-B

Secondary Phases in Alloy	Volume Fraction(%)					
	100-200^{o} C	200-300^{o} C	300-400^{o} C	400-500^{o} C	500-600^{o} C	600-700^{o} C
14H-LPSO	4.23%	4.23%	3.87%	_	_	_
$Mg_5(Gd,Y)$	_	_	_	_	_	_
$Mg_3Zn_3(Gd,Y)_2$ (W-phase)	2.33%	2.33%	2.33%	2.33%	2.33%	_

Table 4.5 Variation of Volume Fraction and Secondary Phase Behavior with CALPHAD Analysis Temperature of Alloy-C

Secondary Phases in Alloy	Volume Fraction(%)					
	100-200^{o} C	200-300^{o} C	300-400^{o} C	400-500^{o} C	500-600^{o} C	600-700^{o} C
14H-LPSO	5.68%	5.68%	4.85%	_	_	_
$Mg_5(Gd,Y)$	_	_	_	_	_	_
$Mg_3Zn_3(Gd,Y)_2$ (W-phase)	_	_	_	0.92%	0.86%	_

Based on the CALPHAD analysis, it is evident that the evolution of secondary phases and their corresponding volume fractions significantly depend on both temperature and composition. Tables 4.3 to 4.5 illustrate the variations in volume fractions of different secondary phases as a function of temperature for alloys A, B, and C, respectively.

The analysis above suggests that the 14H-LPSO phase is present in all the investigated alloys, with its volume fraction increasing notably with Gd content, peaking at 6% Gd.

However, beyond 450°C, the 14H-LPSO phase dissolves within the matrix. In the case of alloy-B, the $Mg_3Zn_3(Gd,Y)_2$ (W-phase) demonstrates remarkable thermal stability, persisting from room temperature up to 600°C. In case of alloy-C, no $Mg_5(Gd,Y)$ was traced which showing slightly inconsistency with the XRD result. Presence of very small amount and low melting temperature of $Mg_5(Gd,Y)$ in alloy-C could be the reason for this discordance. In addition, it is also evident that alterations in composition have minimal impact on the solidus and liquidus temperatures.

4.5 SEM Observation with EDX

For further validation of the results of XRD analysis and the identification of different phases in the microstructure, SEM and EDS analyses were conducted on the hot-rolled samples of the three alloys. SEM imaging, Figure 4.14(a-c), provides high-resolution visualization and great depth of field of the microstructure, different phases and particles, while EDS analysis, Table 4.6 yields information on the chemical composition of different phases. The integration of these techniques can offer a more comprehensive understanding of the microstructure and the distribution of different phases in the alloys.

Figure 4.14(A) shows the SEM image of the Mg-1Zn-1.5Y-1Gd alloy, revealing the presence of $Mg_{12}Zn(Gd,Zn)$ (14H-LPSO) and $Mg_5(Gd,Y)$ secondary phases in the α-Mg matrix. In Figure 4.14(B), a new secondary phase, $Mg_3Zn_3(Gd,Y)_2$ (W-phase), is observed in the α-Mg matrix of the Mg-1Zn-1.5Y-2Gd alloy with the addition of Gd. This finding aligns with a previous study [101] that investigated Mg-Gd-Y-Mg alloy with three distinct compositions. The presence of the W-phase was only noted in one specific composition, characterized by a Gd:Y:Zn ratio of 2:1:1. This ratio closely resembles that of alloy-B in this study. This serves as a clear indication that the ratio of the present alloying elements strongly influences the formation of secondary phases within the alloy.

Figure 4.14(C) depicts the presence of two secondary phases, $Mg_{12}Zn(Gd,Zn)$ (14H-LPSO) and $Mg_5(Gd,Y)$, in the α-Mg matrix of the Mg-1Zn-1.5Y-6Gd alloy with further addition of Gd.

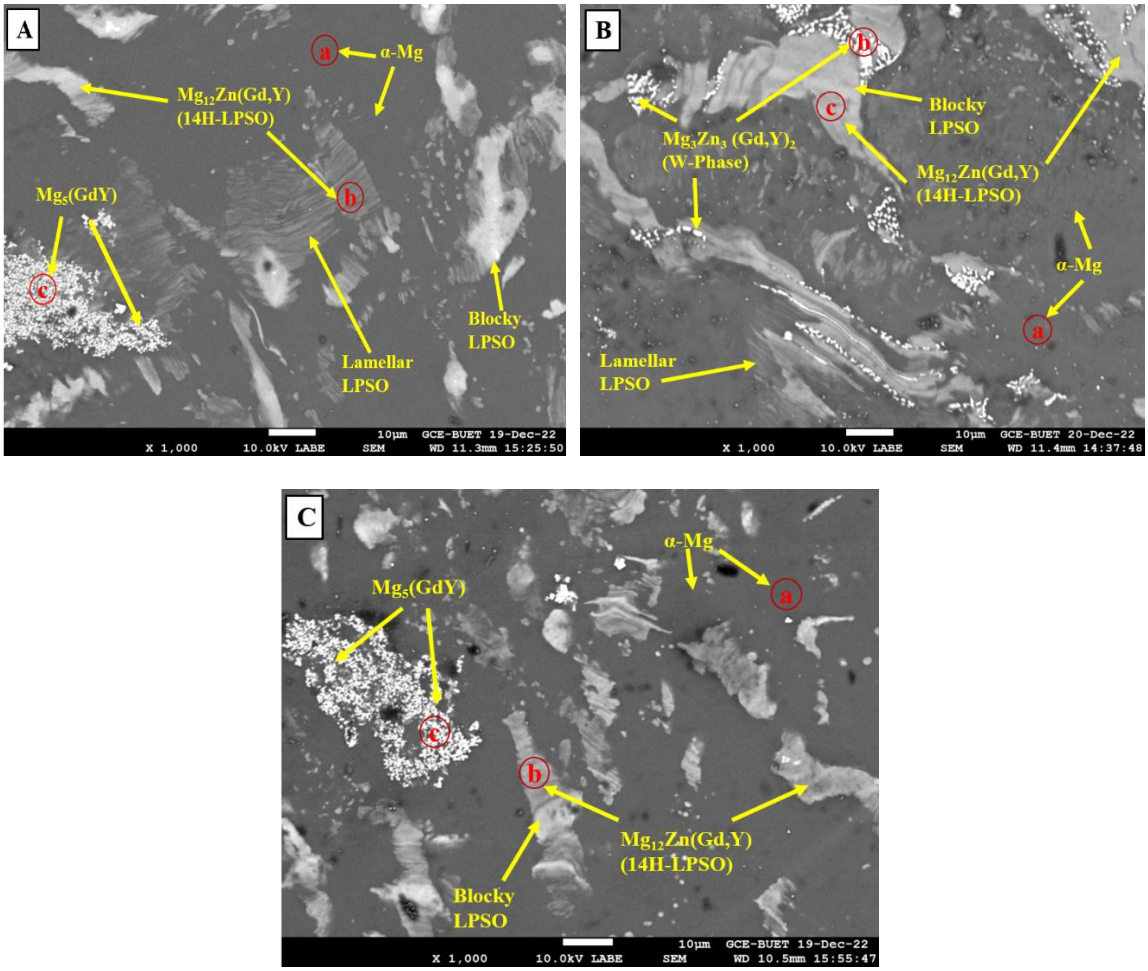

Figure 4.14: SEM image of Hot-Rolled Alloys: (A) Mg-1Zn-1.5Y-1Gd, (B) Mg-1Zn-1.5Y-2Gd, (C) Mg-1Zn-1.5Y-6Gd.

The 14H-LPSO phase is commonly found across all the alloys, displaying morphological variations due to changes in composition. Within the α-Mg matrix, two distinct types of 14H-LPSO phases are identified: lamellar and blocky. In alloys A and B, both lamellar and blocky phases are observed. Comparing alloy-B to alloy-A, the amount of lamellar LPSO decreases while blocky LPSO increases. In alloy-C, only the blocky LPSO phase is present, whereas the lamellar LPSO phase is nearly absent. Thus, an observed trend is the reduction of lamellar LPSO with higher Gd content, whereas blocky LPSO exhibits an increase. Notably, various studies indicate that the mechanical properties of these alloys are influenced by the morphology of the LPSO phase. In a study [38], blocky phases have been shown to possess greater strength compared to lamellar phases.

Table 4.6 presents the EDS results of different phases found in hot-rolled Mg-1Zn-1.5Y-xGd (x=1, 2, 6 wt%) alloys, along with the calculated Zn-RE atomic ratio and matched

with the reference ratio [10] to confirm the phases. The evaluated results are found consistent with the previous XRD results. EDX reports are given in Appendix A.

Table 4.6: EDS Results of Different Phases in Hot-Rolled Mg-1Zn-1.5Y-xGd (x=1, 2, 6 wt%) Alloys

Alloy Composition	Position	Mg (at%)	Zn (at%)	Y (at%)	Gd (at%)	Zn-RE Atomic Ratio	Phase
Mg-1Zn-1.5Y-1Gd	a	98.89	0.01	0.01	0.94	0.099	α-Mg
	b	85.58	4.67	1.43	8.32	0.45	$Mg_{12}Zn(Gd,Y)$ (Z-phase/14H-LPSO)
	c	80.49	0.50	13.98	5.08	0.026	$Mg_5(Gd,Y)$
Mg-1Zn-1.5Y-2Gd	a	99.07	0.01	0.14	0.79	0.01	α-Mg
	b	97.72	1.04	0.19	1.05	0.84	$Mg_3Zn_3(Gd,Y)_2$ (W-phase)
	c	97.72	0.67	0.60	1.45	0.33	$Mg_{12}Zn(Gd,Y)$ (Z-phase/14H-LPSO)
Mg-1Zn-1.5Y-6Gd	a	98.47	0.11	0.27	1.15	0.07	α-Mg
	b	86.56	4.39	1.58	7.47	0.49	$Mg_{12}Zn(Gd,Y)$ (Z-phase/14H-LPSO)
	c	75.34	0.28	17.77	6.62	0.01	$Mg_5(Gd,Y)$

4.6 Effect of Gd on Tensile Strength

4.6.1 Tensile Test at $5x10^{-4}$ s^{-1} Strain Rate

The tensile strength and elongation to failure of three different alloys, Mg-1Zn-1.5Y-1Gd, Mg-1Zn-1.5Y-2Gd, and Mg-1Zn-1.5Y-6Gd, were studied at 250^o C temperature and $5x10^{-4}$ s^{-1} strain rate, and the results are shown in Figure 4.15(a) and (b). The tensile strength values were found to be 189.009, 187.979, and 196.589 MPa for Mg-1Zn-1.5Y-1Gd, Mg-

1Zn-1.5Y-2Gd, and Mg-1Zn-1.5Y-6Gd, respectively. The elongation to failure values for the alloys were found to be 8.452%, 8.347%, and 11.286%, respectively.

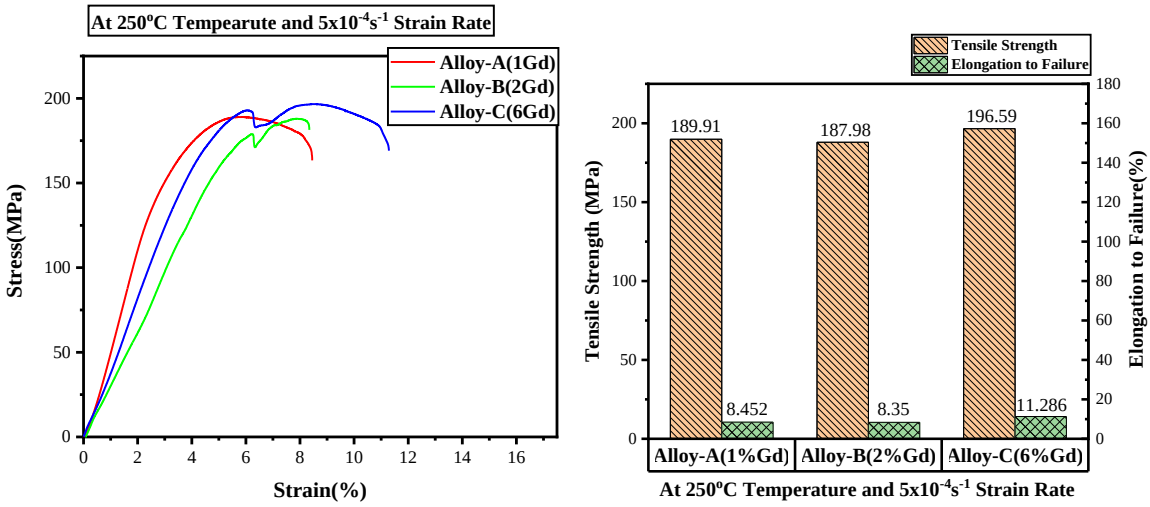

(a) (b)

Figure 4.15: Mg-1Zn-1.5Y-xGd (x=1, 2, 6%) alloy (a) Stress-Strain Curve, (b) Variation of Tensile Strength, Elongation to Failure, and Grain Size with Gd content at 250° C Temperature and $5x10^{-4}$ s^{-1} Strain Rate

The results indicate that, with the addition of Gd up to 2%, the tensile strength and the elongation to failure degraded very slightly compared to alloy-A (1% Gd) which again increased with further addition of Gd in alloy-C (6% Gd).

The Mg-1Zn-1.5Y-6Gd alloy has the highest tensile strength and elongation to failure values among the three alloys studied. This can be attributed to the finer grain size of 12.03 µm observed in this alloy, compared to 21.39 µm and 15.47 µm for Mg-1Zn-1.5Y-1Gd and Mg-1Zn-1.5Y-2Gd, respectively. The finer grain size allows for a higher number of grain boundaries and improves the strength and ductility of the alloy.

At 300°C temperature and $5x10^{-4}$ s^{-1} strain rate, the stress-strain curves for the three alloys are presented in Figure 4.16(a). The tensile strength of Alloy-A (1% Gd), Alloy-B (2% Gd), and Alloy-C (6% Gd) are 187.172, 177.979, and 159.989 MPa, respectively, as shown in Figure 4.16(b). The results indicate that the tensile strength decreases as the percentage of Gd content increases, with Alloy-C exhibiting the lowest tensile strength.

However, the trend is not consistent for elongation to failure, as Alloy-C exhibits the highest value (15.285%), followed by Alloy-B (11.46%) and Alloy-A (10.77%), as shown

in Figure 4.16(b). This trend suggests that the addition of Gd can improve the ductility of magnesium alloys at elevated temperatures with the expense of flow stress.

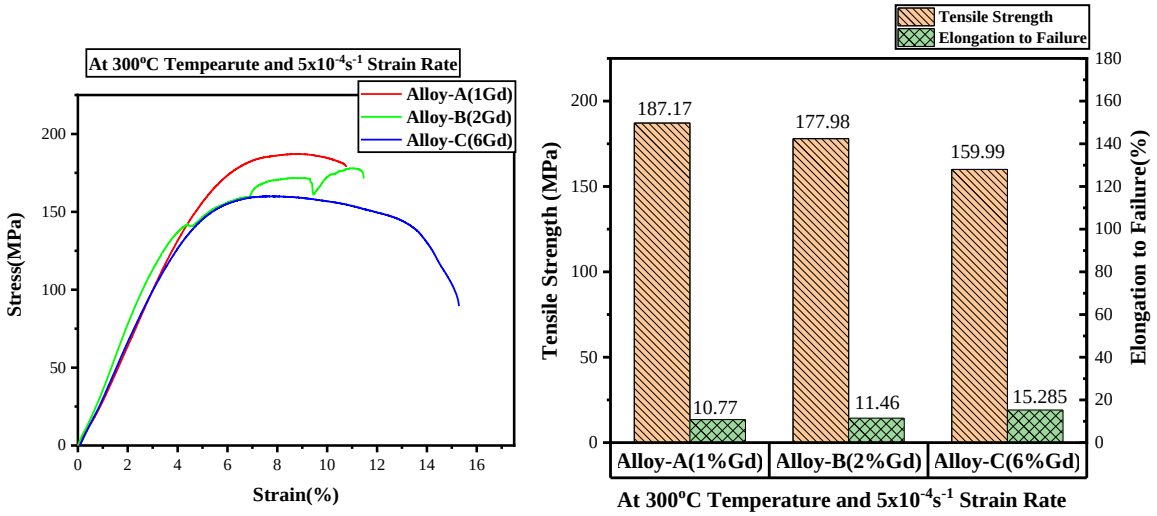

(a) (b)

Figure 4.16: Mg-1Zn-1.5Y-xGd(x=1, 2, 6%) alloy (a) Stress-Strain Curve, (b) Variation of Tensile Strength, Elongation to Failure, and Grain Size with Gd content at 300° C Temperature and $5x10^{-4}s^{-1}$ Strain Rate.

The tensile test data for three alloys (alloy-A with 1%Gd, alloy-B with 2%Gd, and alloy-C with 6% Gd) at 350° C and $5x10^{-4}$ s^{-1} strain rate were analyzed. Figure 4.17(a) shows the stress-strain curves for the three alloys, while Figure 4.17(b) presents the variations in the tensile strength, and the elongation to failure.

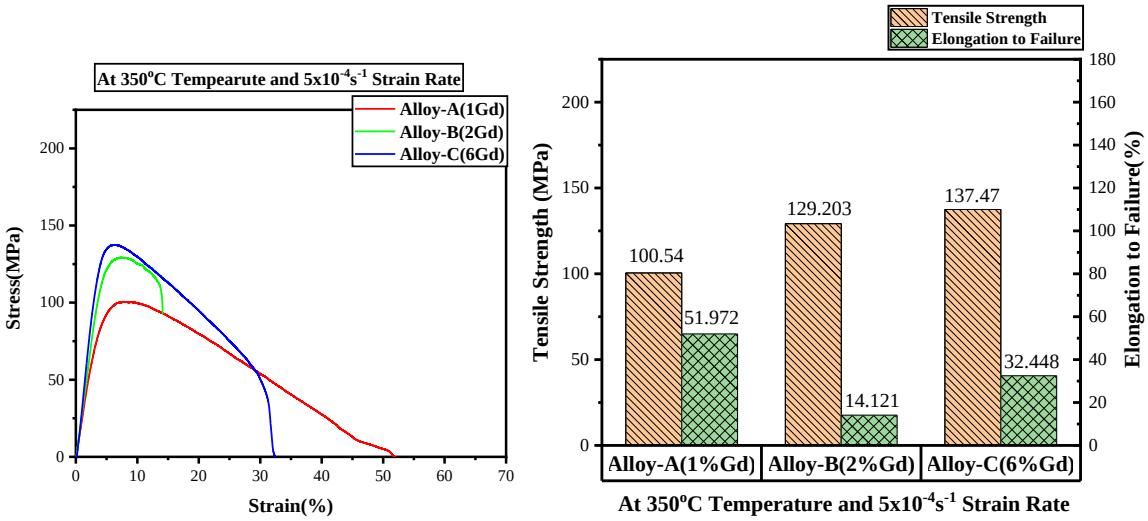

(a) (b)

Figure 4.17: Mg-1Zn-1.5Y-xGd (x=1, 2, 6%) alloys (a) Stress-Strain Curve, (b) Variation of Tensile Strength, Elongation to Failure, and Grain Size with Gd content at 350° C Temperature and $5x10^{-4}$ s^{-1} Strain Rate.

The tensile strength of the three alloys are 100.539, 129.203, and 137.468 MPa, respectively, which indicates to an increasing tendency of strength with addition of Gd. In contrast, the elongation does not follow such trend, the values of elongation to failure 51.972, 14.121 and 32.448%, respectively shows the elongation to capacity degraded with increasing amount of Gd.

Therefore, Alloy-C exhibited the highest tensile strength (137.468 MPa) compared to the other two alloys. On the other hand, alloy-A had the lowest tensile strength (100.539 MPa) but the highest elongation to failure (51.972%).

The tensile stress-strain curves of the three alloys at 400° C temperature and $5x10^{-4}$ s^{-1} strain rate are shown in Figure 4.18(a) and the tensile strength, and elongation to failure of the alloys are compared in Figure 4.18(b).

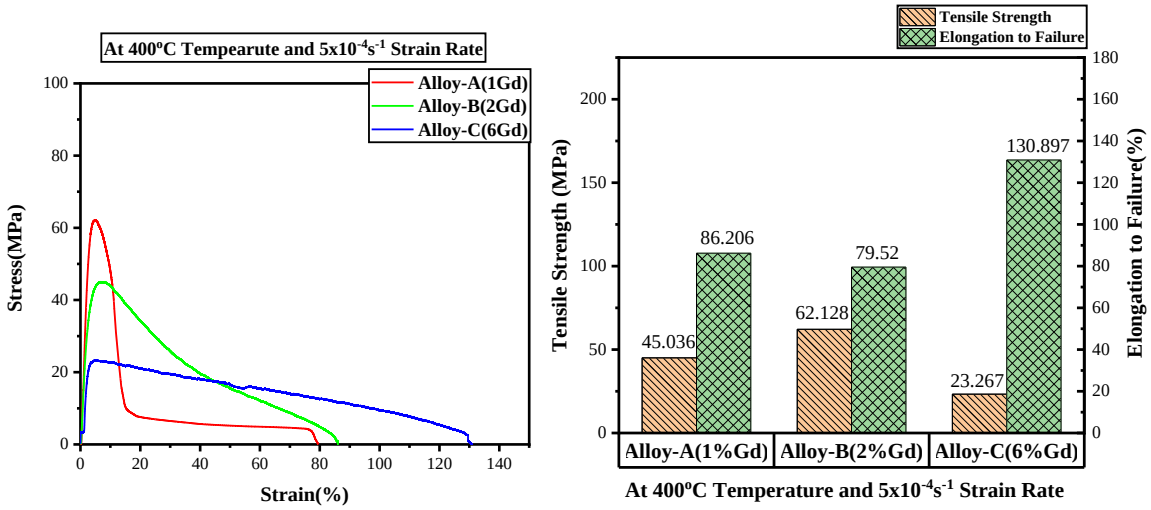

(a) (b)

Figure 4.18: Mg-1Zn-1.5Y-xGd (x=1, 2, 6%) alloys (a) Stress-Strain Curve, (b) Variation of Tensile Strength, Elongation to Failure, and Grain Size with Gd content at 400° C Temperature and $5x10^{-4}$ s^{-1} Strain Rate

At this elevated temperature (400° C), the tensile strength increased with addition of Gd (45.036 MPa for alloy-A and 62.128 MPa for alloy-B) initially and then decreased for further addition and found least for alloy-C (6%) 23.267 MPa. On the other hand, the elongation to failure of alloy-C is found highest, 130.89%, followed by 86.206% (alloy-A) and 79.52% (alloy-B).

However, upon analyzing the tensile strength values of alloy-A, alloy-B, and alloy-C at various temperatures and strain rates, it was observed that with increasing temperature, the tensile strength of each alloy degraded. Notably, the degradation percentage in alloy-B was lesser than in the other alloys. Consequently, at elevated temperatures and $5x10^{-4}$ s^{-1} strain rate, alloy-B exhibited a superior combination of tensile strength and elongation capacity compared to the other alloys.

4.6.2 Tensile Test at $1x10^{-4}$ s^{-1} Strain Rate

Figure 4.19(a) presents the stress-strain curves of three alloys for the tensile test conducted at 250° C temperature and $1x10^{-4}$ s^{-1} strain rate. Figure 4.19(b) compares the variations in tensile strength, and elongation to failure with changing Gd content.

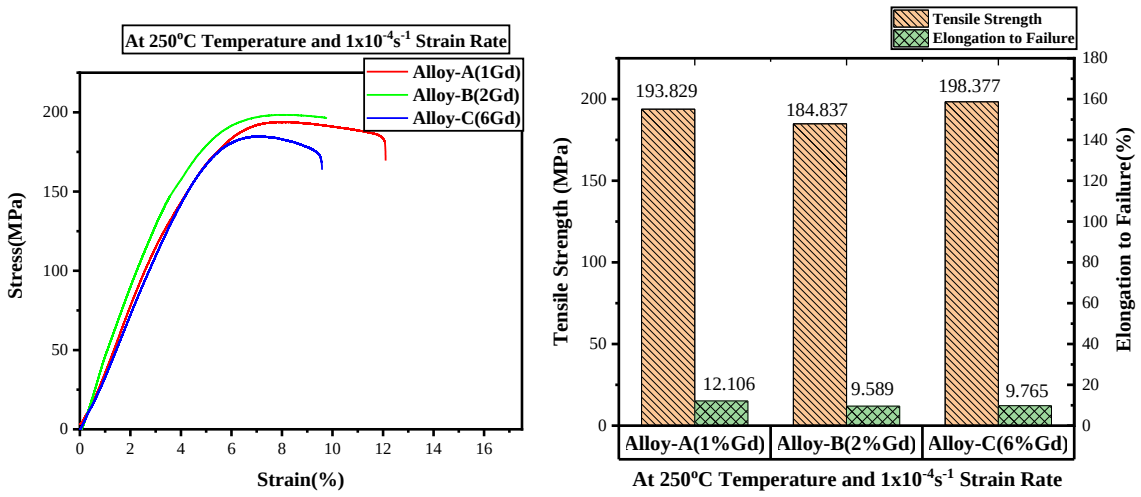

(a) (b)

Figure 4.19: Mg-1Zn-1.5Y-xGd (x=1, 2, 6%) alloys (a) Stress-Strain Curve, (b) Variation of Tensile Strength, Elongation to Failure, and Grain Size with Gd content at 250° C Temperature and $1x10^{-4}s^{-1}$ Strain Rate.

The measured tensile strength values for the three alloys are 193.829 MPa, 184.837 MPa, and 198.377 MPa, and the corresponding values of elongation to failure are 12.106%, 9.589%, and 9.795%, respectively. Thus, it is evident that at this temperature and strain rate, alloy-C with 6% Gd exhibited the highest tensile strength of 198.377 MPa among the three alloys, as shown in Figure 4.19(b). However, alloy-C also had the lowest elongation to failure of 9.765%, while alloy-A with 1% Gd exhibited the highest value of 12.106%.

Tensile tests were conducted on three alloys at a temperature of 300°C and a strain rate of $1x10^{-4}$ s^{-1}, and the results are shown in Figure 4.20. Figure 4.20(a) displays the tensile stress-strain curves of the three alloys, while Figure 4.20(b) illustrates the effect of changes in Gd content on the tensile strength, and the elongation to failure.

The tensile strength values of the three alloys were 176.395, 132.108, and 184.837 MPa, and the elongation values at failure were 16.301, 26.853, and 9.586%, respectively. Upon analyzing the comparison, it was observed that the tensile strength initially decreased and then increased with increasing amounts of Gd, while the elongation to failure displayed the opposite trend.

Similar to the results at 250° C, at this temperature as well, alloy-C exhibited the highest tensile strength and the lowest elongation to failure among the three alloys.

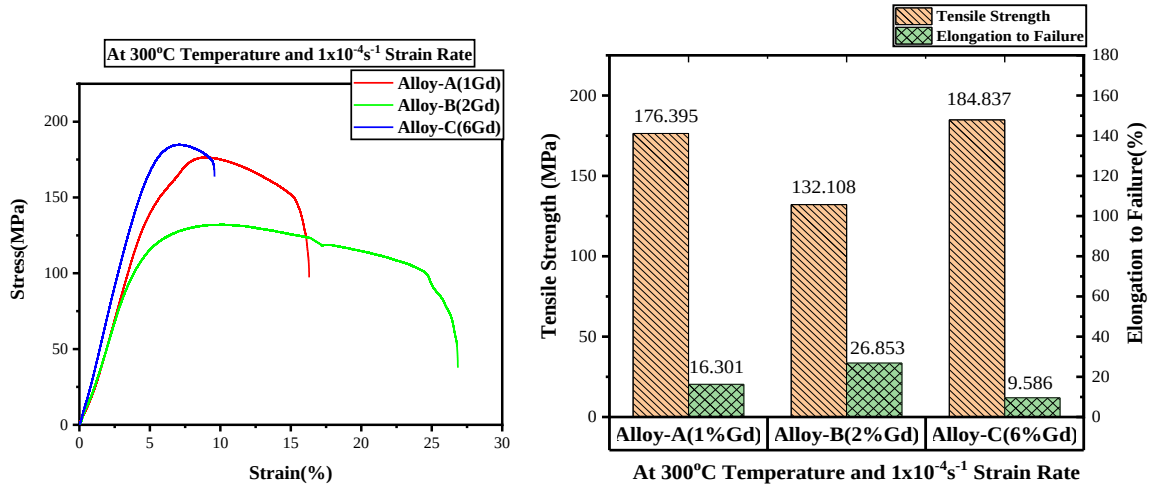

(a) (b)

Figure 4.20: Mg-1Zn-1.5Y-xGd (x=1, 2, 6%) alloys (a) Stress-Strain Curve, (b) Variation of Tensile Strength, Elongation to Failure, and Grain Size with Gd content at 300° C Temperature and $1x10^{-4}$ s^{-1} Strain Rate.

Tensile tests were conducted on three alloys at a temperature of 350° C and a strain rate of $1x10^{-4}$ s^{-1}, and the results are shown in Figure 4.21. Figure 4.21(a) displays the stress-strain curves of the three alloys, while Figure 4.21(b) illustrates the effect of Gd on the tensile strength, and the elongation capability.

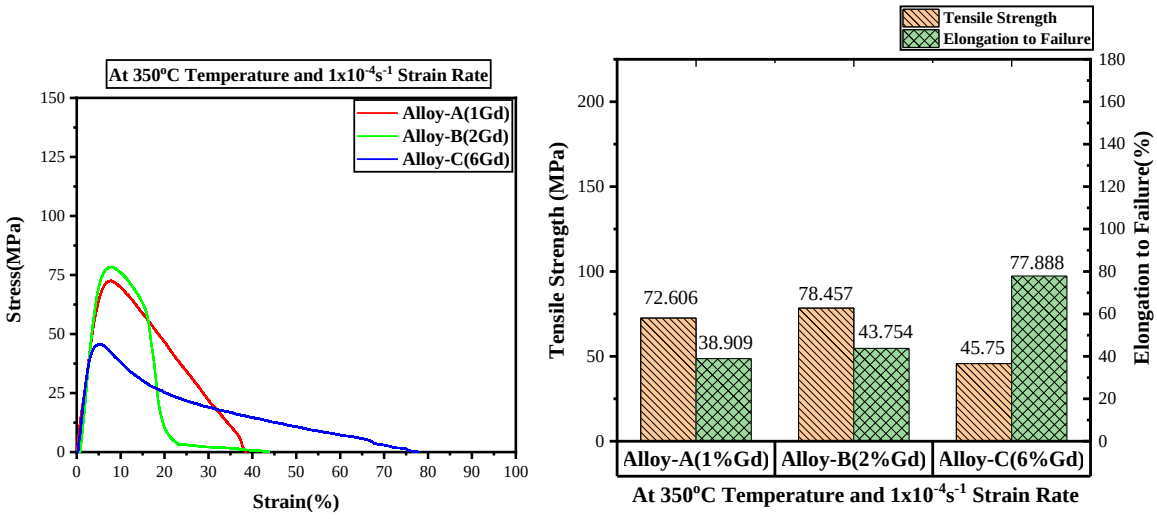

(a) (b)

Figure 4.21: Mg-1Zn-1.5Y-xGd (x=1, 2, 6%) alloys (a) Stress-Strain Curve, (b) Variation of Tensile Strength, Elongation to Failure, and Grain Size with Gd content at 350° C Temperature and $1x10^{-4}$ s^{-1} Strain Rate.

The tensile strength values of the three alloys were 72.606, 78.457, and 45.75 MPa, and the elongation values at failure were 38.909, 43.754, and 77.888%, respectively. The results indicate a trend where the tensile strength initially increased with the addition of Gd and then started to degrade with further addition, resulting in the highest tensile strength for alloy-B with 2% Gd. However, in the case of elongation, it increased with Gd addition and resulted in the highest elongation value for alloy-C. Therefore, at 350° C, alloy-B exhibited the highest tensile strength with 2% Gd, while alloy-C displayed the highest elongation capability among the three alloys.

Figure 4.22(a) shows the stress-strain curve for three alloys at 400° C and a strain rate of $1x10^{-4}$ s^{-1}. Meanwhile, Figure 4.22(b) demonstrates the effect of varying Gd content in the alloy.

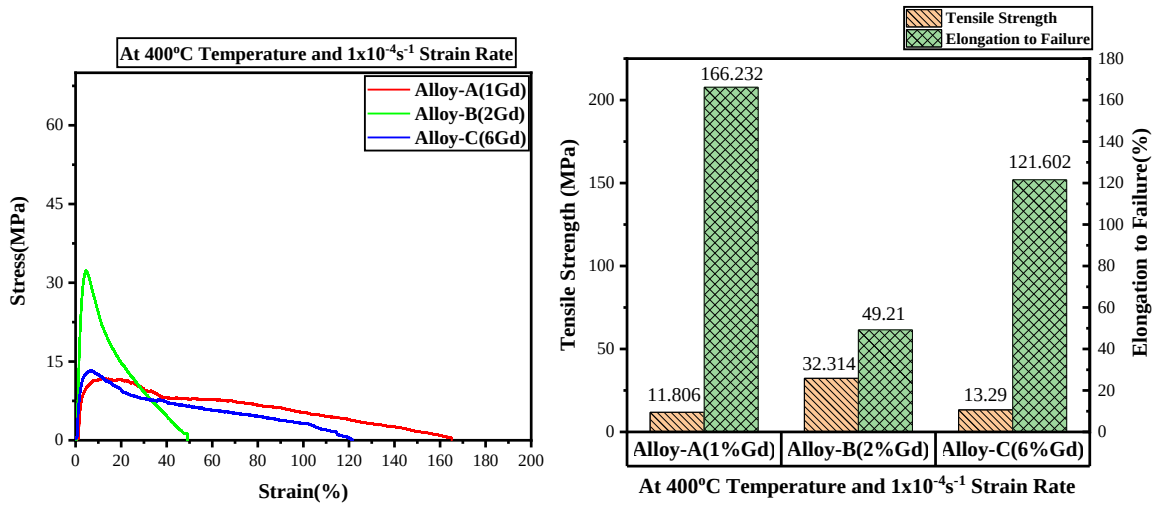

Figure 4.22: Mg-1Zn-1.5Y-xGd (x=1, 2, 6%) alloys (a) Stress-Strain Curve, (b) Variation of Tensile Strength, and Elongation to Failure with Gd content at 400ºC Temperature and $1x10^{-4}s^{-1}$ Strain Rate.

The tensile strength values for alloy-A, alloy-B, and alloy-C are 11.806 MPa, 32.314 MPa, and 13.29 MPa, respectively. These values indicate a significant decrease in tensile strength compared to the values obtained at 250, 300 and 350° C. The elongation to failure values for the three alloys are 166.232%, 49.21%, and 121.602%, respectively. At this elevated temperature and strain rate, tensile strength reached at maximum, 32.314 MPa, for addition of Gd up to 2%(alloy-B) and started to decrease for further addition of Gd. In contrast, elongation capacity of the alloys displayed the completely opposite trend. Therefore, alloy-B exhibits the highest tensile strength (32.314 MPa) and alloy-A exhibits the highest elongation to failure (166.232%).

At both strain rates ($1x10^{-4}$ and $5x10^{-4}$ s^{-1}), alloy-C has demonstrated superior tensile strength compared to the other two alloys at lower temperatures (250°C and 300°C), with a few exceptions. CALPHAD analysis revealed that alloy-C exhibited the highest volume fraction of the 14H-LPSO phase compared to alloy-A and alloy-B. This notable volume fraction of the blocky 14H-LPSO phase could explain the enhanced strength of alloy-C in contrast to the others as a previous study [38] indicated that the blocky 14H-LPSO phase possesses greater strengthening efficiency than the more film-like and lamellar LPSO phases.

However, at elevated temperatures (350°C and 400°C), alloy-B demonstrated promising performance due to a favorable combination of tensile strength and elongation. This strength can be attributed to the presence of a bimodal 14H-LPSO phase (a mixture of lamellar and blocky LPSO) as well as the W-phase at these elevated temperatures. The ductility can be linked to the dynamically recrystallized grains with weak texture, aligning well with findings from a previous study [93].

This changes of mechanical properties with increasing temperature could be also attributed to the change of deformation mechanism and dynamic recrystallization at elevated temperature. Different studies [75][102] reported that at low temperature, the dominant deformation process is the dislocation slip, while at high temperature, thermally activated mechanisms such as dynamic recrystallization, grain boundary sliding (GBS), the emergence of creep caused by diffusion or dislocation climb, are in charge.

At both strain rates ($5x10^{-4}$ and $1x10^{-4}$ s^{-1}), the elongation percentage of alloy-B (2% Gd) is found to be lower than the other two alloys at higher temperatures (350^{o} C and 400^{o} C). In a previous study [94], the presence of the W-phase in Mg-Zn-Y-Gd alloys was found to cause a pinning effect, resulting in reduced plastic deformation and elongation. Therefore, the lower elongation, observed in alloy-B at 350^{o} C and 400^{o} C temperatures, can be attributed to this pinning effect of W-phase present in alloy.

4.6.3 Effect of Strain Rate on Tensile Strength and Elongation

The variation in tensile strength with Gd concentration at strain rates of $5x10^{-4}$ s^{-1} and $1x10^{-4}$ s^{-1} at various temperatures (250° C, 300° C, 350° C and 400° C) is depicted in Figure 4.23.

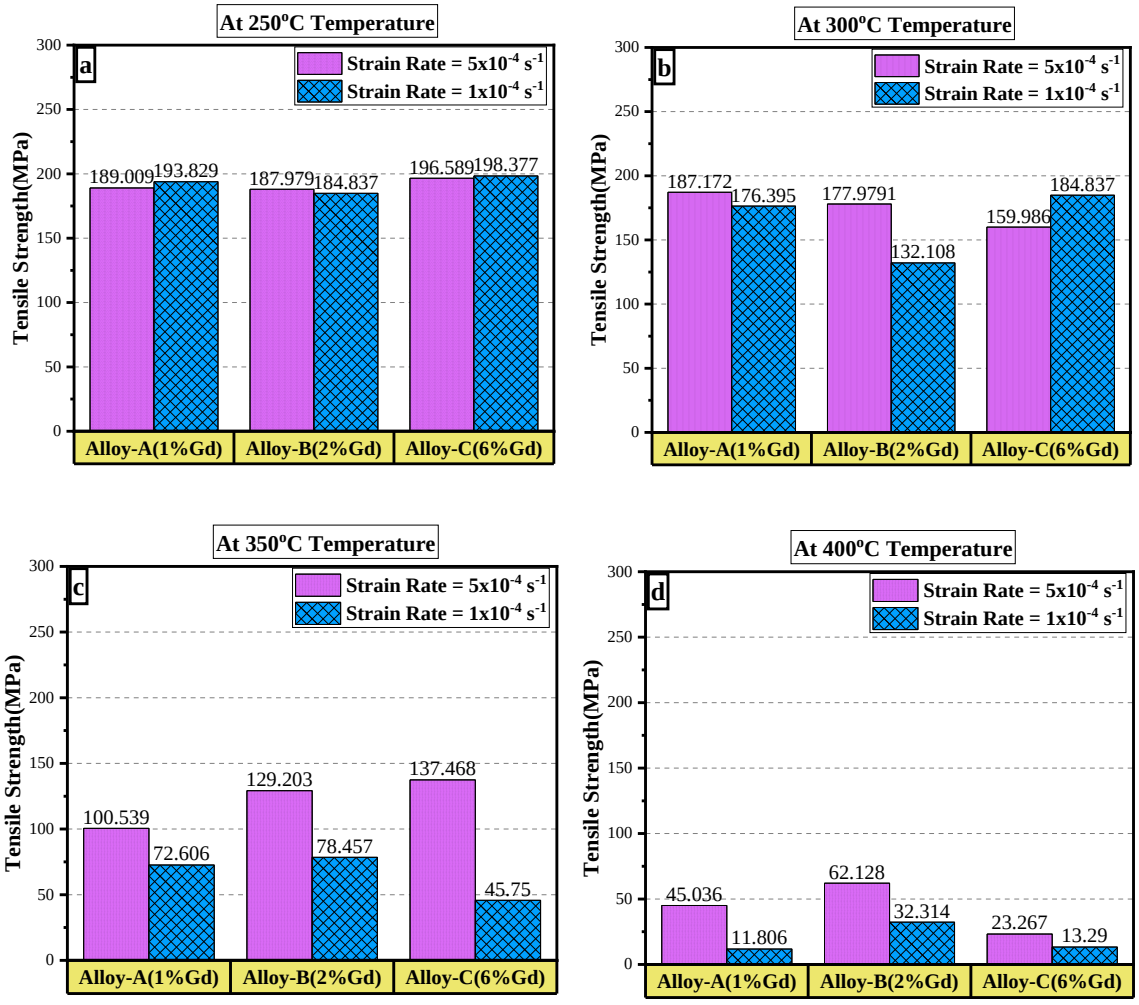

Figure 4.23: Tensile Strength at temperature (a) 250° C, (b) 300° C, (c) 350° C and (d) 400° C with variation of Gd content(%) at the strain rate $5x10^{-4}$ s^{-1} and $1x10^{-4}$ s^{-1}

At lower temperature, the tensile strength difference between slower strain rate and higher strain rate is observed less (Figure 4.23(a)), but with increasing temperature the difference increased and found maximum for 350° C in Figure 4.23.

At a lower temperature of 250° C, the tensile strength of Alloy-A and Alloy-C was found to be higher with small difference at a low strain rate ($1x10^{-4}$ s^{-1}), with values of 193.826 MPa and 198.377 MPa, respectively, compared to their tensile strength at a higher strain rate ($5x10^{-4}$ s^{-1}). Similarly, at 300°C, Alloy-C exhibited a higher tensile strength (184.837 MPa) than Alloy-A (159.986 MPa) at the lower strain rate. However, for all other alloys, higher tensile strengths were observed at the higher strain rates compared to the lower ones.

A previous study [103] observed that slower strain rates lead to greater grain growth, resulting in larger grain sizes compared to higher strain rates. According to the Hall-Petch relationship [104], larger grain size typically results in lower strength values. As a result,

the higher tensile strength observed at higher strain rates in our study can be attributed to the formation of smaller grains due to dynamic recrystallization during the tensile test.

In Figure 4.24, elongation to failure at different temperatures (250, 300, 350, and 400°C) with variation Gd content at strain rates $5x10^{-4}$ and $1x10^{-4}$ s^{-1} is shown.

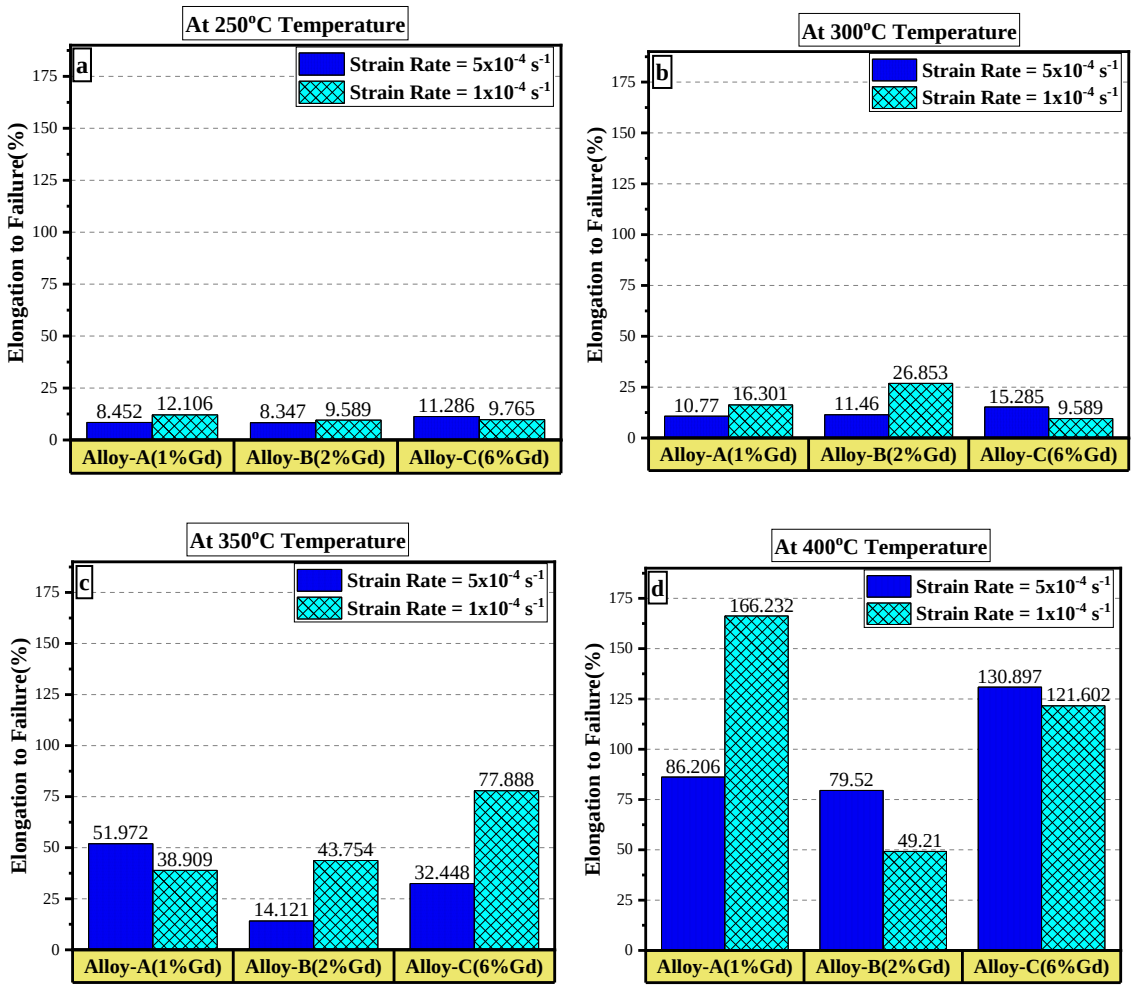

Figure 4.24: Elongation to Failure at temperature (a) 250° C, (b) 300° C, (c) 350° C and (d) 400° C with variation of Gd content(%) at the strain rate $5x10^{-4}$ s^{-1} and $1x10^{-4}$ s^{-1}

With the exception of 400° C temperature, strain rate $5x10^{-4}$ s^{-1} generally exhibits a tendency of lesser elongation to failure than the strain rate $1x10^{-4}$ s^{-1}, which is consistent with earlier research [105]. Because grain growth occurs at higher rate at a reduced strain rate ($1x10^{-4}$ s^{-1}), this can delay the creation of a neck. Materials can elongate further at this time, leading to failure. At 250° C, all alloys show nearly similar elongation to failure with small differences (1-3%) among them. Elongation to failure increased at 300° C [Figure 4.24(b)] with increasing Gd content (%), but as Gd concentration grew further, elongation

to failure decreased. This is due to the fact that a significant amount of intermetallic particles caused the earlier elongation to fail. However, at higher temperature (350^{o} C and 400^{o} C), a changed trend is observed- with increasing Gd elongation capacity decreased at first and then start to increase again. This observation indicates to the pinning effect of W-phase, that is found in alloy-B, degrade the plastic deformation behavior of alloy.[94] With increase of Gd up to 6%, W-phase disappeared and amount of 14H-LPSO increased results in higher elongation capacity for alloy-C. Besides, in an study [106] it is found that the formation of precipitation results in age-softening responses, which enhance the total elongation of the material.

It has been observed from Figure 4.23 and Figure 4.24 that at elevated temperatures, the flow stress or tensile strength is reduced, and the elongation to failure increases regardless of the strain rate. In previous several studies [107], it was found that the obstacle of activating dislocation slip caused by the strong basal texture at room temperature is relieved due to lowered critical resolved shear stress (CRSS) values at high temperature. Therefore, the reduction of flow stress and significant improvement in the elongation can be attributed to that lowered CRSS value.

4.7 Deformation Mechanism on Grain Growth

4.7.1 Activation Energy Calculation

The relationship between deformation temperature, strain rate, and flow stress can be described by the power exponent function, exponential function, and hyperbolic sine function for the alloy's high temperature deformation [108]. These are the equations:

$$\acute{\varepsilon} = A_1\sigma^{n1}\exp\left(\frac{-Q}{RT}\right) \quad \ldots\ldots\ldots\ldots (1)$$

$$\acute{\varepsilon} = A_2 \exp(\beta\sigma) \exp\left(\frac{-Q}{RT}\right) \quad \ldots\ldots\ldots\ldots (2)$$

$$\acute{\varepsilon} = A_3 [\sinh(\alpha\sigma)]^n \exp\left(\frac{-Q}{RT}\right) \quad \ldots\ldots\ldots\ldots(3)$$

Where Q is hot deformation activation energy(kJ/mol), T represents the absolute temperature, and R is the molar gas constant (8.31 J/mol). n_1, β, α, n, and A(A_1, A_2, A_3) are the constants for materials, in that case $\alpha = \beta/n_1$. By taking natural logarithms of equation (1), (2) and (3), it could be written as follow:

$$\ln \acute{\varepsilon} = n_1 \ln\sigma + \ln A_1 + \left(\frac{-Q}{RT}\right) \quad \ldots\ldots\ldots\ldots(4)$$

$\ln \dot{\varepsilon} = \beta\sigma + \ln A_2 + \left(\frac{-Q}{RT}\right)$…… (5)

$\ln \dot{\varepsilon} = n \ln[\sinh(\alpha\sigma)] + \ln A_3 + \left(\frac{-Q}{RT}\right)$ ……..…..(6)

$\ln[\sinh(\alpha\sigma)] = \frac{-Q}{R} \cdot \frac{1}{T} + \frac{1}{n}(\ln \dot{\varepsilon} - \ln A_3)$ …… (7)

Eq. (7) can be used to derive the linear relationship in between ln[sinh(ασ)] and 1/T when the strain rate is constant. Q is computed because the other values were constants. Q can be written as follows:

$Q = R\, n \left(\frac{\delta ln[sinh(\alpha\sigma)]}{\delta(\frac{1}{T})}\right)$……..… (8)

In Figure 4.25, Figure 4.26, and Figure 4.27, plots are shown for calculating material constants, n_1, β, α, and n of alloy-A, B, and C respectively. Activation energies for different temperature and strain rate have been evaluated using equation-8.

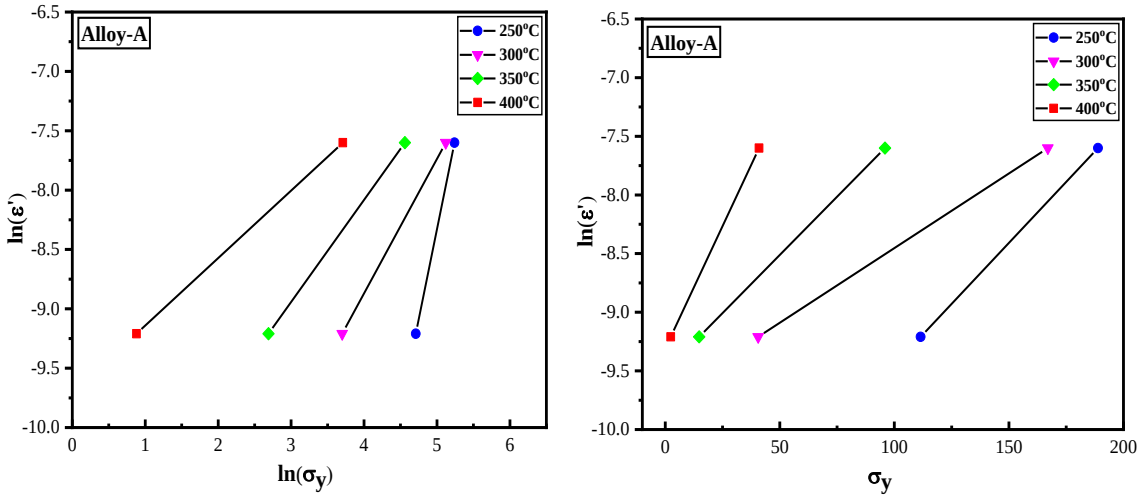

(a) (b)

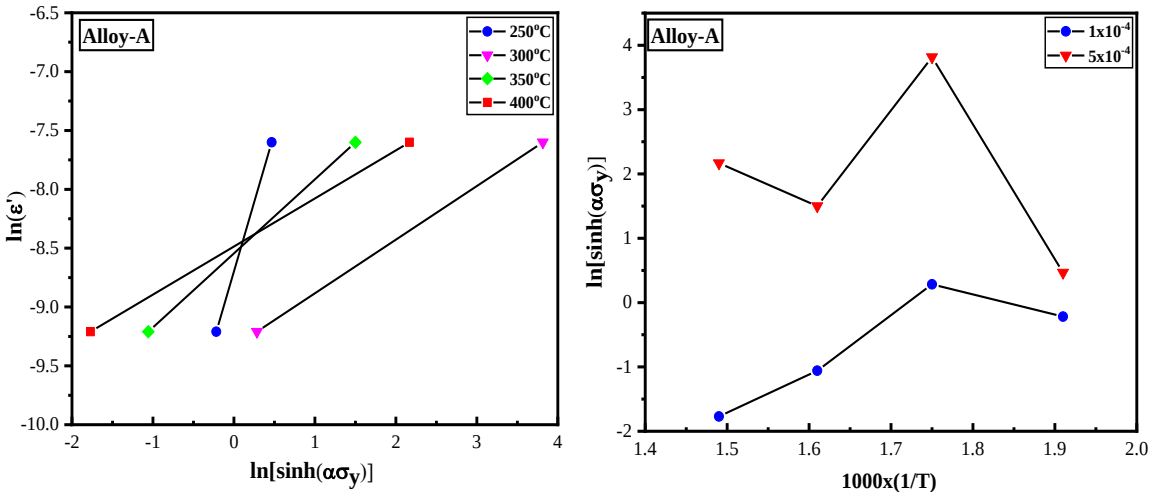

(c) (d)

Figure 4.25: Plots for calculating the hot deformation constants n_1, β, n and Activation Energy, Q of Alloy-A- (a) ln(έ)-ln(σ_y), (b) ln(έ)-ln[sinh(ασ_y)], (c) ln(έ)-ln[sinh(ασ_y)], (d) ln[sinh(ασ_y)]-1000x(1/T)

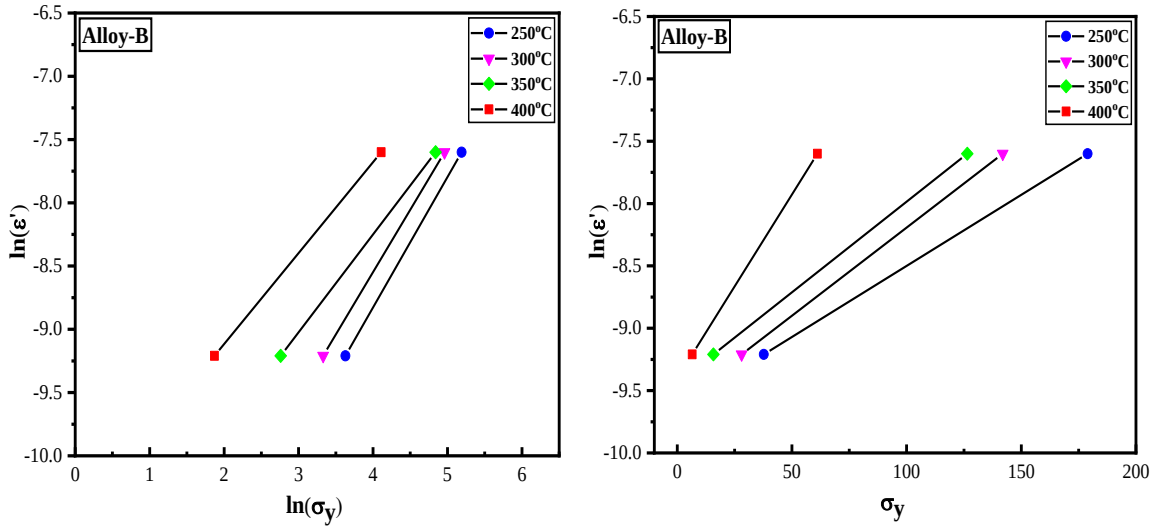

(a) (b)

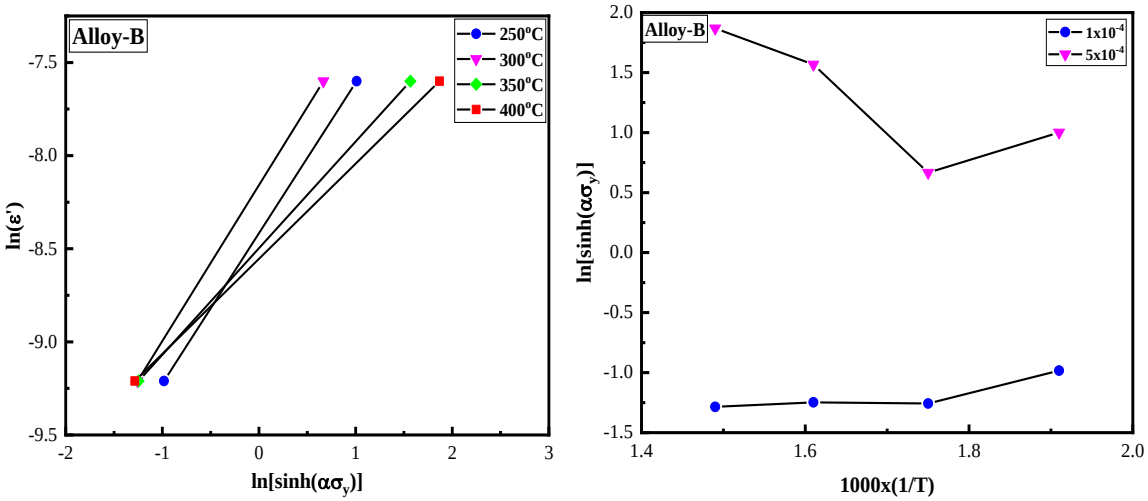

(c) (d)

Figure 4.26: Plots for calculating the hot deformation constants n_1, β, n and Activation Energy, Q of Alloy-B- (a) ln(έ)-ln(σ_y), (b) ln(έ)-ln[sinh(ασ_y)], (c) ln(έ)-ln[sinh(ασ_y)], (d) ln[sinh(ασ_y)]-1000x(1/T)

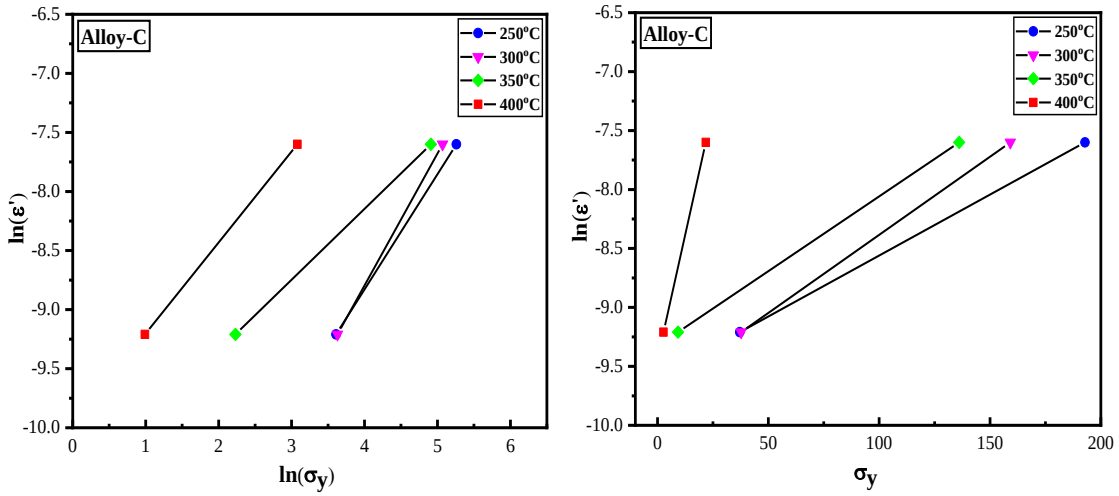

(a) (b)

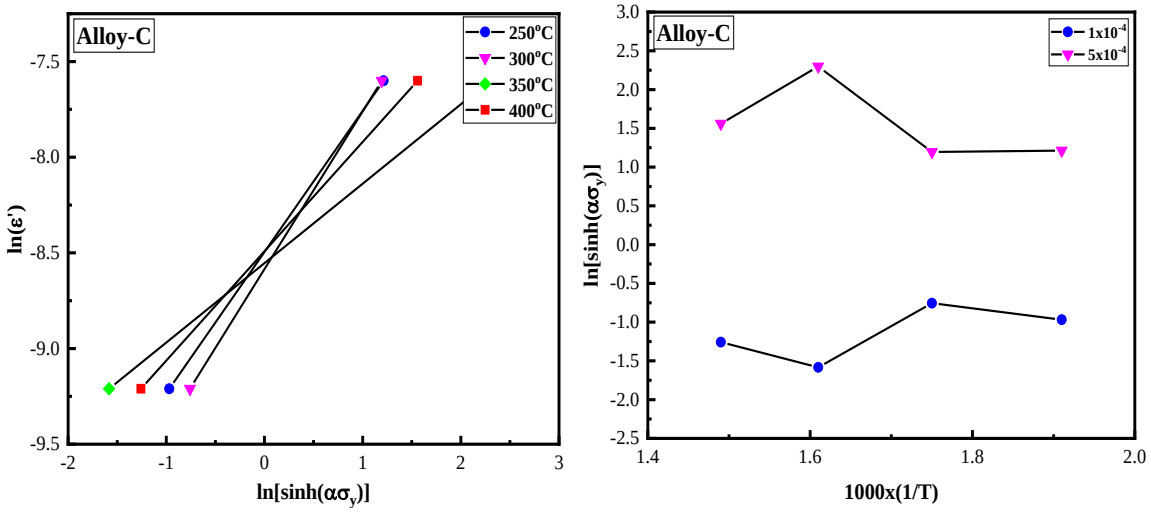

(c) (d)

Figure 4.27: Plots for calculating the hot deformation constants n_1, β, n and Activation Energy, Q of Alloy-C- (a) ln(έ)-ln(σ_y), (b) ln(έ)-ln[sinh(ασ_y)], (c) ln(έ)-ln[sinh(ασ_y)], (d) ln[sinh(ασ_y)]-1000x(1/T)

Table 4.7: Calculated Values of Q at $1x10^{-4}$ s^{-1} Strain Rate

Alloy	Activation Energy, Q (kJ/mol)		
	250°-300° C	300°-350° C	350°-400° C
Alloy-A	24.03 (Grain boundary diffusion)	76.52 (Grain boundary diffusion)	40.65 (Grain boundary diffusion)
Alloy-B	56.881 (Grain boundary diffusion)	36.4 (Grain boundary diffusion)	14.28 (Grain boundary diffusion)
Alloy-C	54.824 (Grain boundary diffusion)	31.14 (Grain boundary diffusion)	12.28 (Grain boundary diffusion)

Table 4.8: Calculated Values of Q at $5x10^{-4}$ s^{-1} Strain Rate

Alloy	Activation Energy, Q (kJ/mol)		
	250°-300° C	300°-350° C	350°-400° C
Alloy-A	190.95 (Lattice diffusion)	133.99 (Lattice diffusion)	44.67 (Grain boundary diffusion)

Alloy	Activation Energy, Q (kJ/mol)		
	250°-300° C	300°-350° C	350°-400° C
Alloy-B	120.16 (Lattice diffusion)	101.17 (Grain boundary diffusion)	75.98 (Grain boundary diffusion)
Alloy-C	76.398 (Grain boundary diffusion)	41.72 (Grain boundary diffusion)	27.89 (Grain boundary diffusion)

In Table 4.7 and 4.8, calculated values of activation energy are presented for the strain rate $1x10^{-4}$ s^{-1} and $5x10^{-4}$ s^{-1}, respectively. In pure Mg, the activation energies for lattice self-diffusion and grain boundary diffusion, respectively, are 135 kJ/mol and 92 kJ/mol [71]. According to table 4.7, activation energy values for lower strain rates $1x10^{-4}$ s^{-1} range from 13 to 77 kJ/mol, which are less than 135 kJ/mol. Therefore, here grain boundary diffusion mechanism acts as deformation mechanism. However, some activation energy values, nearer or above, 135 kJ/mol are seen at higher strain rates $5x10^{-4}$ s^{-1}. As a result, it is clear from the values that the deformation process changed from the grain boundary diffusion to the lattice diffusion, with the strain rate changing from low to high.

On the basis of just two values of Q, deformation mechanisms have been determined. As a result, employing activation energy values to identify deformation mechanisms is improper. For understanding deformation mechanisms in practice, the strain rate sensitivity index or strain hardening exponent are used.

4.7.2 Values of Strain Exponent(n) and Strain Rate Sensitivity(m) Index Calculation

The response of the material to strain hardening under tension in various directions and temperatures follows a parabolic trend. In order to fully understand this hardening response, the power law relationship was utilized to define the strain exponent. From relation of the true stress and the true strain [109],

$\sigma = K \varepsilon^n$

where,

ε is true strain;

σ is true stress;

n is strain exponent.

By curve fitting of the true stress-strain curve, values of strain exponent(n) have been determined for alloy A, B and C at each test temperature and strain rate. In Figure 4.28 to Figure 4.33, fitted curves have been presented.

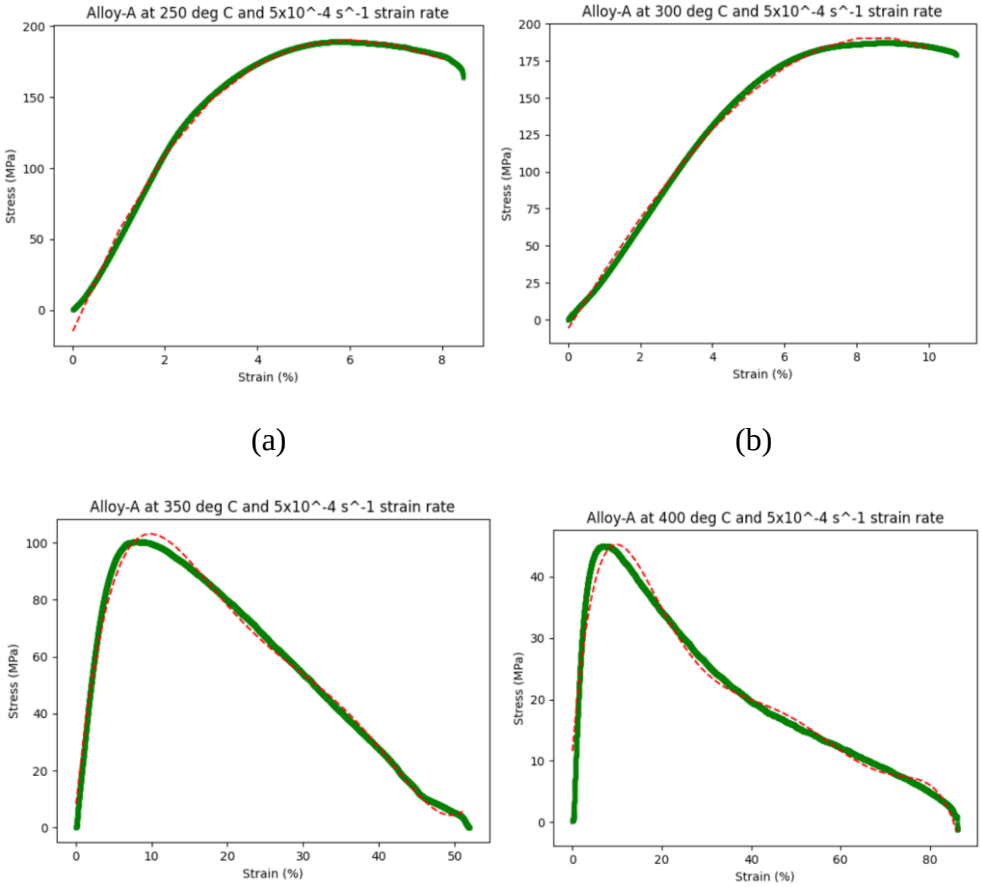

(a) (b)

(c) (d)

Figure 4.28: Curve fitting of Stress-Strain Curve of alloy-A for $5x10^{-4}$ s^{-1} Strain Rate at (a) 250° C, (b) 300° C, (c) 350° C and (d) 400° C Temperature

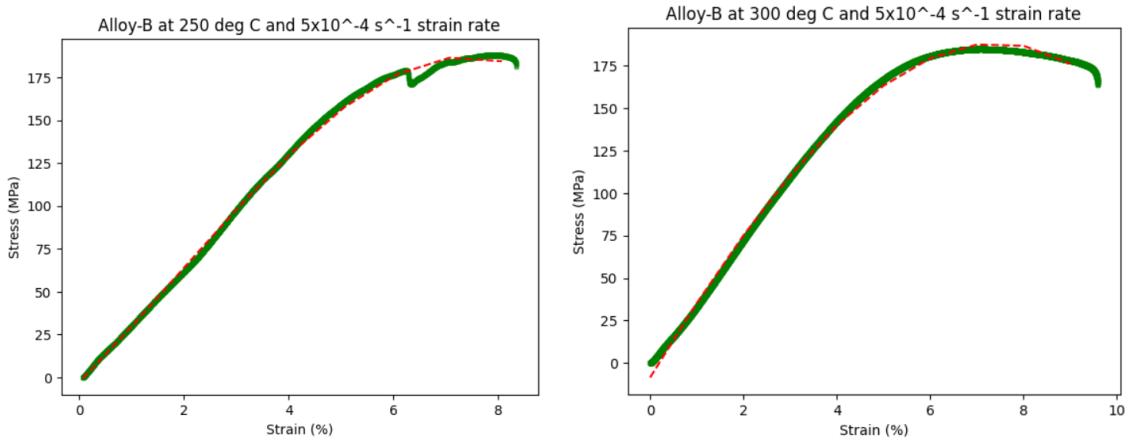

(a) (b)

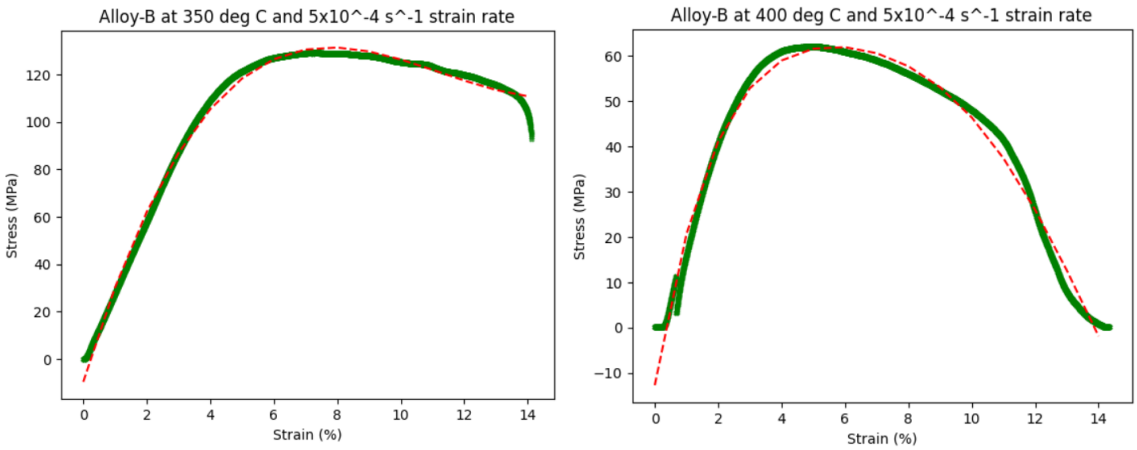

(c) (d)

Figure 4.29: Curve fitting of Stress-Strain Curve of alloy-B for $5x10^{-4}$ s^{-1} Strain Rate at (a) 250º C, (b) 300º C, (c) 350º C and (d) 400º C Temperature

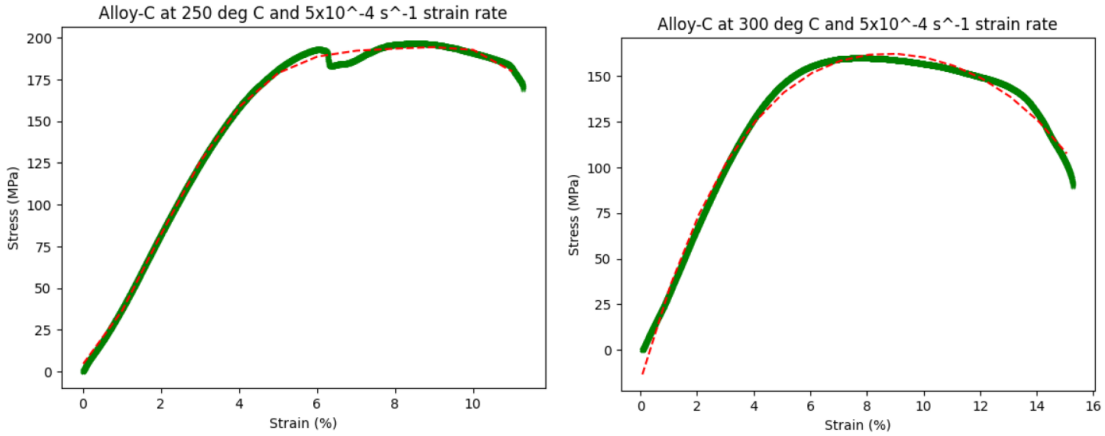

(a) (b)

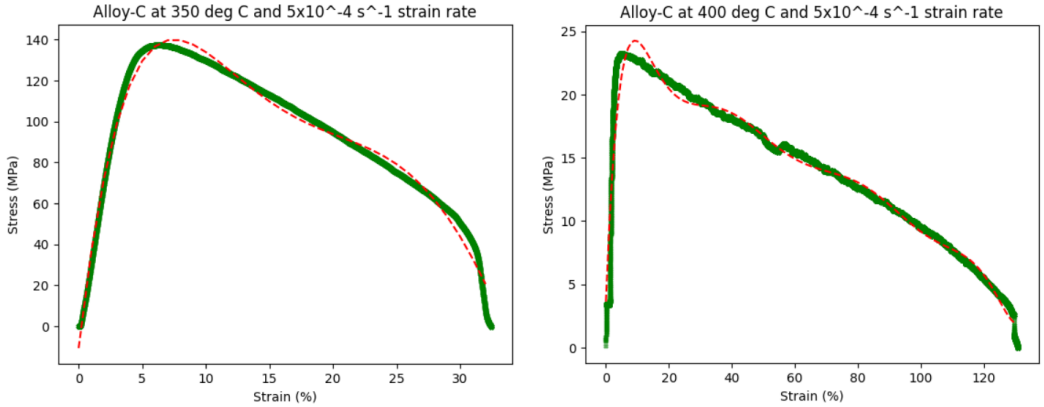

(c) (d)

Figure 4.30: Curve fitting of Stress-Strain Curve of alloy-C for $5x10^{-4}$ s^{-1} Strain Rate at (a) 250º C, (b) 300º C, (c) 350º C and (d) 400º C Temperature

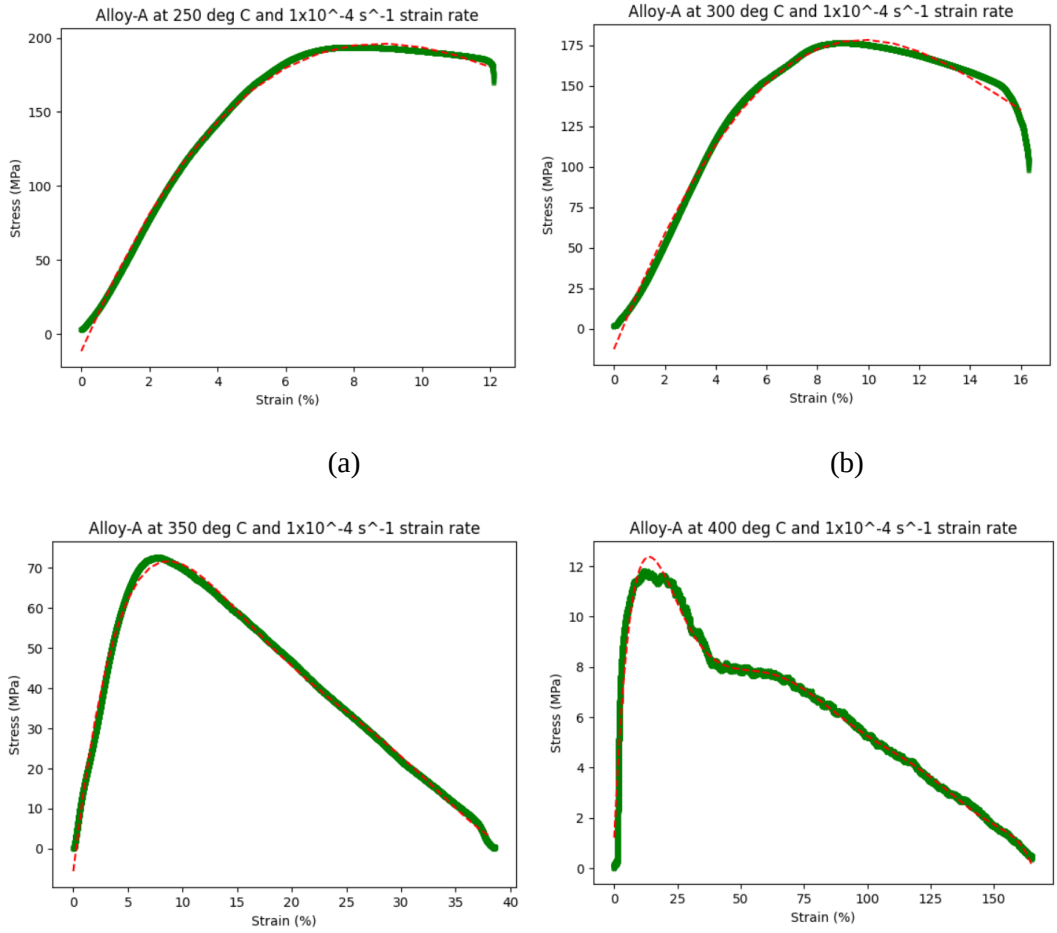

Figure 4.31: Curve fitting of Stress-Strain Curve of alloy-A for $1x10^{-4}$ s^{-1} Strain Rate at (a) 250º C, (b) 300º C, (c) 350º C and (d) 400º C Temperature

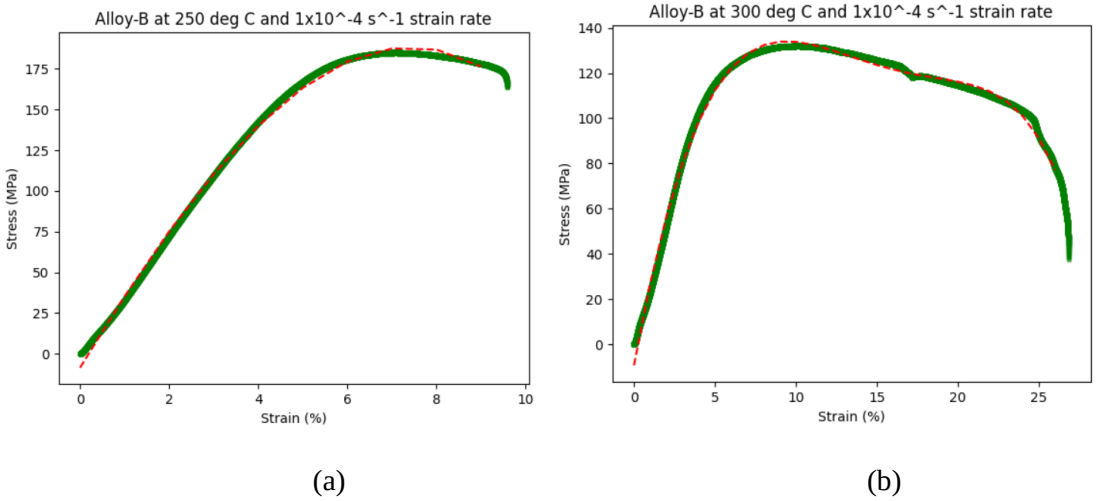

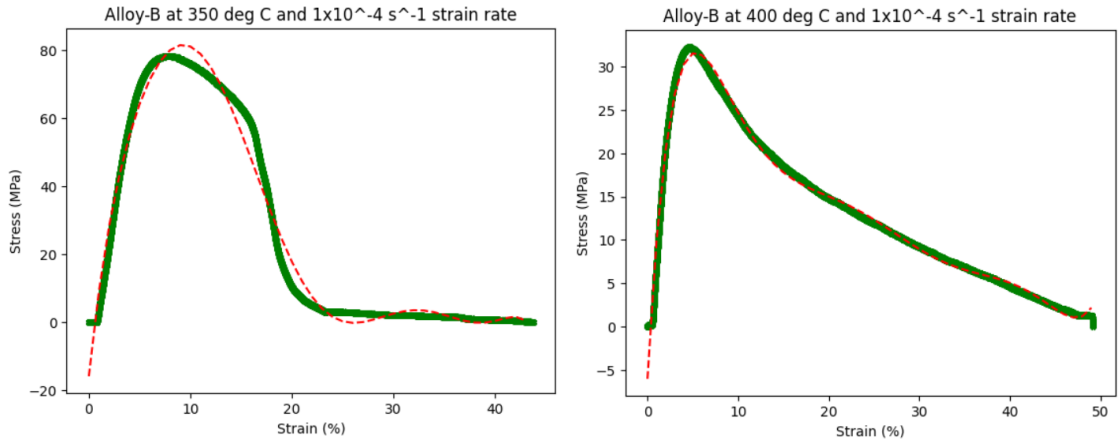

(c) (d)

Figure 4.32: Curve fitting of Stress-Strain Curve of alloy-B for $1x10^{-4}$ s^{-1} Strain Rate at (a) 250º C, (b) 300º C, (c) 350º C and (d) 400º C Temperature

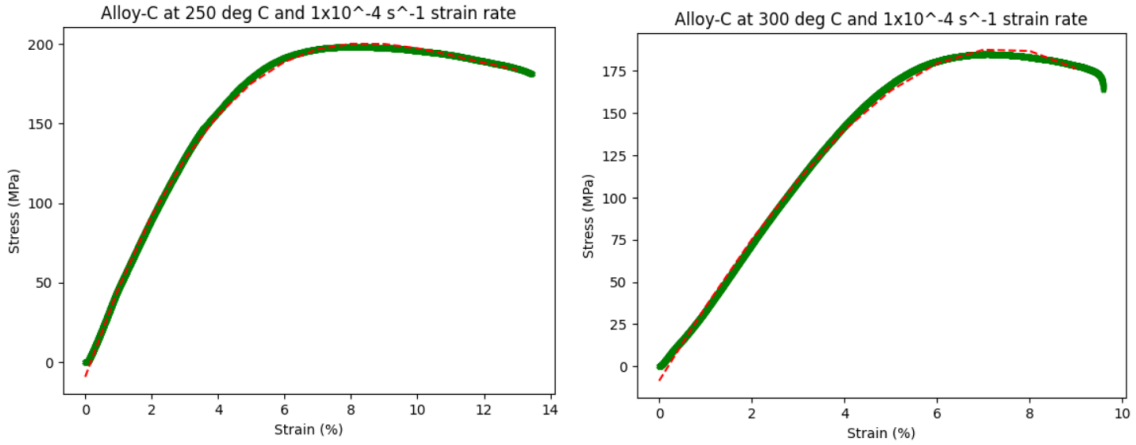

(a) (b)

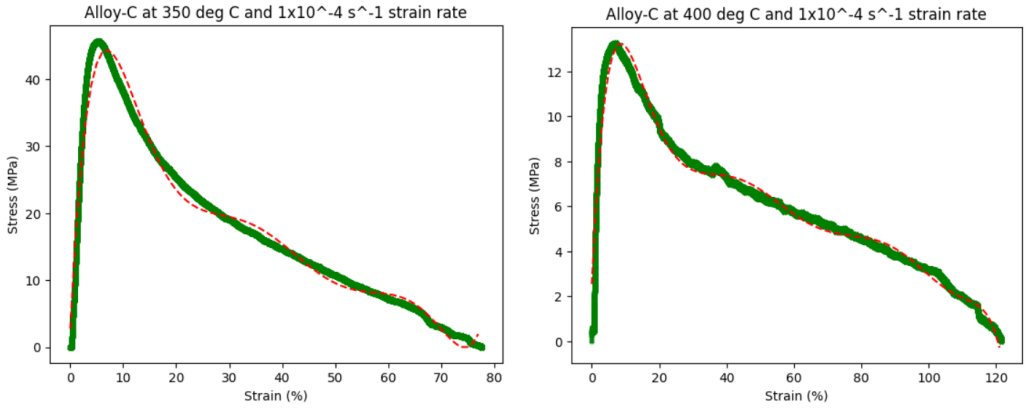

(c) (d)

Figure 4.33: Curve fitting of Stress-Strain Curve of alloy-C for $1x10^{-4}$ s^{-1} Strain Rate at (a) 250º C, (b) 300º C, (c) 350º C and (d) 400º C Temperature

Below is a list of different n values for deformation mechanisms at high temperatures [72]:

n= 1 (Diffusional creep)

n= 2 (Grain boundary sliding)

n= 3 (Glide-controlled creep)

n= 4-5 (Climb-controlled creep)

n> 8 (Dispersion-strengthened alloy)

The values of n at strain rates of $1x10^{-4}$ s^{-1} and $5x10^{-4}$ s^{-1} are shown in Table 4.9 and Table 4.10, respectively.

Table 4.9: Values of the Strain Exponent(n) at strain rate $1x10^{-4}$ s^{-1}

Alloy	**Strain Exponent(n)**			
	250ºC	**300ºC**	**350ºC**	**400ºC**
Alloy-A (Mg-1Zn-1.5Y-1Gd)	8.86 (Dispersion Strengthened)	7.34 (Dispersion Strengthened)	6.25 (Climb-controlled Creep)	2.75 (Grain-boundary Sliding)
Alloy-B (Mg-1Zn-1.5Y-2Gd)	8.45 (Dispersion Strengthened)	5.67 (Climb-controlled Creep)	4 (Climb-controlled Creep)	2.94 (Grain-boundary Sliding)
Alloy-C (Mg-1Zn-1.5Y-6Gd)	9.54 (Dispersion Strengthened)	7.8 (Dispersion Strengthened)	2.58 (Grain-boundary Sliding)	3.44 (Glide-controlled Creep)

Table 4.10: Values of the Strain Exponent(n) at strain rate $5x10^{-4}$ s^{-1}

Alloy	**Strain Exponent(n)**			
	250°C	**300°C**	**350°C**	**400°C**
Alloy-A (Mg-1Zn-1.5Y-1Gd)	8.87 (Dispersion Strengthened)	6.76 (Dispersion Strengthened)	3.45 (Glide-controlled Creep)	2.33 (Grain-boundary Sliding)
Alloy-B (Mg-1Zn-1.5Y-2Gd)	9.65 (Dispersion Strengthened)	7.67 (Dispersion Strengthened)	3.56 (Glide-controlled Creep)	2.5 (Grain-boundary Sliding)
Alloy-C (Mg-1Zn-1.5Y-6Gd)	9.30 (Dispersion Strengthened)	7.73 (Dispersion Strengthened)	2.08 (Grain-boundary Sliding)	2.45 (Grain-boundary Sliding)

Depending on the analysis of the strain exponent value (n) from Table 4.9 and Table 4.10, it is evident that at low temperatures, dominant deformation mechanisms include dispersion-strengthened and climb-controlled creep. However, at higher temperatures (350° C and 400° C) and slow strain rates, grain boundary sliding (GBS) emerges as the primary deformation mechanism, with a few exceptions. Many studies [110] have also found that grain boundary sliding is a prevalent deformation mechanism observed at low strain rates, elevated temperatures, and in grains with small sizes. The exact mechanism governing grain boundary sliding (GBS) activity is a subject of debate within the research community, with most studies proposing either vacancy diffusion or dislocation motion (climb and glide) within the grain boundary plane as driving mechanisms for GBS [111]. Several analyses [110] reported that the combination of resolved shear stress at the grain boundary plane and boundary straightness constitutes a set of criteria for predicting the propensity of sliding.

The strain rate sensitivity (SRS) index is regarded as a most reliable parameter to understand and explain the deformation mechanisms during various thermo-mechanical processing [112]. The effects of strain rate sensitivity were initially researched by Backofen et al. [76]. They devised a power-law constitutive equation that included quantitative index for measuring strain rate sensitivity that is as follow:

$\sigma = K\,\dot{\varepsilon}^{m}$

Here, K is a material constant, σ is the true flow stress, $\dot{\varepsilon}$ is the true strain rate, and m is the strain rate sensitivity, which could be calculated as follows:

$$m = \frac{\partial log\sigma}{\partial log\dot{\varepsilon}} \quad \text{.....(2)}$$

In several previous studies, the SRS index has been employed as an effective parameter to determine how the deformation mechanisms change in Mg alloy with temperature [112] [113]. Below are the deformation mechanisms for various m values [72]:

m= 1 (Diffusional creep)

m= 0.5 (Grain boundary sliding)

m= 0.33 (Glide-controlled creep)

m= 0.14-0.25 (Climb-controlled creep)

m< 0.125 (Dispersion-strengthened alloy)

Table 4.11 and Table 4.12 show the values of 'm' at strain rates of $1x10^{-4}$ s^{-1} and $5x10^{-4}$ s^{-1}, respectively. These values were measured from the data sets presented in Figure 4.34 by employing equation (2).

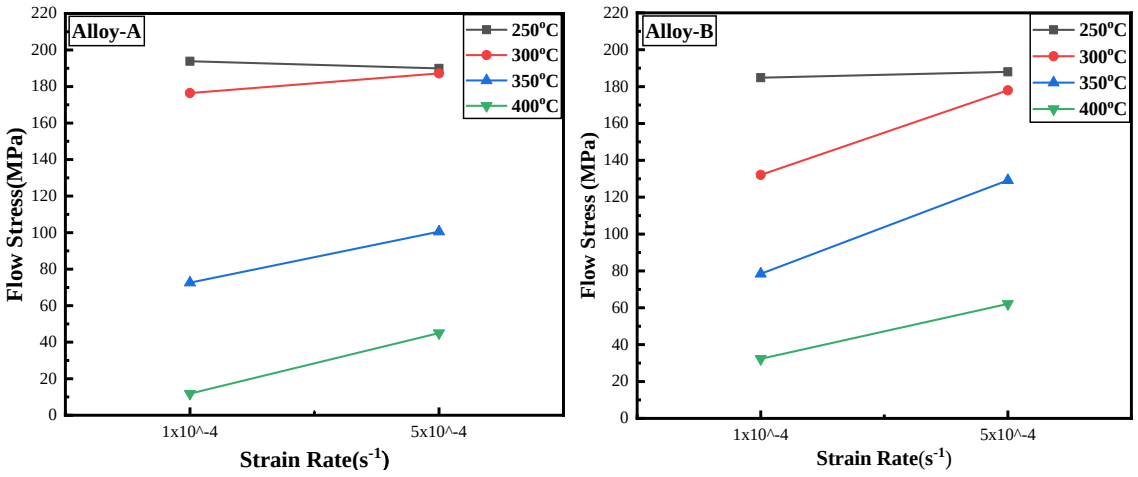

(a) (b)

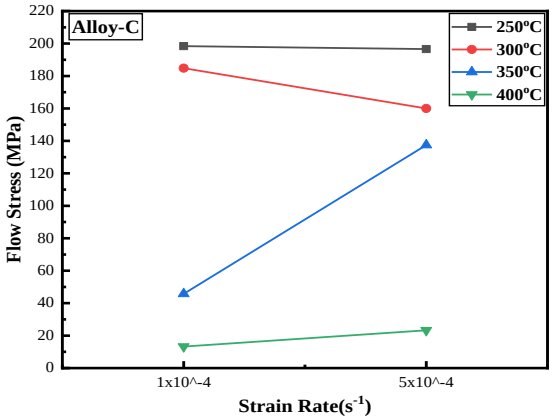

(c)

Figure 4.34: Variation in the Flow Stress with Strain Rate for (a) Alloy-A, (b) Alloy-B and (c) Alloy-C for Each Test Conditions

Table 4.11: Value of m at strain rate $1x10^{-4}$ s^{-1}

Alloy Composition	Strain Rate Sensitivity Index(m)			
	250° C	300° C	350° C	400° C
Alloy-A (Mg-1Zn-1.5Y-1Gd)	0.01 (Dispersion Strengthened)	0.03 (Dispersion Strengthened)	0.16 (Climb-Controlled Creep)	0.8 (Grain-Boundary sliding)
Alloy-B (Mg-1Zn-1.5Y-2Gd)	0.01 (Dispersion Strengthened)	0.15 (Climb-Controlled Creep)	0.25 (Climb-Controlled Creep)	0.34 (Glide-Controlled Creep Creep)
Alloy-C (Mg-1Zn-1.5Y-6Gd)	0.01 (Dispersion Strengthened)	0.02 (Dispersion Strengthened)	0.63 (Grain-Boundary sliding)	0.29 (Glide-Controlled Creep Creep)

Table 4.12: Value of m at strain rate $5x10^{-4}$ s^{-1}

Alloy Composition	Strain Rate Sensitivity Index(m)			
	250° C	300° C	350° C	400° C
Alloy-A (Mg-1Zn-1.5Y-1Gd)	0.02 (Dispersion Strengthened)	0.06 (Dispersion Strengthened)	0.29 (Glide-controlled creep)	0.89 (Diffusional creep)
Alloy-B (Mg-1Zn-1.5Y-2Gd)	0.02 (Dispersion Strengthened)	0.27 (Glide-controlled creep)	0.43 (Grain-Boundary sliding)	0.54 (Grain-Boundary sliding)

Alloy Composition	Strain Rate Sensitivity Index(m)			
	250° C	300° C	350° C	400° C
Alloy-C (Mg-1Zn-1.5Y-6Gd)	0.04 (Dispersion Strengthened)	0.14 (Dispersion Strengthened)	0.8 (Grain-Boundary sliding)	0.48 (Grain-Boundary sliding)

Table 4.11 and Table 4.12 demonstrate how increasing temperature influences the strain rate sensitivity of the alloy at strain rates of $1x10^{-4}$ s^{-1} and $5x10^{-4}$ s^{-1}. Furthermore, the impact of Gd addition on strain rate sensitivity and deformation mechanism can also be understood. In most cases, a dispersed strengthening mechanism has been observed at lower temperatures (250° and 300° C), which transitions into climb-controlled creep, glide-controlled creep, and grain-boundary sliding at higher temperatures (350° and 400° C).

In Figure 4.35, values of strain rate sensitivity(m) have been plotted against temperature to see how the temperature controls the strain rate sensitivity of an alloy while throughout the tensile test strain rate is kept constant i.e. $1x10^{-4}$ s^{-1} and $5x10^{-4}$ s^{-1}.

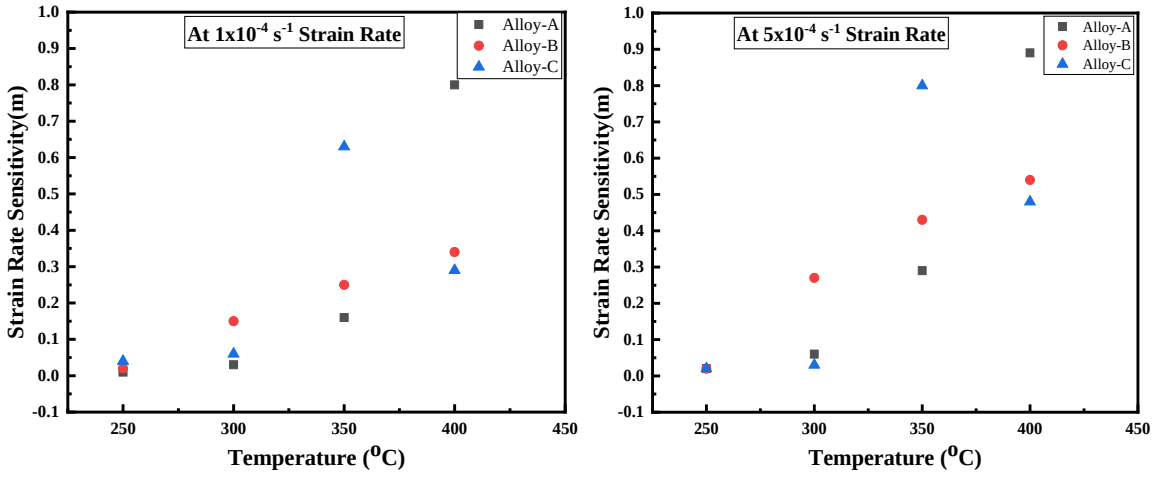

(a) (b)

Figure 4.35: Plot of Strain Rate Sensitivity vs. Temperature for alloy-A, alloy-B, and alloy-C at (a) $1x10^{-4}$ s^{-1} and (b) $5x10^{-4}$ s^{-1} Strain Rate.

For both strain rates, the values of strain rate sensitivity (m) are found to increase with temperature up to 400° C for alloy-A and B. However, alloy C has exhibited a different trend. In the case of alloy C, the strain rate sensitivity has reached its highest value at 350° C and then decreased at 400° C.

Figure 4.36 (a, b, c) demonstrate the impact of strain rate on the m for alloys A, B, and C at different test temperatures. The figures show that the strain rate sensitivity (m) increases with the strain rate for all temperatures. At higher temperatures (350° C and 400° C), a larger difference in the values of m is observed. Therefore, it can be concluded that strain rate has a significant influence on the strain rate sensitivity at higher temperatures.

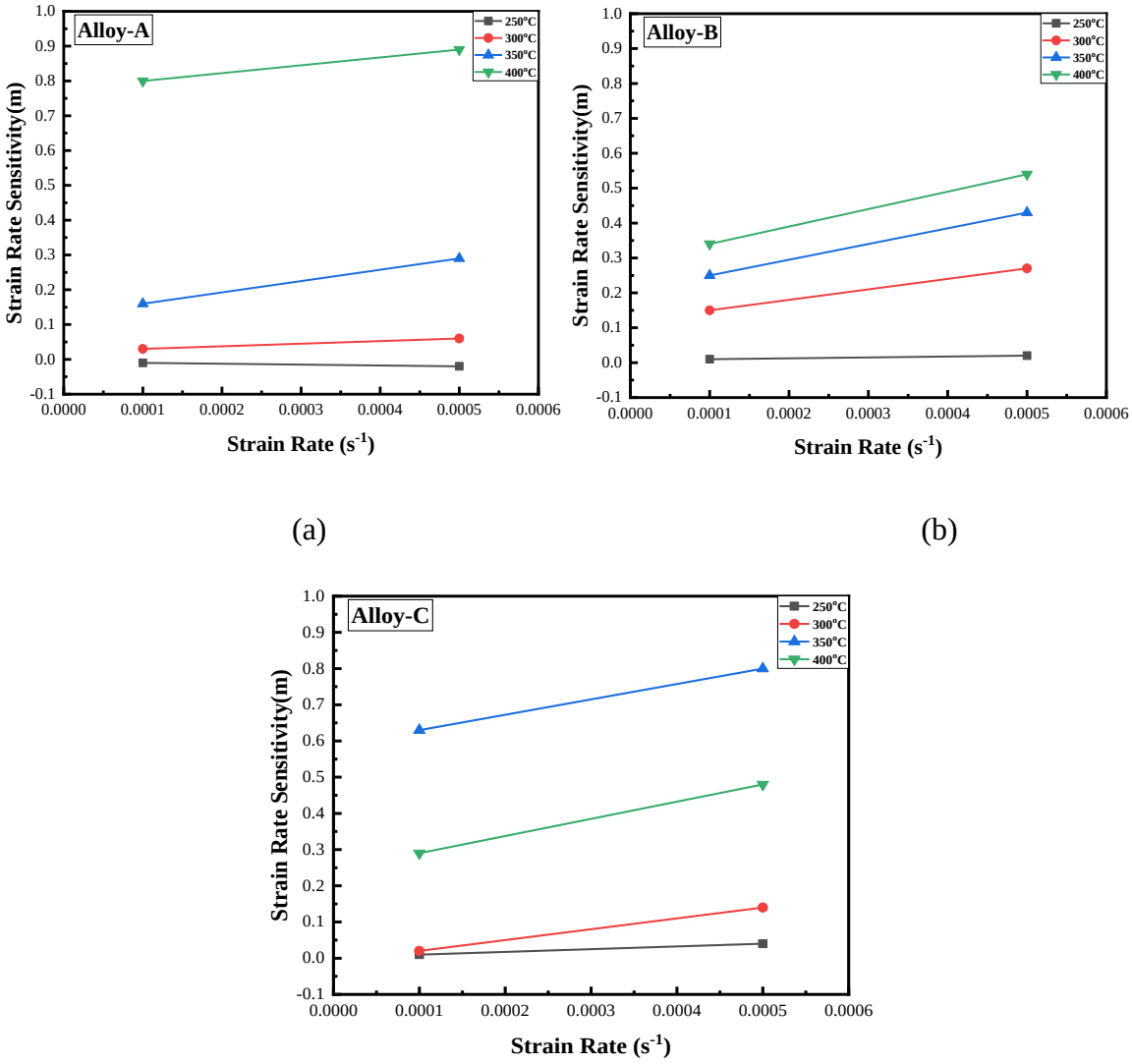

Figure 4.36: Plot of Strain Rate Sensitivity vs. Strain Rate for alloy-A, alloy-B, and alloy-C for Different Test Temperature.

By analyzing Figure 4.35 and Figure 4.36, it can be summarized that the strain rate sensitivity (m-values) tends to increase with temperature and strain rate, with few exceptions. This observation is consistent with several previous reports [114], [115]. It is reported [27] that the strain rate sensitivity index for superplastic materials should be larger

than or equal to 0.3, and it typically falls between 0.4 and 0.8 for most superplastic materials. The 'm-values' from Table 4.11 and Table *4.12* show that at a strain rate of $5x10^{-4}$ s^{-1}, alloy-A and alloy-B exhibit superplastic behavior at a temperature of 400° C, while alloy-C exhibits superplastic behavior at a temperature of 350° C, with grain boundary sliding as the dominant deformation mechanism. On the other hand, at a strain rate of $1x10^{-4}$ s^{-1}, alloy-A at 400° C and alloy-C at 350° C exhibit superplastic behavior with high 'm-values' of 0.8 and 0.63, respectively.

After conducting tests over a wide range of temperatures in previous studies [77], it was found that 400° C is the optimum temperature for superplastic behavior in several Mg alloys. These observations from previous reports is consistent with the findings of this study, here alloy-A and B have exhibited superplastic behavior at 400° C and for alloy-C the temperature is 350° C.

In Figure 4.37, displays a plot of m value against elongation to failure (%). The "blue" colored spots in this diagram denote a strain rate of $1x10^{-4}$ s^{-1}, whereas the "red" colored points denote a strain rate of $5x10^{-4}$ s^{-1}.

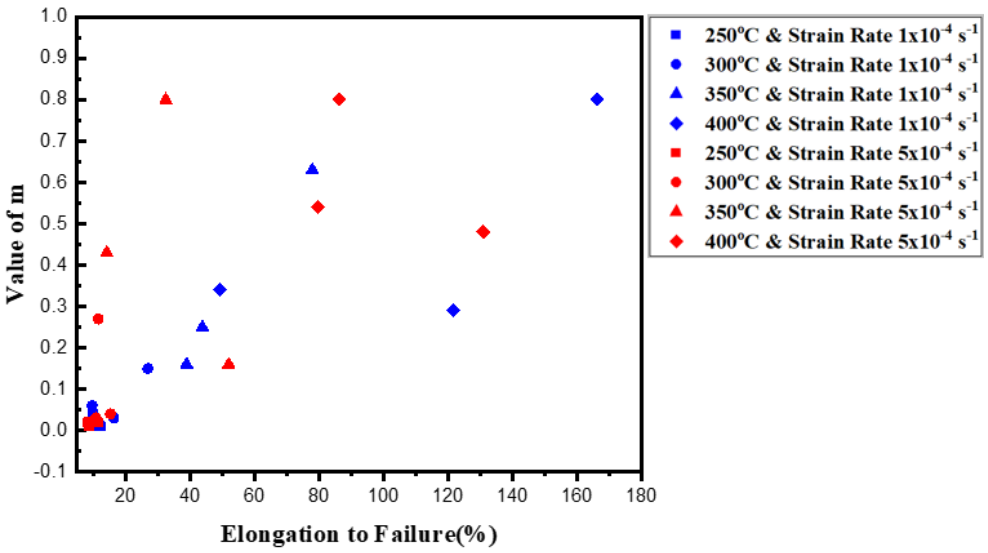

Figure 4.37: Plot of Values of the Strain Rate Sensitivity(m) against Elongation to Failure (%)

It can be observed from the figure that high m values (above 0.4) have been achieved at elevated temperatures, associated with large tensile elongation values, with only a few exceptions. The value of m is strongly correlated with the tensile ductility of metal alloys. When the value of m is low, the increased strain rate at the neck-region will be significantly

accelerated by the increased stress there. As a result, the neck will develop quickly, resulting in an abrupt failure and a low elongation to failure. On the other hand, for large m, the strain rate slowly rises as a result of the elevated tension in the neck-region. As a result, the neck gradually grows, delaying the onset of tensile failure and resulting in significant tensile elongations. Therefore, as the strain rate sensitivity increases, the tensile ductility enhances [76]. In other words, it can be said that ductility increases with increasing m value [116]. This trend from Figure 4.37 indicates the presence of superplastic behavior in the alloys at higher temperatures, which is consistent with previous findings [77] [117].

Again, it is found that grain boundary sliding is the main mode of deformation in alloys with $m > 0.33$ during superplastic flow [72]. Three alloys of this study also have exhibited superplastic behavior at high temperature (400^{O} C for alloy-A and B, 350^{o} C for alloy-C) due to their high values of m and elongation to failure, with grain boundary sliding as dominant deformation mechanism.

However, the most common way is used to measure the SRS index (m value) by conducting tensile test at two constant strain rates. As found earlier studies [115] [114], composition of alloys, microstructural features like texture, grain size, and twinning, as well as experimental parameters like strain rate and temperature, all have an impact on SRS. Therefore, there is a possibility of microstructure changes in each test conducted at different strain rates due to variations in recovery and deformation history which may affect the calculation of m value.

4.8 Synergetic Impacts

Increasing the Gd content in the Mg-1Zn-1.5Y alloy system resulted in a decrease in grain sizes under all conditions, including as-cast, homogenized, and hot-rolled states. Notably, hot rolling at 420°C significantly promoted grain size reduction, attributed to dynamic recrystallization during the hot rolling process. Furthermore, it was observed the evolution of various secondary phases due to changes in Gd composition. The volume fraction of the 14H-LPSO phase increased with increasing Gd content, while other phases like Mg_5GdY and W-phase were found within the α-Mg matrix, each with varying volume fractions. These fractions changed with temperature, as indicated by CALPAD analysis, reflecting the different melting temperatures of these phases. The volume fraction of the 14H-LPSO phase decreased with temperature (250°C, 300°C, 350°C, and 400°C), which corresponded to a weakening of the tensile strength of the alloys at elevated temperatures due to the

dissolution of 14H-LPSO in the matrix. Alloy-B, featuring the pinning effect of the W-phase, exhibited a superior combination of tensile strength and ductility compared to other alloys at 350°C and 400°C. At a higher strain rate ($5x10^{-4}$ s^{-1}), tensile strength values were higher compared to lower strain rates. The increased tensile strength observed at higher strain rates can be attributed to the formation of smaller-sized grains during the tensile test through dynamic recrystallization, while slower strain rates ($1x10^{-4}$ s^{-1}) resulted in larger-sized grains and consequently lower strength values. However, strain rate $5x10^{-4}$ s^{-1} showed a trend of lower elongation to failure compared to strain rate $1x10^{-4}$ s^{-1}, except at 400°C. For both strain rates, the values of strain rate sensitivity (m) increased with temperature up to 400°C for alloys A and B. In contrast, alloy C exhibited a different trend, reaching its maximum value at 350°C. Based on the strain exponent (n) and the strain rate sensitivity index (m), it was observed a dispersed strengthening mechanism at lower temperatures (250°C and 300°C), transitioning to climb-controlled creep, glide-controlled creep, and grain-boundary sliding at higher temperatures (350°C and 400°C), irrespective of the strain rate.

Chapter 5

Conclusions

This study aimed to examine the impact of Gd on the microstructure and deformation mechanism in the Mg-1Zn-1.5Y alloy system under varying temperatures and strain rates. The following are the summaries of the results:

i. As-cast sample microstructure investigation showed that the addition of Gd to the alloy increased dendrite formation, caused a reduction in grain size, and resulted in an increased amount of secondary particles in the matrix.

ii. The investigation of microstructure in homogenized samples revealed the disappearance of dendritic arms and solute segregation observed in the as-cast sample, as well as an increased grain size attributed to grain growth.

iii. The microstructure of the rolled samples revealed that the grain size of the sample decreased as the Gd concentration of the alloy increased; this can be attributed to recrystallization that occurs during hot rolling.

iv. The XRD results indicated that in the Mg-1Zn-1.5Y-1Gd alloy, the $Mg_{12}Zn(Gd,Y)$ (14H-LPSO phase) and Mg_5GdY secondary phase were embedded in the α-Mg matrix. Increasing the Gd content up to 2 wt% led to the formation of a new phase, $Mg_3Zn_3(Gd,Y)$ (W-phase), and further increase in Gd content resulted in the disappearance of the W-phase and increase in the 14H-LPSO phase compared to the 1% Gd alloy.

v. The presence of the 14H-LPSO phase, W-phase, and Mg_5GdY secondary phase in the α-Mg matrix, depending on the Gd content, was also confirmed by SEM images and EDS analysis. Additionally, particle size and volume fraction of secondary phase particle were found to increase with increasing Gd content upto 6% Gd as observed from the SEM images.

vi. CALPHAD analysis suggests that the 14H-LPSO phase is present in all the investigated alloys, with its volume fraction increasing notably with Gd content, peaking at 6% Gd. However, beyond 450°C, the 14H-LPSO phase dissolves within the matrix. In the case of alloy-B, the $Mg_3Zn_3(Gd,Y)_2$ (W-phase) demonstrates remarkable thermal stability, persisting from room temperature up to 600° C. The $Mg_5(Gd,Y)$ phase is also observed in alloy-A and C, although in very small amounts at temperatures below 200° C. In

addition, it is also evident that alterations in composition have minimal impact on the solidus and liquidus temperatures.

vii. Tensile test results show that addition of Gd up to 2% results in better tensile strength and reduced elongation capacity at elevated temperature (400^{o} C), which can be attributed to the pinning effect of W-phase. However, an optimal combination of strength and ductility is observed in alloy-B (2% Gd) at 350^{o} and 400° C and both strain rates, with few exceptions, attributed to the presence of a bimodal 14H-LPSO phase (mix of lamellar and blocky LPSO) and the W-phase at elevated temperatures. Conversely, alloy-C demonstrates promising performance below 350° C, possibly due to the maximum volume fraction of the blocky LPSO phase.

viii. High temperatures caused flow softening, which led to reduced tensile strength and higher elongation to failure as the temperature increased (350° C and 400° C).

ix. For higher strain rate, tensile strength values were found greater than slower strain rate. The higher tensile strength observed at higher strain rates in this study can be attributed to the formation of smaller-sized grains during the tensile test through dynamic recrystallization, while the slower strain rates led to formation of relatively larger-sized grain and hence lower strength values.

x. For strain rate $5x10^{-4}$ s^{-1} shows a trend of lower elongation to failure than strain rate $1x10^{-4}$ s^{-1} except at 400^{o} C temperature. Since grain growth occurs at a slower strain rate ($1x10^{-4}$ s^{-1}), this can delay the formation of a neck. As a result, the material has more time to elongate before reaching failure.

xi. For both strain rates, the values of strain rate sensitivity (m) are found to increase with temperature up to 400^{o} C for alloys-A and B. However, alloy-C has exhibited a different trend. In the case of alloy-C, the strain-rate-sensitivity has reached its highest value at 350° C and then decreased at 400° C.

xii. Deformation mechanisms changed with temperature and strain rate. The activation energy value indicates that grain boundary diffusion was the deformation mechanism at lower strain rates. The deformation process switched from lattice self-diffusion to grain boundary diffusion at higher strain rates. But this approach of analysis is not appropriate for studying deformation mechanisms.

xiii. According to the strain exponent(n) and the stain rate sensitivity index(m), in most cases, a dispersed strengthening mechanism has been observed at lower temperatures (250° C and 300° C), which transitions into climb-controlled creep, glide-controlled

creep, and grain-boundary sliding at higher temperatures (350° C and 400° C) regardless of strain rate.

Appendix

EDX of Mg-1Zn-1.5Y-1Gd

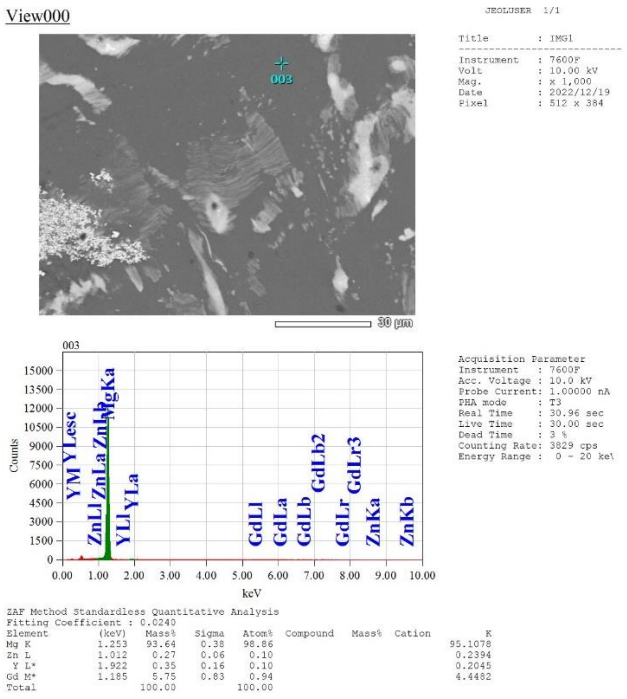

Figure: EDX of α-Mg phase in Mg-1Zn-1.5Y-1Gd Alloy

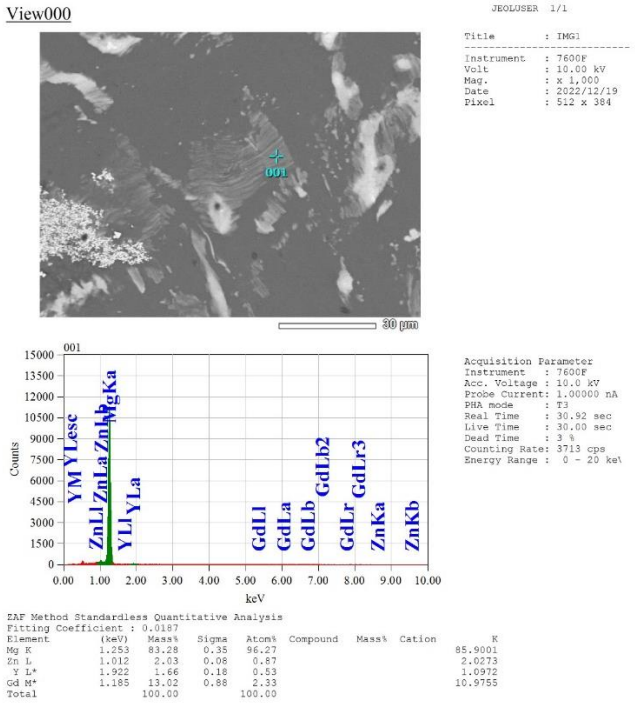

Figure: EDX of $Mg_{12}Zn(Gd,Y)$ (Z-phase/14H-LPSO) in Mg-1Zn-1.5Y-1Gd Alloy

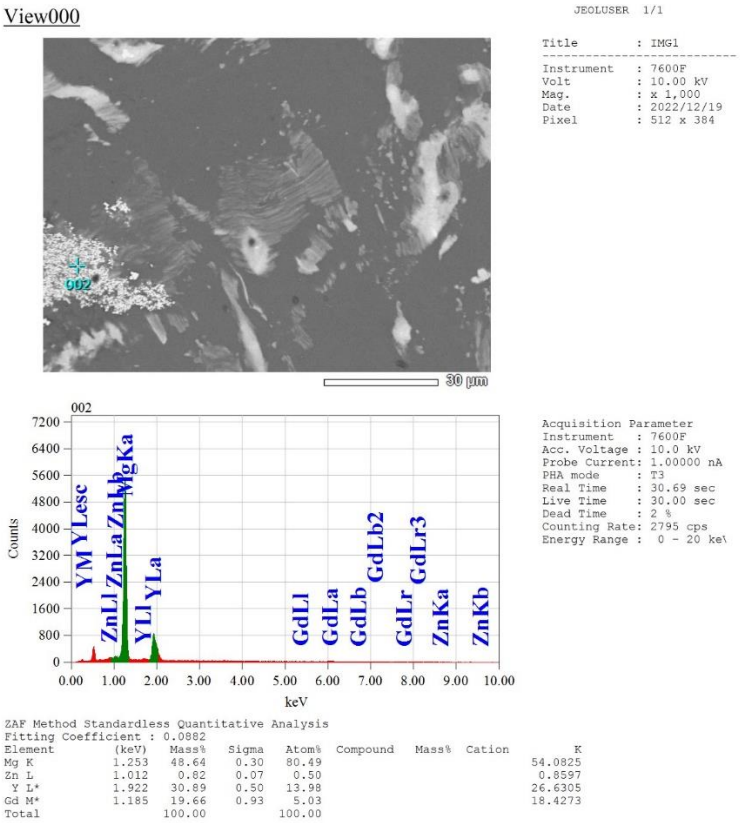

Figure: EDX of $Mg_5(Gd,Y)$ phase in Mg-1Zn-1.5Y-1Gd Alloy

EDX of Mg-1Zn-1.5Y-2Gd

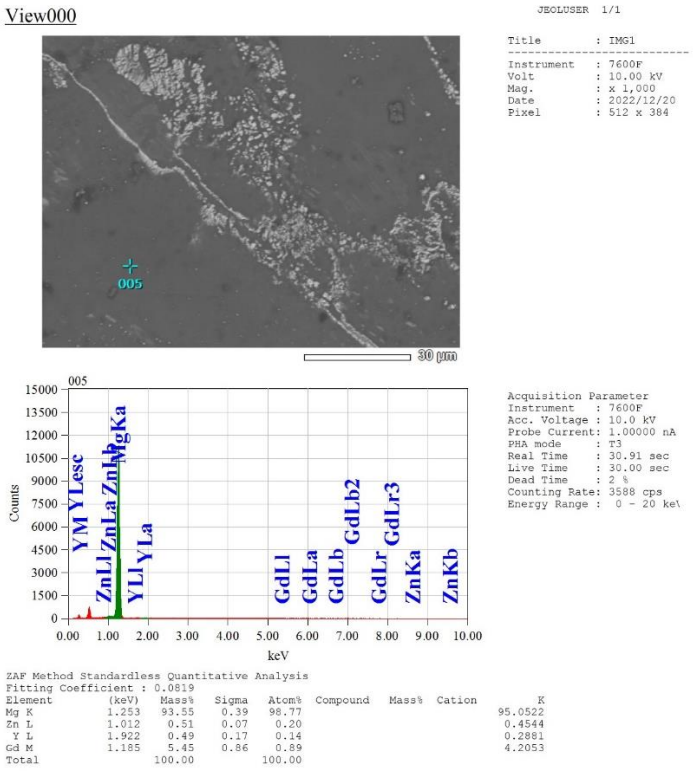

Figure: EDX of α-Mg phase in Mg-1Zn-1.5Y-2Gd Alloy

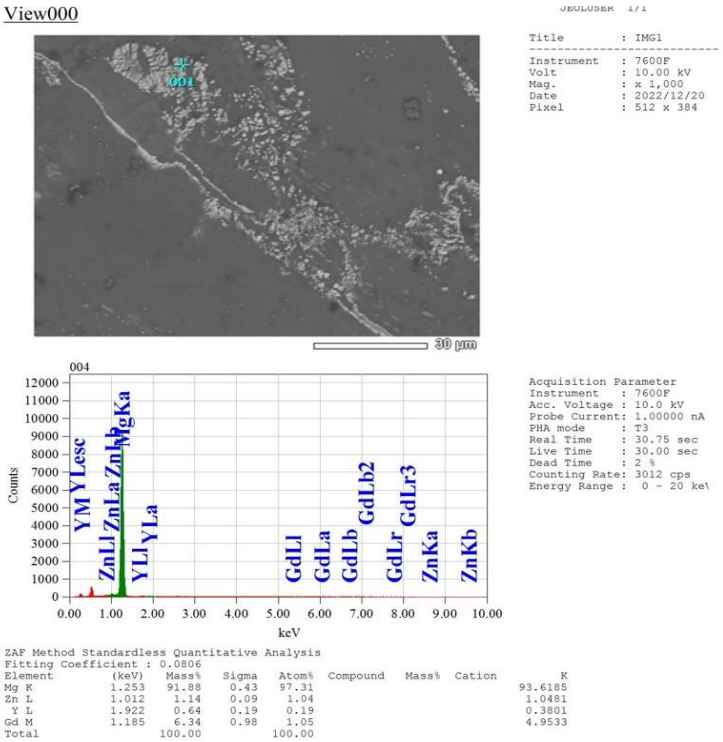

Figure: EDX of $Mg_3Zn_3(Gd,Y)_2$ (W-phase) phase in Mg-1Zn-1.5Y-2Gd Alloy

EDX of Mg-1Zn-1.5Y-2Gd

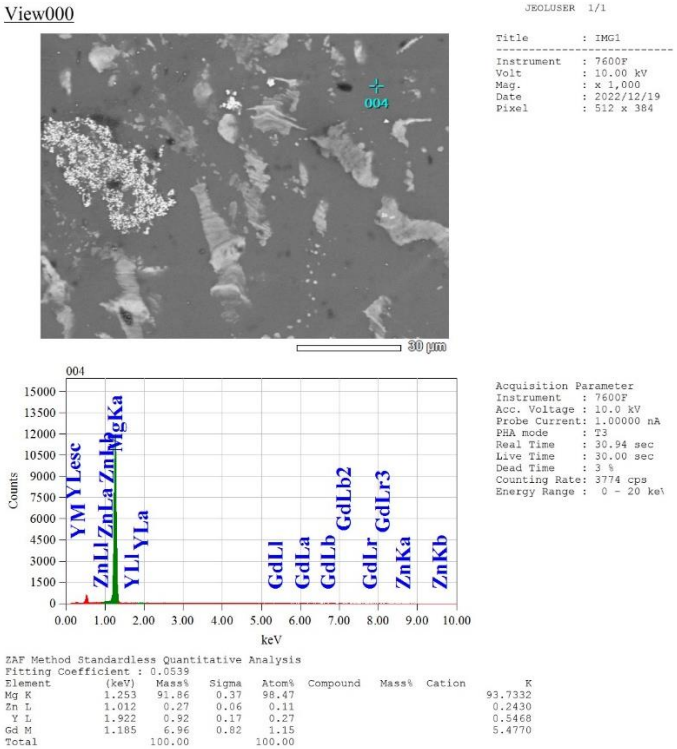

Figure: EDX of α-Mg phase in Mg-1Zn-1.5Y-6Gd Alloy

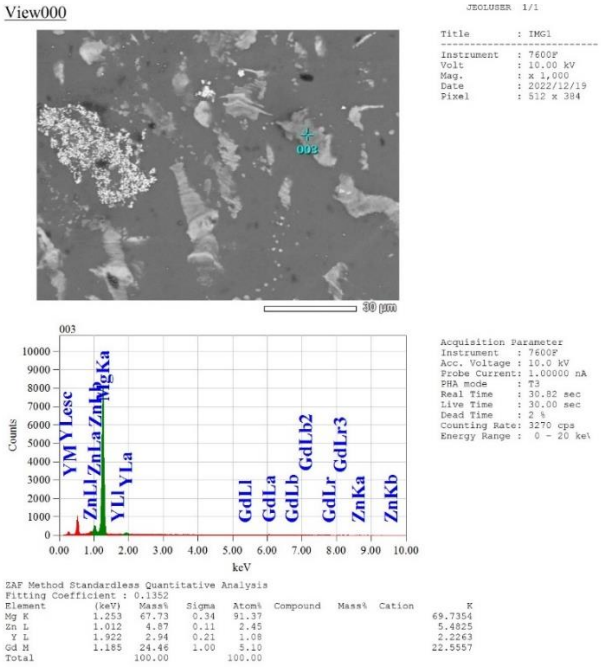

Figure: EDX of $Mg_{12}Zn(Gd,Y)$ (Z-phase/14H-LPSO) in Mg-1Zn-1.5Y-6Gd Alloy

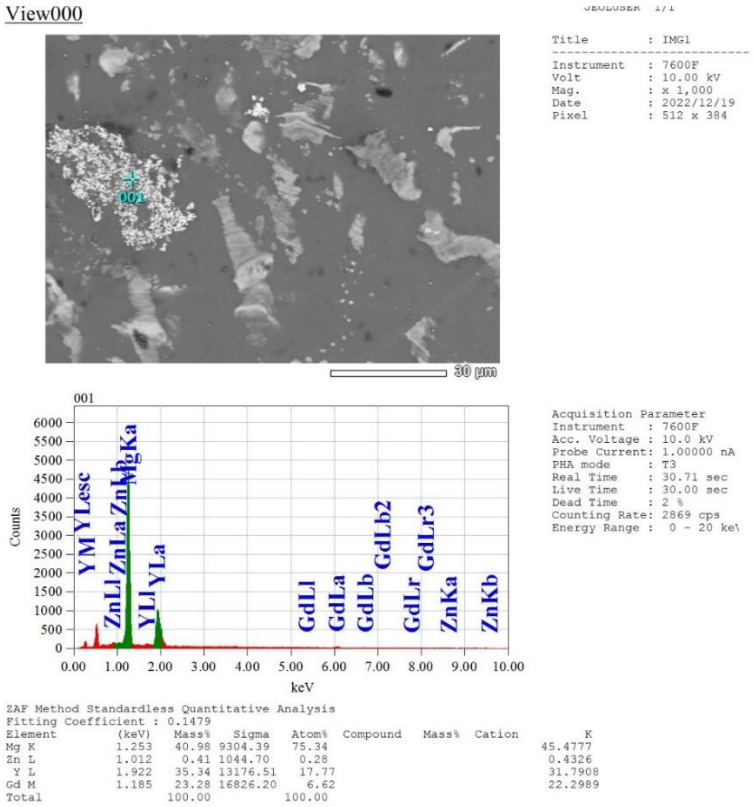

Figure: EDX of $Mg_5(Gd,Y)$ phase in Mg-1Zn-1.5Y-6Gd Alloy

References

[1] Y. Li, P. Hou, Z. Wu, Z. Feng, Y. Ren, and H. Choo, "Dynamic recrystallization of a wrought magnesium alloy: Grain size and texture maps and their application for mechanical behavior predictions," *Mater. Des.*, vol. 202, p. 109562, 2021, doi: 10.1016/j.matdes.2021.109562.

[2] G. Davies, *Materials for Automobile Bodies*. 2012. doi: 10.1016/C2010-0-66319-X.

[3] C. C. Jain and C. H. Koo, "Creep and corrosion properties of the extruded magnesium alloy containing rare earth," *Mater. Trans.*, vol. 48, no. 2, pp. 265–272, 2007, doi: 10.2320/matertrans.48.265.

[4] S. Yi, J. Bohlen, F. Heinemann, and D. Letzig, "Mechanical anisotropy and deep drawing behaviour of AZ31 and ZE10 magnesium alloy sheets," *Acta Mater.*, vol. 58, no. 2, pp. 592–605, 2010, doi: 10.1016/j.actamat.2009.09.038.

[5] M. Ahmadi, S. A. A. B. Tabary, D. Rahmatabadi, M. S. Ebrahimi, K. Abrinia, and R. Hashemi, "Review of selective laser melting of magnesium alloys: advantages, microstructure and mechanical characterizations, defects, challenges, and applications," *J. Mater. Res. Technol.*, vol. 19, pp. 1537–1562, 2022, doi: 10.1016/j.jmrt.2022.05.102.

[6] D. Rahmatabadi, R. Hashemi, M. Tayyebi, and A. Bayati, "Investigation of mechanical properties, formability, and anisotropy of dual phase Mg-7Li-1Zn," *Mater. Res. Express*, vol. 6, no. 9, pp. 0–12, 2019, doi: 10.1088/2053-1591/ab2de6.

[7] D. Carou, E. M. Rubio, and J. P. Davim, "Machinability of Magnesium and Its Alloys: A Review," vol. 1, no. 3, pp. 133–152, 2015, doi: 10.1007/978-3-662-45088-8_5.

[8] V. Manakari, G. Parande, and M. Gupta, *Selective laser melting of magnesium and magnesium alloy powders: A review*, vol. 7, no. 1. 2017. doi: 10.3390/met7010002.

[9] S. Johnston, Z. Shi, and A. Atrens, "The influence of pH on the corrosion rate of high-purity Mg, AZ91 and ZE41 in bicarbonate buffered Hanks' solution," *Corros. Sci.*, vol. 101, pp. 182–192, 2015, doi: 10.1016/j.corsci.2015.09.018.

[10] I. Toda-Caraballo, E. I. Galindo-Nava, and P. E. J. Rivera-Díaz-Del-Castillo, "Understanding the factors influencing yield strength on Mg alloys," *Acta Mater.*, vol. 75, pp. 287–296, 2014, doi: 10.1016/j.actamat.2014.04.064.

[11] Z. R. Zeng, M. Z. Bian, S. W. Xu, C. H. J. Davies, N. Birbilis, and J. F. Nie, "Effects of dilute additions of Zn and Ca on ductility of magnesium alloy sheet," *Mater. Sci. Eng. A*, vol. 674, pp. 459–471, 2016, doi: 10.1016/j.msea.2016.07.049.

[12] B. L. Mordike and T. Ebert, "Magnesium Properties - applications - potential," *Mater. Sci. Eng. A*, vol. 302, no. 1, pp. 37–45, 2001, doi: 10.1016/S0921-5093(00)01351-4.

[13] J. Xing, X. Yang, H. Miura, and T. Sakai, "Superplasticity of fine-grained magnesium alloy AZ31 processed by multi-directional forging," *Mater. Trans.*, vol. 48, no. 6, pp. 1406–1411, 2007, doi: 10.2320/matertrans.L-MRA2007839.

[14] L. Capolungo, I. J. Beyerlein, and C. N. Tomé, "Slip-assisted twin growth in hexagonal close-packed metals," *Scr. Mater.*, vol. 60, no. 1, pp. 32–35, 2009, doi: 10.1016/j.scriptamat.2008.08.044.

[15] P. Scroll and D. For, "Deformation twinning in h.c.p. metals and alloys," *Philos. Mag. A*, vol. 63, no. January 2012, pp. 987–1000, 2006.

[16] A. Jain and S. R. Agnew, "Modeling the temperature dependent effect of twinning on the behavior of magnesium alloy AZ31B sheet," *Mater. Sci. Eng. A*, vol. 462, no. 1–2, pp. 29–36, 2007, doi: 10.1016/j.msea.2006.03.160.

[17] A. Chapuis and J. H. Driver, "Temperature dependency of slip and twinning in plane strain compressed magnesium single crystals," *Acta Mater.*, vol. 59, no. 5, pp. 1986–1994, 2011, doi: 10.1016/j.actamat.2010.11.064.

[18] G. L. Makar and J. Kruger, "Corrosion of magnesium," *Int. Mater. Rev.*, vol. 38, no. 3, pp. 138–153, 1993, [Online]. Available: http://www.tandfonline.com/doi/abs/10.1179/imr.1993.38.3.138

[19] S. S. Vagarali and T. G. Langdon, "Deformation mechanisms in h.c.p. metals at elevated temperatures-II. Creep behavior of a Mg-0.8% Al solid solution alloy,"

Acta Metall., vol. 30, no. 6, pp. 1157–1170, 1982, doi: 10.1016/0001-6160(82)90009-8.

[20] A. Luo and M. O. Pekguleryuz, "Cast magnesium alloys for elevated temperature applications," *J. Mater. Sci.*, vol. 29, no. 20, pp. 5259–5271, 1994, doi: 10.1007/BF01171534.

[21] Q. Luo *et al.*, "Thermodynamics and kinetics of phase transformation in rare earth–magnesium alloys: A critical review," *J. Mater. Sci. Technol.*, vol. 44, pp. 171–190, 2020, doi: 10.1016/j.jmst.2020.01.022.

[22] A. E. Coy, F. Viejo, P. Skeldon, and G. E. Thompson, "Susceptibility of rare-earth-magnesium alloys to micro-galvanic corrosion," *Corros. Sci.*, vol. 52, no. 12, pp. 3896–3906, 2010, doi: 10.1016/j.corsci.2010.08.006.

[23] I. J. Polmear, "Magnesium alloys and applications," *Mater. Sci. Technol. (United Kingdom)*, vol. 10, no. 1, pp. 1–16, 1994, doi: 10.1179/mst.1994.10.1.1.

[24] K. Hagihara *et al.*, "Effect of long-period stacking ordered phase on mechanical properties of Mg97Zn1Y2 extruded alloy," *Acta Mater.*, vol. 58, no. 19, pp. 6282–6293, 2010, doi: 10.1016/j.actamat.2010.07.050.

[25] S. Cai, T. Lei, N. Li, and F. Feng, "Effects of Zn on microstructure, mechanical properties and corrosion behavior of Mg-Zn alloys," *Mater. Sci. Eng. C*, vol. 32, no. 8, pp. 2570–2577, 2012, doi: 10.1016/j.msec.2012.07.042.

[26] J. Yuan *et al.*, "Effect of Zn content on the microstructures, mechanical properties, and damping capacities of Mg–7Gd–3Y–1Nd–0.5Zr based alloys," *J. Alloys Compd.*, vol. 773, pp. 919–926, 2019, doi: 10.1016/j.jallcom.2018.09.303.

[27] N. Jiang, L. Chen, L. Meng, C. Fang, H. Hao, and X. Zhang, "Effect of neodymium, gadolinium addition on microstructure and mechanical properties of AZ80 magnesium alloy," *J. Rare Earths*, vol. 34, no. 6, pp. 632–637, 2016, doi: 10.1016/S1002-0721(16)60072-8.

[28] L. Ye *et al.*, "Modification of Mg2Si in Mg-Si alloys with gadolinium," *Mater. Charact.*, vol. 79, pp. 1–6, 2013, doi: 10.1016/j.matchar.2013.02.005.

[29] A. Kania, R. Nowosielski, A. Gawlas-Mucha, and R. Babilas, “Mechanical and corrosion properties of Mg-based alloys with Gd addition,” *Materials (Basel).*, vol. 12, no. 11, pp. 30–35, 2019, doi: 10.3390/ma12111775.

[30] I. A. Anyanwu, S. Kamado, and Y. Kojima, “Creep properties of Mg-Gd-Y-Zr alloys,” *Materials Transactions*, vol. 42, no. 7. pp. 1212–1218, 2001. doi: 10.2320/matertrans.42.1212.

[31] S. Wasiur-Rahman and M. Medraj, “Critical assessment and thermodynamic modeling of the binary Mg-Zn, Ca-Zn and ternary Mg-Ca-Zn systems,” *Intermetallics*, vol. 17, no. 10, pp. 847–864, 2009, doi: 10.1016/j.intermet.2009.03.014.

[32] O. B. Fabrichnaya, H. L. Lukas, G. Effenberg, and F. Aldinger, “Thermodynamic optimization in the Mg-Y system,” *Intermetallics*, vol. 11, no. 11-12 SPEC. ISS, pp. 1183–1188, 2003, doi: 10.1016/S0966-9795(03)00156-0.

[33] M. Mezbahul-Islam, A. O. Mostafa, and M. Medraj, “Essential Magnesium Alloys Binary Phase Diagrams and Their Thermochemical Data,” *J. Mater.*, vol. 2014, pp. 1–33, 2014, doi: 10.1155/2014/704283.

[34] M. Hampl *et al.*, “Thermodynamic assessment and experimental study of Mg-Gd alloys,” *J. Alloys Compd.*, vol. 581, pp. 166–177, 2013, doi: 10.1016/j.jallcom.2013.07.042.

[35] F. Ozturk, A. Sisman, S. Toros, S. Kilic, and R. C. Picu, “Influence of aging treatment on mechanical properties of 6061 aluminum alloy,” *Mater. Des.*, vol. 31, no. 2, pp. 972–975, 2010, doi: 10.1016/j.matdes.2009.08.017.

[36] Z. Yang, Z. H. Wang, H. B. Duan, Y. C. Guo, P. H. Gao, and J. P. Li, “Microstructure evolution of Mg-6Gd-2Y alloy during solid solution and aging process,” *Mater. Sci. Eng. A*, vol. 631, pp. 160–165, 2015, doi: 10.1016/j.msea.2015.02.041.

[37] S. Asqardoust, A. Zarei-Hanzaki, S. M. Fatemi, and M. Moradjoy-Hamedani, “High temperature deformation behavior and microstructural evolutions of a high Zr containing WE magnesium alloy,” *J. Alloys Compd.*, vol. 669, pp. 108–116, 2016, doi: 10.1016/j.jallcom.2016.01.232.

[38] H. Liao *et al.*, “Effect of heat treatment on LPSO morphology and mechanical properties of Mg–Zn–Y–Gd alloys,” *J. Magnes. Alloy.*, vol. 8, no. 4, pp. 1120–1127, 2020, doi: 10.1016/j.jma.2020.06.009.

[39] L. Gao, R. S. Chen, and E. H. Han, “Effects of rare-earth elements Gd and Y on the solid solution strengthening of Mg alloys,” *J. Alloys Compd.*, vol. 481, no. 1–2, pp. 379–384, 2009, doi: 10.1016/j.jallcom.2009.02.131.

[40] L. A. Gypen and A. Deruyttere, “Multi-component solid solution hardening - Part 2 Agreement with experimental results,” *J. Mater. Sci.*, vol. 12, no. 5, pp. 1034–1038, 1977, doi: 10.1007/BF00540988.

[41] R. Labusch, “A Statistical Theory of Solid Solution Hardening,” *Phys. Status Solidi*, vol. 41, no. 2, pp. 659–669, 1970, doi: 10.1002/pssb.19700410221.

[42] S. W. Xu, S. Kamado, and T. Honma, “Effect of homogenization on microstructures and mechanical properties of hot compressed Mg-9Al-1Zn alloy,” *Mater. Sci. Eng. A*, vol. 528, no. 6, pp. 2385–2393, 2011, doi: 10.1016/j.msea.2010.11.047.

[43] J. Koike, “Enhanced deformation mechanisms by anisotropic plasticity in polycrystalline Mg alloys at room temperature,” *Metall. Mater. Trans. A Phys. Metall. Mater. Sci.*, vol. 36, no. 7, pp. 1689–1696, 2005, doi: 10.1007/s11661-005-0032-4.

[44] B. C. Suh, J. H. Kim, J. H. Bae, J. H. Hwang, M. S. Shim, and N. J. Kim, “Effect of Sn addition on the microstructure and deformation behavior of Mg-3Al alloy,” *Acta Mater.*, vol. 124, pp. 268–279, 2017, doi: 10.1016/j.actamat.2016.11.020.

[45] R. E. Reed-Hill and W. D. Robertson, “Deformation of magnesium single crystals by nonbasal slip,” *Jom*, vol. 9, no. 4, pp. 496–502, 1957, doi: 10.1007/bf03397907.

[46] Y. Chang and D. M. Kochmann, “A variational constitutive model for slip-twinning interactions in hcp metals: Application to single- and polycrystalline magnesium,” *Int. J. Plast.*, vol. 73, pp. 39–61, 2015, doi: 10.1016/j.ijplas.2015.03.008.

[47] Q. Ma, B. Li, E. B. Marin, and S. J. Horstemeyer, “Twinning-induced dynamic recrystallization in a magnesium alloy extruded at 450 °c,” *Scr. Mater.*, vol. 65, no.

9, pp. 823–826, 2011, doi: 10.1016/j.scriptamat.2011.07.046.

[48] S. Sandlöbes, S. Zaefferer, I. Schestakow, S. Yi, and R. Gonzalez-Martinez, “On the role of non-basal deformation mechanisms for the ductility of Mg and Mg-Y alloys,” *Acta Mater.*, vol. 59, no. 2, pp. 429–439, 2011, doi: 10.1016/j.actamat.2010.08.031.

[49] B. Jóni, T. Al-Samman, S. G. Chowdhury, G. Csiszár, and T. Ungár, “Dislocation densities and prevailing slip-system types determined by X-ray line profile analysis in a textured AZ31 magnesium alloy deformed at different temperatures,” *J. Appl. Crystallogr.*, vol. 46, no. 1, pp. 55–62, 2013, doi: 10.1107/S0021889812046705.

[50] J. Koike, N. Fujiyama, D. Ando, and Y. Sutou, “Roles of deformation twinning and dislocation slip in the fatigue failure mechanism of AZ31 Mg alloys,” *Scr. Mater.*, vol. 63, no. 7, pp. 747–750, 2010, doi: 10.1016/j.scriptamat.2010.03.021.

[51] Y. Chino, K. Sassa, and M. Mabuchi, “Texture and stretch formability of a rolled Mg-Zn alloy containing dilute content of Y,” *Mater. Sci. Eng. A*, vol. 513–514, no. C, pp. 394–400, 2009, doi: 10.1016/j.msea.2009.01.074.

[52] S. Yi, J. Bohlen, F. Heinemann, and D. Letzig, “Mechanical anisotropy and deep drawing behaviour of AZ31 and ZE10 magnesium alloy sheets,” *Acta Mater.*, vol. 58, no. 2, pp. 592–605, 2010, doi: 10.1016/j.actamat.2009.09.038.

[53] S. Sandlöbes *et al.*, “The relation between ductility and stacking fault energies in Mg and Mg-Y alloys,” *Acta Mater.*, vol. 60, no. 6–7, pp. 3011–3021, 2012, doi: 10.1016/j.actamat.2012.02.006.

[54] J. A. Yasi, T. Nogaret, D. R. Trinkle, Y. Qi, L. G. Hector, and W. A. Curtin, “Basal and prism dislocation cores in magnesium: Comparison of first-principles and embedded-atom-potential methods predictions,” *Model. Simul. Mater. Sci. Eng.*, vol. 17, no. 5, 2009, doi: 10.1088/0965-0393/17/5/055012.

[55] L. Wen, P. Chen, Z. F. Tong, B. Y. Tang, L. M. Peng, and W. J. Ding, “A systematic investigation of stacking faults in magnesium via first-principles calculation,” *Eur. Phys. J. B*, vol. 72, no. 3, pp. 397–403, 2009, doi: 10.1140/epjb/e2009-00365-2.

[56] S. Groh, E. B. Marin, M. F. Horstemeyer, and D. J. Bammann, “Dislocation motion

in magnesium: A study by molecular statics and molecular dynamics," *Model. Simul. Mater. Sci. Eng.*, vol. 17, no. 7, 2009, doi: 10.1088/0965-0393/17/7/075009.

[57] C. X. Li, S. H. Dang, L. P. Wang, C. L. Zhang, and P. De Han, "First-principles study of the effects of selected interstitial atoms on the generalized stacking fault energies, strength, and ductility of Ni," *Chinese Phys. B*, vol. 23, no. 11, pp. 1–5, 2014, doi: 10.1088/1674-1056/23/11/117102.

[58] R. L. Fleischer, "Rapid solution hardening, dislocation mobility, and the flow stress of crystals," *J. Appl. Phys.*, vol. 33, no. 12, pp. 3504–3508, 1962, doi: 10.1063/1.1702437.

[59] M. H. Yoo, J. R. Morris, K. M. Ho, and S. R. Agnew, "Nonbasal deformation modes of HCP metals and alloys: Role of dislocation source and mobility," *Metall. Mater. Trans. A Phys. Metall. Mater. Sci.*, vol. 33, no. 3, pp. 813–822, 2002, doi: 10.1007/s11661-002-0150-1.

[60] R. K. Sabat, R. K. Mishra, A. K. Sachdev, and S. Suwas, "The deciding role of texture on ductility in a Ce containing Mg alloy," *Mater. Lett.*, vol. 153, pp. 158–161, 2015, doi: 10.1016/j.matlet.2015.03.036.

[61] M. Sanjari *et al.*, "Promotion of texture weakening in magnesium by alloying and thermomechanical processing: (I) alloying," *J. Mater. Sci.*, vol. 49, no. 3, pp. 1408–1425, 2014, doi: 10.1007/s10853-013-7826-3.

[62] W. Y. Wang *et al.*, "Effects of alloying elements on stacking fault energies and electronic structures of binary Mg alloys: A first-principles study," *Mater. Res. Lett.*, vol. 2, no. 1, pp. 29–36, 2014, doi: 10.1080/21663831.2013.858085.

[63] L. Wang, G. Fang, S. Leeflang, J. Duszczyk, and J. Zhou, "Investigation into the hot workability of the as-extruded WE43 magnesium alloy using processing map," *J. Mech. Behav. Biomed. Mater.*, vol. 32, pp. 270–278, 2014, doi: 10.1016/j.jmbbm.2014.01.011.

[64] F. J. Humphreys and M. Hatherly, *Recrystallization and Related Annealing Phenomena*. 2012. doi: 10.1016/C2009-0-07986-0.

[65] M. J. Stowell, “Metals and materials; science, processes, applications,” *Int. Mater. Rev.*, vol. 40, no. 5, pp. 218–218, 1995, doi: 10.1179/imr.1995.40.5.218.

[66] T. Al-Samman and G. Gottstein, “Dynamic recrystallization during high temperature deformation of magnesium,” *Mater. Sci. Eng. A*, vol. 490, no. 1–2, pp. 411–420, 2008, doi: 10.1016/j.msea.2008.02.004.

[67] G. Gottstein, L. Chang, and H. F. Yung, “Dynamic recrystallisation and microstructural evolution in Ni3Al,” *Mater. Sci. Technol. (United Kingdom)*, vol. 7, no. 2, pp. 158–166, 1991, doi: 10.1179/mst.1991.7.2.158.

[68] J. William D. Callister, *Materials Science and Engineering- An Introduction*. John Wiley and Sons., 2007. doi: 10.1007/BF01184995.

[69] B. N. Kim, K. Hiraga, Y. Sakka, and B. W. Ahn, “Grain-boundary diffusion model of dynamic grain growth during superplastic deformation,” *Acta Mater.*, vol. 47, no. 12, pp. 3433–3439, 1999, doi: 10.1016/S1359-6454(99)00201-3.

[70] R. A. P. Djaic and J. J. Jonas, “Recrystallization of high carbon steel between intervals of high temperature deformation,” *Metall. Trans.*, vol. 4, no. 2, pp. 621–624, 1973, doi: 10.1007/bf02648720.

[71] H. O. K. Kim, “Activation energies for the grain growth of an AZ31 Mg alloy after equal channel angular pressing,” *J. Mater. Sci.*, vol. 39, no. 23, pp. 7107–7109, 2004, doi: 10.1023/B:JMSC.0000047560.93940.45.

[72] O. D. (Stanford U. Nieh, T.G.(Lawrence Livermore Labaratory) ; Wadsworth, j.(Lawrence Livermore Labaratory); Sherby, “Superplasticity in Metals and Ceramics (Cambridge Solid State Science Series) by T. G. Nieh, J. Wadsworth, O. D. Sherby (z-lib.org.” Cambridge University Press, 1997.

[73] F. Lang, H. Tanaka, O. Munegata, T. Taguchi, and T. Narita, “The effect of strain rate and temperature on the tensile properties of Sn-3.5Ag solder,” *Mater. Charact.*, vol. 54, no. 3, pp. 223–229, 2005, doi: 10.1016/j.matchar.2004.11.013.

[74] Y. H. Wei *et al.*, “Superplasticity and grain boundary sliding in rolled AZ91 magnesium alloy at high strain rates,” *Mater. Sci. Eng. A*, vol. 360, no. 1–2, pp. 107–

115, 2003, doi: 10.1016/S0921-5093(03)00407-6.

[75] H. Somekawa, K. Hirai, H. Watanabe, Y. Takigawa, and K. Higashi, “Dislocation creep behavior in Mg-Al-Zn alloys,” *Mater. Sci. Eng. A*, vol. 407, no. 1–2, pp. 53–61, 2005, doi: 10.1016/j.msea.2005.06.059.

[76] J. Lin and F. P. E. Dunne, “Modelling grain growth evolution and necking in superplastic blow-forming,” *Int. J. Mech. Sci.*, vol. 43, no. 3, pp. 595–609, 2001, doi: 10.1016/S0020-7403(00)00055-2.

[77] M. A. Nazzal, M. K. Khraisheh, and F. K. Abu-Farha, “The effect of strain rate sensitivity evolution on deformation stability during superplastic forming,” *J. Mater. Process. Technol.*, vol. 191, no. 1–3, pp. 189–192, 2007, doi: 10.1016/j.jmatprotec.2007.03.097.

[78] M. A. Meyers, “Meyers M.A. - Dynamic Behavior of Materials-Wiley (1994).pdf.” 1994.

[79] J. Luo, M. Li, W. Yu, and H. Li, “The variation of strain rate sensitivity exponent and strain hardening exponent in isothermal compression of Ti-6Al-4V alloy,” *Mater. Des.*, vol. 31, no. 2, pp. 741–748, 2010, doi: 10.1016/j.matdes.2009.09.055.

[80] M. A. Khaleel, K. I. Johnson, C. H. Hamilton, and M. T. Smith, “Deformation modeling of superplastic AA-5083,” *Int. J. Plast.*, vol. 14, no. 10–11, pp. 1133–1154, 1998, doi: 10.1016/S0749-6419(98)00051-5.

[81] O. Guvener, A. Eyidogan, C. Oto, and P. Y. Huri, “Novel additive manufacturing applications for communicable disease prevention and control: focus on recent COVID-19 pandemic,” *Emergent Mater.*, vol. 4, no. 1, pp. 351–361, 2021, doi: 10.1007/s42247-021-00172-y.

[82] T. Mozammel, D. Dumbre, P. Selvakannan, K. K. Sadasivuni, and S. K. Bhargava, “Calcined hydrotalcites of varying Mg/Al ratios supported Rh catalysts: highly active mesoporous and stable catalysts toward catalytic partial oxidation of methane,” *Emergent Mater.*, vol. 4, no. 2, pp. 469–481, 2021, doi: 10.1007/s42247-020-00158-2.

[83] J. Tan and S. Ramakrishna, “Applications of magnesium and its alloys: A review,” *Appl. Sci.*, vol. 11, no. 15, 2021, doi: 10.3390/app11156861.

[84] D. S. Kumar, C. T. Sasanka, K. Ravindra, and K. N. S. Suman, “Magnesium and Its Alloys in Automotive Applications – A Review,” *Am. J. Mater. Sci. Technol.*, vol. 4, no. 1, pp. 12–30, 2015, doi: 10.7726/ajmst.2015.1002.

[85] D. S. Kumar and K. N. S. Suman, “Selection of Magnesium Alloy by MADM Methods for Automobile Wheels,” *Int. J. Eng. Manuf.*, vol. 4, no. 2, pp. 31–41, 2014, doi: 10.5815/ijem.2014.02.03.

[86] M. K. Kulekci, “Magnesium and its alloys applications in automotive industry,” *Int. J. Adv. Manuf. Technol.*, vol. 39, no. 9–10, pp. 851–865, 2008, doi: 10.1007/s00170-007-1279-2.

[87] A. A. Luo, *Applications: Aerospace, automotive and other structural applications of magnesium*. Woodhead Publishing Limited, 2013. doi: 10.1533/9780857097293.266.

[88] A. Wang and M. Li, “Effects of Sn on Microstructure and Mechanical Properties of Rolled Mg-Y-Ce-Zr Alloy,” *Tezhong Zhuzao Ji Youse Hejin/Special Cast. Nonferrous Alloy.*, vol. 40, no. 9, pp. 1034–1038, 2020, doi: 10.15980/j.tzzz.2020.09.026.

[89] M. M. Savalani, C. C. Ng, and H. C. Man, “Selective laser melting of magnesium for future applications in the medicine,” *Proc. - 2010 Int. Conf. Manuf. Autom. ICMA 2010*, pp. 50–54, 2010, doi: 10.1109/ICMA.2010.45.

[90] J. Suchy, M. Horynová, L. Klakurková, D. Palousek, D. Koutny, and L. Celko, “Effect of laser parameters on processing of biodegradable magnesium alloy WE43 via selective laser melting method,” *Materials (Basel).*, vol. 13, no. 11, 2020, doi: 10.3390/ma13112623.

[91] M. P. Staiger, A. M. Pietak, J. Huadmai, and G. Dias, “Magnesium and its alloys as orthopedic biomaterials: A review,” *Biomaterials*, vol. 27, no. 9, pp. 1728–1734, 2006, doi: 10.1016/j.biomaterials.2005.10.003.

[92] C. H. Cáceres and A. Blake, “The strength of concentrated Mg-Zn solid solutions,” *Phys. Status Solidi Appl. Res.*, vol. 194, no. 1, pp. 147–158, 2002, doi: 10.1002/1521-396X(200211)194:1<147::AID-PSSA147>3.0.CO;2-L.

[93] M. Yamasaki, K. Hashimoto, K. Hagihara, and Y. Kawamura, “Effect of multimodal microstructure evolution on mechanical properties of Mg-Zn-Y extruded alloy,” *Acta Mater.*, vol. 59, no. 9, pp. 3646–3658, 2011, doi: 10.1016/j.actamat.2011.02.038.

[94] F. Shi, C. Q. Wang, and Z. M. Zhang, “Microstructures, corrosion and mechanical properties of as-cast Mg-Zn-Y-(Gd) alloys,” *Trans. Nonferrous Met. Soc. China (English Ed.*, vol. 25, no. 7, pp. 2172–2180, 2015, doi: 10.1016/S1003-6326(15)63829-8.

[95] T. Chen, Z. Chen, J. Shao, R. Wang, L. Mao, and C. Liu, “Evolution of LPSO phases in a Mg-Zn-Y-Gd-Zr alloy during semi-continuous casting, homogenization and hot extrusion,” *Mater. Des.*, vol. 152, pp. 1–9, 2018, doi: 10.1016/j.matdes.2018.04.070.

[96] K. Liu, X. Wang, and K. Wen, “Effect of isothermal homogenization on microstructure and mechanical properties of the Mg-5Y-4Gd-0.5Zn-0.4Zr alloy,” *Mater. Des.*, vol. 52, pp. 1035–1042, 2013, doi: 10.1016/j.matdes.2013.06.048.

[97] C. Cai, R. Song, E. Wen, Y. Wang, and J. Li, “Effect of microstructure evolution on tensile fracture behavior of Mg-2Zn-1Nd-0.6Zr alloy for biomedical applications,” *Mater. Des.*, vol. 182, p. 108038, 2019, doi: 10.1016/j.matdes.2019.108038.

[98] D. J. Chen *et al.*, “Weak strengthening effect of the precipitated lamellar phase in the homogenized Mg-8Gd-4Y-1.6Zn-0.5Zr (wt%) alloy followed by furnace cooling,” *Mater. Sci. Eng. A*, vol. 744, pp. 1–9, 2019, doi: 10.1016/j.msea.2018.08.056.

[99] Z. H. Huang, S. M. Liang, R. S. Chen, and E. H. Han, “Solidification pathways and constituent phases of Mg-Zn-Y-Zr alloys,” *J. Alloys Compd.*, vol. 468, no. 1–2, pp. 170–178, 2009, doi: 10.1016/j.jallcom.2008.01.034.

[100] Z. Wei *et al.*, “Effects of Zn Content on Hot Tearing Susceptibility of Mg–Zn–Gd–Y–Zr Alloys,” *Int. J. Met.*, vol. 16, no. 4, pp. 1902–1914, 2022, doi: 10.1007/s40962-

021-00720-6.

[101] J. M. Meier *et al.*, “Phase equilibria and microstructure investigation of Mg-Gd-Y-Zn alloy system,” *J. Magnes. Alloy.*, vol. 10, no. 3, pp. 689–696, 2022, doi: 10.1016/j.jma.2021.09.019.

[102] P. S. Roodposhti, A. Sarkar, K. L. Murty, H. Brody, and R. Scattergood, “Grain boundary sliding mechanism during high temperature deformation of AZ31 Magnesium alloy,” *Mater. Sci. Eng. A*, vol. 669, pp. 171–177, 2016, doi: 10.1016/j.msea.2016.05.076.

[103] B. Zhang, P. S. Bate, and N. Ridley, “The Effect of Strain Rate History on the Dynamic Grain Growth Behaviour of AA 5083,” *Mater. Sci. Forum*, vol. 551–552, pp. 627–632, 2007, doi: 10.4028/www.scientific.net/msf.551-552.627.

[104] H. Yu, Y. Xin, M. Wang, and Q. Liu, “Hall-Petch relationship in Mg alloys: A review,” *J. Mater. Sci. Technol.*, vol. 34, no. 2, pp. 248–256, 2018, doi: 10.1016/j.jmst.2017.07.022.

[105] kenji H. Mabuchi Mamoru, Kubota Kohei, “New Recycling Process by Extrusion for Machined Chips of AZ91 Magnesium and Mechanical Properties of Extruded Bars.” pp. 1249–1254, 1995. doi: https://doi.org/10.2320/matertrans1989.36.1249.

[106] S. M. Baek *et al.*, “Effect of secondary phase particles on the tensile behavior of Mg-Zn-Ca alloy,” *Mater. Sci. Eng. A*, vol. 735, no. August, pp. 288–294, 2018, doi: 10.1016/j.msea.2018.08.050.

[107] S. K. Woo, R. Pei, T. Al-Samman, D. Letzig, and S. Yi, “Plastic instability and texture modification in extruded Mg-Mn-Nd alloy,” *J. Magnes. Alloy.*, vol. 10, no. 1, pp. 146–159, 2022, doi: 10.1016/j.jma.2021.07.003.

[108] J. Cai *et al.*, “Hot deformation behavior and microstructure evolutions of as-forged Mg-Gd-Y-Zn-Zr alloy,” *J. Mater. Res. Technol.*, vol. 21, pp. 1724–1736, 2022, doi: 10.1016/j.jmrt.2022.10.013.

[109] S. A. Habib, A. S. Khan, T. Gnäupel-Herold, J. T. Lloyd, and S. E. Schoenfeld, “Anisotropy, tension-compression asymmetry and texture evolution of a rare-earth-

containing magnesium alloy sheet, ZEK100, at different strain rates and temperatures: Experiments and modeling," *Int. J. Plast.*, vol. 95, pp. 163–190, 2017, doi: 10.1016/j.ijplas.2017.04.006.

[110] A. Venkataraman, M. Linne, S. Daly, and M. D. Sangid, "Criteria for the prevalence of grain boundary sliding as a deformation mechanism," *Materialia*, vol. 8, p. 100499, 2019, doi: 10.1016/j.mtla.2019.100499.

[111] H. Kokawa, T. Watanabe, and S. Karashima, "Sliding behaviour and dislocation structures in aluminium grain boundaries," *Philos. Mag. A Phys. Condens. Matter, Struct. Defects Mech. Prop.*, vol. 44, no. 6, pp. 1239–1254, 1981, doi: 10.1080/01418618108235806.

[112] E. Karimi, A. Zarei-Hanzaki, M. H. Pishbin, H. R. Abedi, and P. Changizian, "Instantaneous strain rate sensitivity of wrought AZ31 magnesium alloy," *Mater. Des.*, vol. 49, pp. 173–180, 2013, doi: 10.1016/j.matdes.2013.01.068.

[113] R. Korla and A. H. Chokshi, "Strain-rate sensitivity and microstructural evolution in a Mg – Al – Zn alloy," *Scr. Mater.*, vol. 63, no. 9, pp. 913–916, 2010, doi: 10.1016/j.scriptamat.2010.06.047.

[114] C. H. J. Davies, "The Effect of Twinning on Strain Rate Sensitivity during the Compression of Extruded Magnesium Alloy AZ31," *Mater. Sci. Forum*, vol. 539–543, pp. 1723–1728, 2007, doi: 10.4028/www.scientific.net/msf.539-543.1723.

[115] Y. B. Chun and C. H. J. Davies, "Twinning-induced negative strain rate sensitivity in wrought Mg alloy AZ31," *Mater. Sci. Eng. A*, vol. 528, no. 18, pp. 5713–5722, 2011, doi: 10.1016/j.msea.2011.04.059.

[116] A. Yilmaz, "The Portevin-Le Chatelier effect: A review of experimental findings," *Sci. Technol. Adv. Mater.*, vol. 12, no. 6, 2011, doi: 10.1088/1468-6996/12/6/063001.

[117] A. K. Ghosh and C. H. Hamilton, "Mechanical Behavior and Hardening Characteristics of a Superplastic Ti-6AI-4V Alloy," vol. 10, no. June, 1979.